



THE HONG KONG
POLYTECHNIC UNIVERSITY

香港理工大學

Pao Yue-kong Library

包玉剛圖書館

Copyright Undertaking

This thesis is protected by copyright, with all rights reserved.

By reading and using the thesis, the reader understands and agrees to the following terms:

1. The reader will abide by the rules and legal ordinances governing copyright regarding the use of the thesis.
2. The reader will use the thesis for the purpose of research or private study only and not for distribution or further reproduction or any other purpose.
3. The reader agrees to indemnify and hold the University harmless from and against any loss, damage, cost, liability or expenses arising from copyright infringement or unauthorized usage.

IMPORTANT

If you have reasons to believe that any materials in this thesis are deemed not suitable to be distributed in this form, or a copyright owner having difficulty with the material being included in our database, please contact lbsys@polyu.edu.hk providing details. The Library will look into your claim and consider taking remedial action upon receipt of the written requests.

Pao Yue-kong Library, The Hong Kong Polytechnic University, Hung Hom, Kowloon, Hong Kong

<http://www.lib.polyu.edu.hk>

**NANOCOMPOSITE-FUNCTIONALIZED
FIBRE-REINFORCED POLYMER
COMPOSITES WITH INTEGRATED SELF-
SENSING AND MONITORING
CAPABILITIES**

YIYIN SU

PhD

The Hong Kong Polytechnic University

2022

The Hong Kong Polytechnic University
Department of Mechanical Engineering

**Nanocomposite-functionalized Fibre-reinforced
Polymer Composites with Integrated Self-
sensing and Monitoring Capabilities**

Yiyin SU

**A thesis submitted in partial fulfillment of the requirements
for the degree of Doctor of Philosophy**

October 2021

CERTIFICATE OF ORIGINALITY

I hereby declare that this thesis is my own work and that, to the best of my knowledge and belief, it reproduces no material previously published or written, nor material that has been accepted for the award of any other degree or diploma, except where due acknowledgment has been made in the text.

Yiyin SU

ABSTRACT

Real-time, continuous condition monitoring of fibre-reinforced polymer (FRP) composites, from the onset of manufacturing, through service to the end of life, is of vital significance, to warrant the structural integrity, reliability and durability spanning the entire life cycle of composites. To accommodate such a need, prevailing integrity monitoring approaches use multiple types of sensors with different sensing philosophies, to monitor individual life cycle stage of composites. When conventional sensors, such as rigid lead zirconate titanate (PZT) wafers or brittle fibre Bragg grating (FBG) sensors, are embedded in composites, the sensors may, more or less, compromise the original structural integrity, regardless of the fact that the intended role of the sensors is to implement integrity monitoring of composites.

Envisaging such a deficiency and facilitated by the recent prosperity in nanotechnology, this PhD study explores and develops integratable nanocomposite piezoresistive sensors, which can precisely perceive strains induced by quasi-static loads, medium-frequency structural vibrations and high-frequency structure-guided ultrasonic waves (GUWs), to accommodate demanding monitoring requirements. To achieve such an objective, the present study embraces three key aspects, to hierarchically develop FRPs with integrated self-sensing and monitoring capabilities, namely:

- 1) the initial effort to graft glass fibres (GFs) with carbon nanotubes (CNTs) via chemical vapor deposition (CVD), endowing conventional glass fibre-reinforced polymer (GFRP) composites with the monitoring capability;
- 2) the further exploration to develop a new type of implantable nanocomposite piezoresistive sensor, with a morphologically optimized nanostructure, via spray coating – a cost-effective additive manufacturing approach;
- 3) the validation of self-continuous monitoring capability of FRPs with the above implantable nanocomposite sensors.

To address aspect 1) and enable conventional GFRPs to perform self-sensing and monitoring, sensing fabrics containing CNT-grafted GF sensors, referred as CNT-g-GF sensors in this study, are created via direct growing CNTs on GF fabrics through CVD. The high graphitization degree of grafted CNTs, synthesized in a low growth temperature at 500 °C, is affirmed via scrutinizing their Raman spectra, with a D-band to G-band intensity ratio <0.89. The smooth synthesis of CNTs at such a low temperature is a joint result of selecting the cobalt (II) nitrate hexahydrate as the catalyst precursor, the ethanol as the hydrocarbon precursor and the 5 vol% H₂/N₂ gas mixture as the carrier and reducing gas. The loadings of grafted CNTs are regulated to distribute CNTs in a close proximity manner, upon which the quantum tunnelling effect can be triggered and promoted when GUWs traverse the CNT-g-GF sensors. Experimental results show the high accuracy, sensitivity and fast response of

such-fabricated sensors to dynamic strains, with a frequency regime from 175 to 375 kHz. Single fibre tensile test (ASTM C1557) and fibre-reinforced polymer matrix composite tensile test (ASTM D3039) are launched to interrogate the possible influence of the CNT grafting process on tensile attributes, confirming no measurable variation in mechanical properties of hybrid composites due to the sensor integration. Thus-produced CNT-g-GF sensors can be used to calibrate the cure progress of epoxy, by measuring the dynamic variations in the electrical resistance (ER). The CNT-g-GF sensors also precisely sense in-service loads applied to the composites, with a gauge factor as high as 30.2. This type of sensor sheds light on the use of nanocomposite-driven fibre decoration towards the development of new functional composites.

To address aspect 2), a new sort of compatible nanocomposite piezoresistive sensors, which can be implanted into carbon fibre-reinforced polymer (CFRP) composites and networked for *in situ* acquisition of dynamic strains, is further explored. The nanocomposite ink, formulated with graphene nanoplatelets (GNPs) and polyvinylpyrrolidone (PVP), is tailored to acquire the percolation threshold of conductive nanofillers. The above ink is then deposited on partially precured ($\alpha = 0.4$) B-stage epoxy films using spray coating. The sensors are electrified, circuited and networked using highly conductive CNT-film-made wires, to be implanted into CFRPs and form a sensor network. With a morphologically optimized nano-

architecture in nanocomposites, the quantum tunnelling effect can be triggered in percolated networks, which enables the sensors to faithfully response to quasi-static loads (with a high gauge factor of 34.5), medium-frequency structural vibrations and high-frequency GUWs up to 450 kHz. Only ~45 μm in thickness (including wires), the implanted sensors exhibit high compatibility and nonintrusive attributes with host composite structures, as confirmed in tensile and bending tests.

To address aspect 3), such-fabricated implantable nanocomposite sensors are integrated into composites from the onset of manufacturing, to continuously monitor the cure progress and structural integrity of composites. In conjunction with differential scanning calorimetry (DSC) and a Sesták–Berggren autocatalytic kinetic model, cure behaviors of matrix are first comprehensively evaluated and understood. The matrix cure degree in manufacturing is correlated with subtle changes in propagation characteristics of GUWs perceived by the sensors. The implantable sensors successfully prove their capabilities of tracing the matrix cure progress and detecting the cure anomaly. Subsequent to cure monitoring, in-service integrity monitoring is continuously implemented by the same implanted sensors, to locate a transient impact.

Being sensitive, compatible and lightweight, both types of sensors developed in this study can be densely deployed in a composite structure – flat or non-flat, while not at

the cost of mechanical attributes of the original FRPs. With the demonstrated sensing performance, these nanocomposite sensors usher in a concrete road to implement either ER-based or acousto-ultrasonics-based continuous monitoring of composites, from manufacturing through service, to the end of life.

PUBLICATIONS ARISING FROM THE THESIS

Refereed Journal Papers

1. **Su Y.**, Yang J., Liao Y., Zhou P., Xu L., Zhou L. & Su Z.*, ‘An implantable, compatible and networkable nanocomposite piezoresistive sensor for *in situ* acquisition of dynamic responses of CFRPs’, *Composites Science and Technology*, 2021;208:108747. (JCR Q1, IF: 8.528)
2. **Su Y.**, Xu L., Zhou P., Yang J., Wang K., Zhou L. & Su Z.*, ‘*In situ* cure monitoring and in-service impact localization of FRPs using pre-implanted nanocomposite sensors’, *Composites Part A-Applied Science and Manufacturing*, 2022;154:106799. (JCR Q1, IF: 7.664)
3. **Su Y.**, Xu L., Zhou P., Yang J., Wang K., Zhou L. & Su Z.*, ‘Carbon nanotube-decorated glass fibre bundles for cure self-monitoring and load self-sensing of FRPs’, *Composites Communications*, 2021;27:100899. (JCR Q1, IF: 6.617)
4. Xu L., **Su Y.**, Wang K., Yang X., Yuan S. & Su Z.*, ‘An elastodynamic reciprocity theorem-based closed-form solution to second harmonic generation of Lamb waves by a fatigue crack: Theory & experimental validation’, *Journal of Sound and Vibration*, 2021;509:116226. (JCR Q1, IF: 3.655) (co-first author)
5. **Su Y.**, Zhou H., Xu L., Zhou P., Yang J., Lu T., Huang H., Zhou L. & Su Z.*, ‘Ultrafast-responsive carbon nanotube-grafted fibre textiles’, submitted to *Composite Structures*. (JCR Q2, IF: 5.407)
6. Yang J., **Su Y.**, Liao Y., Zhou P., Xu L. & Su Z.*, ‘Ultrasound tomography for health monitoring of carbon fibre-reinforced polymers using implanted nanocomposite sensor networks and enhanced reconstruction algorithm for the

- probabilistic inspection of damage imaging’, *Structural Health Monitoring-An International Journal*, 2021;14759217211023930. (JCR Q1, IF: 5.929)
7. Duongthipthewa A., Su Y. & Zhou L.*, ‘Electrical conductivity and mechanical property improvement by low-temperature carbon nanotube growth on carbon fiber fabric with nanofiller incorporation’, *Composites Part B-Engineering*, 2020;182:107581. (JCR Q1, IF: 9.078)
 8. Zhou P., Yang X., Su Y., Yang J., Xu L., Wang K., Zhou L. & Su Z.*, ‘Direct-write nanocomposite sensor array for ultrasonic imaging of composites’, *Composites Communications*, 2021;28:100937. (JCR Q1, IF: 6.617)
 9. Xu L., Wang K., Su Y., He Y., Yang J., Yuan S. & Su Z.*, ‘Surface/sub-surface crack-scattered nonlinear Rayleigh waves: A full analytical solution based on elastodynamic reciprocity theorem’, *Ultrasonics*, 2022;118:106578. (JCR Q1, IF: 2.890)
 10. Zhou P., Liao Y., Yang X., Su Y., Yang J., Xu L., Wang K., Zeng Z., Zhou L., Zhang Z. & Su Z.*, ‘Thermally stable, adhesively strong graphene/polyimide films for inkjet printing ultrasound sensors’, *Carbon*, 2021;184:64-71. (JCR Q1, IF: 9.594)
 11. Xu L., Wang K., Yang X., Su Y., Yang J., Liao Y., Zhou P. & Su Z.*, ‘Model-driven fatigue crack characterization and growth prediction: A two-step, 3-D fatigue damage modeling framework for structural health monitoring’, *International Journal of Mechanical Sciences*, 2021;195:106226. (JCR Q1, IF: 5.329)
 12. Li Y., Wang K., Wang Q., Yang J., Zhou P., Su Y., Guo S. & Su Z.*, ‘Acousto-ultrasonics-based health monitoring for nano-engineered composites using a dispersive graphene-networked sensing system’, *Structural Health Monitoring-An International Journal*, 2021;20(1):240-54. (JCR Q1, IF: 5.929)
 13. Zhou P., Cao W., Liao Y., Wang K., Yang X., Yang J., Su Y., Xu L., Zhou L., Zhang Z. & Su Z.*, ‘Temperature effect on all-inkjet-printed nanocomposite

piezoresistive sensors for ultrasonics-based health monitoring’, *Composites Science and Technology*, 2020;197:108273. (JCR Q1, IF: 8.528)

Refereed Papers in International Conference Proceedings

1. **Su Y.**, Yang J., Xu L., Zhou P. & Su Z.*, ‘An implantable, compatible and networkable nanocomposite sensor for continuous monitoring of FRPs’, in Proceedings of the 13th International Workshop on Structural Health Monitoring (IWSHM-13).

ACKNOWLEDGEMENTS

First and foremost, I would like to give my most pure-hearted gratitude to my chief supervisor, Prof. Zhongqing Su, for his education and guidance during my pursuit of PhD degree. Without his enlightening instruction and meticulous supervision, it would be an impossible mission for me to continue my study and complete this thesis. In addition to his vast academic knowledge, his personalities such as kindness, hard work and optimism will also have a lifelong impact on me. It is my great fortune to complete my PhD study under his supervision. Special thanks should be addressed to my associated supervisor, Prof. Limin Zhou, for his help in my academic life.

Throughout this venture, the whole world is suffering from the Coronavirus Disease-2019, it is my blessing to have met and befriended many persons, which help me get through this tough period in Hong Kong. I am indebted to Dr. Yaozhong Liao, Dr. Kai Wang, Dr. Yehai Li, for their timely guidance and help during my study period. With help from Lei Xu, Jianwei Yang, Pengyu Zhou, Tianhui Lu, Xiongbin Yang, Yi He, I am able to make my research progress and my life full of joy at HKPU.

Finally, my utmost acknowledgement goes to my most beloved father, mother and sister, for their encouragement, support and unconditional love.

NOMENCLATURE

Acronyms and Initialisms

FRP	Fibre-reinforced polymer
CM	Cure monitoring
BVID	Barely visible impact damage
SIM	Structural integrity monitoring
AE	Acoustic emission
FBG	Fibre Bragg grating
IDT	Interdigital transducer
PVDF	Polyvinylidene fluoride
PZT	Lead zirconate titanate
AM	Additive manufacturing
ER	Electrical resistance
GUW	Guided ultrasonic wave
CNT	Carbon nanotube
GF	Glass fibre
CVD	Chemical vapor deposition
SEM	Scanning electron microscopy
TEM	Transmission electron microscopy
TGA	Thermo gravimetric analysis
CF	Carbon fibre
GNP	Graphene nanoplatelet
PVP	Polyvinylpyrrolidone

CPC	Conductive polymer nanocomposite
CFRP	Carbon fibre-reinforced polymer
DSC	Differential scanning calorimetry
SHM	Structural health monitoring
RTM	Resin transfer molding
FTIR	Fourier transform infrared spectroscopy
DMA	Dynamic mechanical analysis
TBA	Torsional braid analysis
DEA	Dielectric analysis
VARTM	Vacuum-assisted resin transfer molding
SMART	Stanford multi-actuator receiver transduction
SH	Shear horizontal
ToF	Time of flight
ILSS	Interlaminar shear strength
1D	One-dimensional
SWCNT	Single-walled carbon nanotube
MWCNT	Multi-walled carbon nanotube
2D	Two-dimensional
SSA	Specific surface area
GO	Graphene oxide
rGO	Reduced graphene oxide
CB	Carbon black
UTS	Ultimate tensile strength
IFSS	Interfacial shear strength
EIT	Electrical impedance tomography

GFRP	Glass fibre-reinforced polymer
EPD	Electrophoretic deposition
DCB	Double cantilever beam
EMI	Electromagnetic interference
UD	Unidirectional
AVE	Advanced video extensometer
AJP	Aerosol jet printing
FDM	Fused deposition modeling

Symbols

h	Plate thickness
k	Wavenumber
c_L	Velocity of longitudinal modes
c_p	Velocity of transverse modes
ω	Wave circular frequency
u	Displacement field
ρ	Density
λ, μ	Lamé constants
R	Electrical resistance
R_{CNT}	Resistance of CNT
$R_{Contact}$	Contact resistance
$R_{Tunnelling}$	Tunnelling resistance
F	Force to failure
d_f	Fibre diameter
$F(\sigma)$	Failure probability
σ_0	Characteristic fibre strength
β_W	Weibull modulus
ΔR	Variation in resistance
R_0	Initial resistance
G	Gauge factor
ε	Strain
σ_c	Electrical conductivity

f	Fraction of nanoparticle
f_c	Percolation threshold
t_{pt}	Constant reflecting the dimensionality of nanocomposite
$R_{Nanoparticle}$	Resistance of nanoparticle
$\alpha, \alpha(t)$	Cure degree
$H(t)$	Current reaction enthalpy
t	Time
H_T	Total reaction enthalpy
S_0	Zeroth-order symmetric Lamb wave mode
A_0	Zeroth-order anti-symmetric Lamb wave mode
σ_f	Flexural strength
P	Maximum load
L_s	Support span
d	Width of laminate
d	Depth of laminate
E_B	Modulus of elasticity in bending
m_s	Slope of load-deflection curve
β	Heating rate
T	Ambient temperature
$k(T)$	Temperature-dependent constant
$f(\alpha)$	Kinetic model
A	Pre-exponential factor
E	Apparent activation energy
R_g	Universal gas constant
T_p	Temperature corresponding to the maximum cure rate

C_g	Group velocity
L	Distance between actuator and sensor
t_e	Moment corresponding to energy envelope peak of excitation signal
t_s	Moment corresponding to energy envelope peak of received signal
t_0	Moment corresponding to impingement
Δt_i	Travel time of signal
ζ	Pixel value

TABLE OF CONTENTS

ABSTRACT	i
PUBLICATIONS ARISING FROM THE THESIS	vi
ACKNOWLEDGEMENTS	ix
NOMENCLATURE	x
TABLE OF CONTENTS	xvi
LIST OF FIGURES	xx
LIST OF TABLES	xxvii
CHAPTER 1 Introduction	1
1.1 Background and Research Motivation	1
1.2 Research Objectives	6
1.3 Scope of the Thesis	7
CHAPTER 2 State of the Art of Structural Integrity and Health Monitoring of Composites Using Guided Ultrasonic Waves: A Literature Review	11
2.1 Introduction	11
2.2 Structural Integrity and Health Monitoring of Composites	12
2.2.1 Cure Monitoring.....	12
2.2.2 In-service Monitoring.....	16
2.2.3 Summary	18
2.3 Guided Ultrasonic Wave-based Monitoring of Composites	21
2.3.1 Fundamentals of Guided Waves.....	21
2.3.2 Evaluation Approaches of Composite Status Using Guided Ultrasonic Waves.....	23

2.3.3	Sensing Approaches	25
2.4	Nanocomposite-based Sensors.....	28
2.4.1	Properties of Carbonaceous Nanomaterials	28
2.4.2	Fabrication and Performance	31
2.4.3	Summary	45
2.5	Functionalized Composites with Expanded Capacities	46
2.6	Summary	48
CHAPTER 3 Carbon Nanotube-grafted Sensing Fabrics: Development, Characterization and Applications		51
3.1	Introduction	51
3.2	Grafting of Carbon Nanotubes on Fabrics	52
3.3	Characteristics of Synthesized Carbon Nanotubes	54
3.4	Response to Guided Ultrasonic Waves	61
3.5	Tensile Properties	66
3.6	Electrical Resistance-based State Diagnosis of Composites with Carbon Nanotube-grafted Glass Fibre Sensors	71
3.7	Summary	77
CHAPTER 4 Implantable Nanocomposite Sensors		79
4.1	Introduction	79
4.2	Sensing Mechanism: Quantum Tunnelling Effect	80
4.3	Preparation of Implantable Sensors	83
4.3.1	Synthesis of Nanocomposite Ink.....	83

4.3.2	Deposition of Nanocomposite Ink on the B-stage Epoxy Film	85
4.3.3	Fabrication of Carbon Nanotube-film-made Wires.....	89
4.4	Implantation of Networked Sensors into Composites.....	94
4.5	Morphological Characterization.....	98
4.6	Summary	102
CHAPTER 5 Characterization of Composites with Implanted Sensors		103
5.1	Introduction	103
5.2	Dynamic Response Analysis	104
5.2.1	Quasi-static Tensile Loads	104
5.2.2	Medium-frequency Vibrations	107
5.2.3	High-frequency Guided Ultrasonic Waves	111
5.3	Possible Influence on Mechanical Properties of Composites	116
5.3.1	Tensile Properties	116
5.3.2	Flexural Properties	122
5.4	Summary	126
CHAPTER 6 Continuous Monitoring of Composites with Implanted Nanocomposite Sensors: From Cure to In-service.....		128
6.1	Introduction	128
6.2	Process Monitoring	129
6.2.1	Cure Kinetics of Matrix	129
6.2.2	Guided Ultrasonic Wave-based Cure Monitoring.....	136
6.3	In-service Impact Localization.....	147

6.4	Summary	150
CHAPTER 7 Conclusions and Recommendations for Future Work.....		151
7.1	Conclusions	151
7.2	Recommendations for Future Work	156
Bibliography... ..		162

LIST OF FIGURES

Figure 2.1 Schematic of the SMART layer [11].....	17
Figure 2.2 Symmetric and anti-symmetric Lamb wave modes [42].	22
Figure 2.3 Schematic of the ToF algorithm [51].	24
Figure 2.4 Schematic of carbon nanotubes [61].....	29
Figure 2.5 Schematic of graphene [61].	30
Figure 2.6 Schematic of a roll-to-roll fibre winding and dip coating process for continuously depositing carbonaceous nanomaterials on fibres [75].	35
Figure 2.7 Fabrication scheme of nonintrusive and self-sensing composites [14].	39
Figure 2.8 Schematic of an EPD process [87].	40
Figure 2.9 Schematic of a CVD set-up.	42
Figure 3.1 Preparation flowchart of GUV-responsive sensing fabrics.....	54
Figure 3.2 (a) Photograph of; and (b) TGA curves of CNT-g-GFs, with various mass fractions of CNTs.	56
Figure 3.3 SEM images showing the morphology of CNT-g-GFs with different CNT loadings.	57
Figure 3.4 Raman spectra of CNT-g-GFs.	60
Figure 3.5 TEM image of a synthesized CNT.....	61
Figure 3.6 Signals captured by CNT-g-GF sensors with different CNT loadings,	

at 175 kHz.	65
Figure 3.7 GUW signals captured by the CNT-g-GF sensors @ 0.85 wt.%, in a frequency regime from 200 to 375 kHz.	66
Figure 3.8 Schematic of single fibre tensile specimen.	67
Figure 3.9 The Weibull distribution of fracture stress of all tested specimens, with acquired characteristic strengths and Weibull moduli.	69
Figure 3.10 Stress-strain curves of composites (C ₁ -C ₃ : with a CNT-grafted fabric; O ₁ -O ₃ : without the CNT-grafted fabric); and (b) averaged tensile moduli and strengths of composites with or without a CNT-grafted fabric.	70
Figure 3.11 Fabrication of a GFRP laminate with an area CNT-g-GF sensor via the VARTM technique.	72
Figure 3.12 Variation in ER measured by the area CNT-g-GF sensor in a VARTM process: (a) entire process; (b) infusion stage; (c) equilibrium stage; (d) cure stage; and (e) morphological alteration of the CNT-g-GF sensor in different stages.	74
Figure 3.13 A laminate with the CNT-g-GF sensor for sensing in-service loads.	76
Figure 3.14 Variation in the ER measured by the CNT-g-GF sensor when the laminate is subject to a quasi-static load.	77
Figure 4.1 Schematic diagram of the quantum tunnelling effect.	82
Figure 4.2 Flowchart of the preparation process of the sprayable CPC ink.	84

Figure 4.3 Correlation between σ_c of CPCs and loadings of GNPs.	85
Figure 4.4 Fabrication of the B-stage Epoxy Film.	87
Figure 4.5 Heat flow and cure degree vs. time measured by DSC @ 130 °C... ..	87
Figure 4.6 Comparison of ink deposited-epoxy films processed with different pre-treatments.	89
Figure 4.7 Morphology and ER of tried mediums to make the wires.	90
Figure 4.8 (a) Photograph (DexMat [®]); and (b) SEM image of the CNT-film. .	91
Figure 4.9 Flowchart of the fabrication process of implantable sensors.	93
Figure 4.10 Photograph of fabricated nanocomposite sensors, with a sensor wrapped on a thin rod (diameter: 8mm) showing the good flexibility of the sensor.	94
Figure 4.11 Schematic of a CFRP laminate with an implanted sensor network.	96
Figure 4.12 The applied consumable lay-up in the autoclaving cure cycle.	96
Figure 4.13 A CFRP laminate with four implanted nanocomposite sensors: (a) under preparation; and (b) in its finished fashion.	97
Figure 4.14 SEM images of the GNPs/PVP nanocomposite sensor, at two different scales.	99
Figure 4.15 (a) Cross-sectional view of a CFRP laminate with an implanted sensor and wires; (b) an individual implantable sensor.	100
Figure 4.16 (a) Vicinity of the implanted sensor; and (b) the interface between	

the implanted sensor and host composite.....	101
Figure 5.1 (a) Set-up for measuring the strain in the laminate under a quasi-static load; (b) gauge points on the laminate for AVE measurement, beneath which the sensor is implanted; and (c) the junction of the implanted sensor to the multimeter.....	105
Figure 5.2 (a) Stress/ER changes vs. strain; and (b) strain/ER changes vs. time under a quasi-static tensile load.	106
Figure 5.3 Schematic of set-up for acquiring dynamic responses in the vibration test.	108
Figure 5.4 Responses of a CFRP laminate with an implanted sensor to vibrations at (a) 100; (b) 500; and (c) 1000 Hz.....	109
Figure 5.5 Schematic of set-up for acquiring GUW signals propagated in the laminate.....	112
Figure 5.6 Signals captured by a nanocomposite sensor randomly selected from the implanted sensor network and by the PZT wafer, at (a) 200 kHz; and (b) 450 kHz.	114
Figure 5.7 Spectra over time-frequency domain up to 450 kHz, perceived by (a) the nanocomposite sensor; and (b) the PZT wafer.	115
Figure 5.8 Schematic of a CFRP laminate implanted with a nanocomposite sensor (with two CNT-film-made wires) for tensile test.....	117
Figure 5.9 The universal testing platform used in the tensile test.....	117

Figure 5.10 Results of tensile test: (a) stress-strain curves of CFRPs with or without implanted sensors (I₁-I₅: with implanted sensors; O₁-O₅: without any implanted sensor); and (b) averaged UTS and Young’s modulus of laminates with or without sensor implantation..... 119

Figure 5.11 (a) A fractured laminate with an implanted sensor; (b) the fracture region in (a); and (c) the fracture region of a counterpart laminate without sensor implantation. 120

Figure 5.12 Schematic of a CFRP laminate implanted with a nanocomposite sensor (with two CNT-film-made wires) for bending test. 123

Figure 5.13 (a) Load-displacement curves; and (b) flexural properties of FRPs with and without implanted sensor (O₁-O₃: without implanted sensor; I₁-I₃: with implanted sensor). 124

Figure 5.14 Fracture regions of (a) a counterpart laminate without the sensor; and (b) a laminate with an implanted sensor, with the zoomed-in fracture region in (c). 125

Figure 6.1 DSC curves of the prepreg at the heating rates of 1.0, 1.5, 2.0, 3.0 and 4.5 K/min, respectively..... 130

Figure 6.2 (a) Kissinger plot for determining E and $\ln A$; and (b) plot of $y(\alpha) = \frac{d\alpha(t)}{dt} e^{\frac{E}{RT}}$ versus cure degree ($\alpha(t)$) at different β 134

Figure 6.3 (a) Cure rate ($\frac{d\alpha(t)}{dt}$) versus cure temperature; and (b) cure degree ($\alpha(t)$) versus cure temperature at different β (solid line: Sesták–Berggren

model-predicted results; symbol: experimental results).	135
Figure 6.4 Experimental set-up for GUW-based cure monitoring.....	138
Figure 6.5 Representative GUW signals captured by an implanted sensor, along with wave energy envelopes, at different temperatures with the heating rate of 1.5 K/min.	139
Figure 6.6 Group velocity of S_0 wave mode at different cure temperatures, corresponding to different cure degrees.	141
Figure 6.7 (a) Measured C_g of GUWs <i>versus</i> cure degree of matrix; and (b) Equation 6.11-predicted correlation between cure degree of matrix and C_g of S_0 wave mode, compared with experimental results.	142
Figure 6.8 Schematic of the prepregs cured with a heating anomaly.....	144
Figure 6.9 (a) Group velocity of S_0 wave mode after the gel point of matrix (at the heating rate of 2 K/min); and (b) comparison of C_g measured in normal and abnormal cure areas (solid line: Sesták–Berggren model and Equation 6.11-predicted results; symbol: experimental results).....	146
Figure 6.10 (a, b) Representative raw and processed AE signals acquired with S_3 and S_5 ; and (c) comparison between the real impact spot and the identified spot.	149
Figure 7.1 AM-driven approaches for fabricating (a) sensing units via AJP; and (b) wires/circuits via FDM.	160
Figure 7.2 Schematic of an AM-driven integratable sensing network layer. ..	160

Figure 7.3 Implantation of the sensing network layer in CFRPs. 161

LIST OF TABLES

Table 2.1 Capabilities of main CM techniques to detect cure characteristics. . .	19
Table 2.2 Capabilities of main SHM techniques to detect representative defects [32].	20
Table 4.1 Cure degree vs. heating duration.	87
Table 4.2 Key parameters of CNT-film-made wires.	92
Table 4.3 Key parameters of a standard autoclaving cure cycle.	95
Table 6.1 Determined parameters in Sesták–Berggren autocatalytic kinetic model.	136

CHAPTER 1

Introduction

1.1 Background and Research Motivation

In virtue of superior mechanical attributes, fibre-reinforced polymer (FRP) composites have attained their maturity to serve as primary load-bearing structural components, in lieu of conventional metallic materials [1]. The quality of a finished composite structure is closely related to the manufacturing process of the composite. During the cure, the polymer matrix undergoes sequent phases, from an uncured liquid state, through the transient rubbery state to the cured glassy solid state [2]. Additionally, it is essential to understand the infusion states of epoxy resin to avoid the presences of dry spots, unsaturated infiltration regions and resin pockets. To entertain the quality demand for composite structures, it is imperative to implement cure monitoring (CM) in an *in situ* and on-line manner.

On the other hand, an in-service composite structure is often exposed to harsh environments, such as fluid contaminants, moisture ingress, cyclic thermal loadings,

ultraviolet radiation, *etc.* On top of that, an out-of-plane impact commonly introduces barely visible impact damage (BVID) to the composite structure. Therefore, it is essential to perform structural integrity monitoring (SIM) of composites in an efficient, reliable and robust way.

In conclusion, continuous monitoring of composites, spanning their entire life cycle, is of vital importance. As the most rudimentary yet pivotal element in a monitoring approach, sensors (or elaborately configured sensor networks) are integrated with FRPs, for capturing ambient variations and structural changes, on which basis the variations in material integrity can be characterized. To meet such a demand, prevailing sensors, which can be used to fulfill monitoring of composites with distinct sensing philosophies, broadly embrace acoustic emission (AE) sensors [3], accelerometers [4], strain gauges [5], fibre Bragg grating (FBG) sensors [6], interdigital transducers (IDTs) [7], polyvinylidene fluoride (PVDF) film sensors [8], lead zirconate titanate (PZT) wafers [9], among others.

These sensors, of whatever kind, are immobilized with FRPs via either surface mounting [3, 10] or internal embedding [11, 12], each possessing respective merits and demerits. Depending on applications, the selection of a proper means to immobilize sensors in composites is somewhat debatable. Surface mounting is preferred when the convenience in sensor installation, ease of maintenance and low

replacement cost are priority considerations. Nonetheless, it is increasingly challenging to faithfully acquire the signals as sensors are directly exposed to the environment and prone to the ambient noise. This concern is particularly accentuated for FRPs used in rugged working conditions such as the composite-made load-bearing structures in aircraft.

In contrast to the surface attachment, internal embedment of sensors has advantages when isolation of sensors from the environment is of necessity. As a consequence of the reduced exposure to ambient, the embedded sensors usually offer a high signal-to-noise ratio due to enhanced immunity to measurement noise, along with guaranteed quality of long-term signal acquisition. Internal embedment of sensors is also conducive to preventing detachment of sensors from composites owing to reasons such as adhesive degradation or environmental attacks (*e.g.*, moisture and corrosion). Additionally, embedded sensors are in general more sensitive to internal damage than surface attached sensors are [12]. Even though, conventional embedded sensors, such as rigid PZT wafers or brittle FBG sensors, inevitably reduce the strength of host structures, though their intended role is to perform monitoring [13]. In addition to the embedded sensors themselves, the associated wires/cables and electrodes simultaneously intensify the degradation of structural integrity [3]. Besides, for composites reinforced by conductive fibres (*e.g.*, carbon and aluminum), the short-circuit of sensors and wires by fibres is another thorny issue. Other

challenging issues arising from sensor embedment, in comparison with surface mounting, also include the ease in breaking vulnerable cables (used for linking sensors to external signal acquisition equipment) during edge-trimming and the impossibility to access or replace embedded sensors during maintenance.

Furthermore, PZT wafers, rigid and brittle, are inadaptable to a curved structure, while FBG sensors are in general not sensitive to damage far from their vicinity [14]. Due to their high sensitivity to moisture and chemicals, FBG sensors need to be protected by polymer sheaths which may introduce localized mechanical weak points to composites. Together, all these factors can significantly undermine the original integrity of composites, cause premature failures and jeopardize the implementation of monitoring which initially targets to enhance the structural reliability.

On the other hand, the recent advances in nanotechnology and additive manufacturing (AM) have ushered in a promising avenue to implement monitoring of composites in conjunction with nanocomposite-based sensors, whereby the intrusion to composites can be minimized. Other appealing merits, derived from the use of nanocomposite-based sensors, include reduced producing cost, standardized fabrication procedure as well as accurate sensor alignment and positioning. However, most monitoring approaches in this domain lie in the premise that change in resin consolidation or occurrence of damage in composites alters the electrical resistance

(ER) measured by nanocomposite-based sensors. These approaches may fail to provide quantitative estimation – that is because the change in ER only holistically reflects the alteration in material between the two electrodes of the measured nanocomposites – that is global information on the overall change in structural integrity.

In contrast to scrutinizing global changes in electrical properties, guided ultrasonic waves (GUWs) of high frequency carry fairly localized information that is accumulated along wave propagation paths. GUWs enable the quantitative estimation of cure progress (during manufacturing) or integrity degradation due to damage (in service) even if the damage is distant from sensors. GUWs also offer much higher sensitivity to material degradation of small scale owing to their short wavelengths, compared with those approaches using global information (*e.g.*, electrical impedance). Conventional GUW-based monitoring is regularly implemented in conjunction with the use of PZT-type wafers for GUW generation and acquisition, embedment of which unavoidably degrades the original structural integrity of host composites as commented earlier. As far as nanocomposite-based sensors are concerned, though they may not inflict remarkable intrusion on composites, this sort of sensors usually fails to respond to high-frequency GUWs, because GUWs are of high frequency (of several hundred kHz or even MHz) yet

ultralow magnitude (of the order of micro-strain, even nano-strain) – beyond the responsivity of ordinary nanocomposite-based sensors.

In conclusion, though significance of monitoring for composite structures cannot be overemphasized, it is still a vast challenge to implement continuous monitoring of composites in a quantitative manner, but without detrimental impact on composites due to integration of the sensing system.

1.2 Research Objectives

Aimed at circumventing the above commented deficiencies in prevailing GUV-based monitoring techniques for composite materials, this PhD research is dedicated to developing a new sort of nanocomposite-based sensors, which can be integrated into composite structures to be sufficiently sensitive to GUVs, for implementing *in situ* cure monitoring and in-service health monitoring of the host composites. Driven by this target, the following objectives are set:

- 1) to develop new genres of nanocomposite-based sensors that can be integrated into fibre-reinforced polymer composites;
- 2) to tailor the nanostructure of nanocomposites to promote the sensitivity of sensors;

- 3) to assess the sensitivity of thus-integrated sensors towards strains induced by quasi-static loads, medium-frequency structural vibrations and high-frequency GUWs;
- 4) to design and provide a high-quality signal communication system (including electrodes and wires), with minimized intrusion on host composite structures;
- 5) to investigate the possible degradation in mechanical attributes of host composite structures due to the sensor integration;
- 6) to prove the capacity of nanocomposite-based sensors in cure monitoring during manufacturing;
- 7) to evaluate the in-service health monitoring capability of the same type sensors.

1.3 Scope of the Thesis

This PhD study is dedicated to developing new kinds of integratable nanocomposite sensors which are capable of perceiving dynamic strains with a frequency up to several megahertz, to implement GUW-based monitoring of composites from manufacturing onset through service. This thesis is organized in the sequence of design philosophy, sensor preparation and integration, performance characterization and application validation.

A brief literature review related to current progresses in CM and SIM approaches and integrated nanocomposite sensors is reported in Chapter 2. The importance and merits of CM and SIM are highlighted, followed with summaries on achievements and limitations of current studies. Illustrations on broadly adopted methods to prepare nanocomposite sensors and their performance are recapped. Another emphasis is placed on the development of integrated functional composites, with which work arising from this study finds its potential applications.

To hierarchically develop FRPs with integrated self-sensing and monitoring capabilities, Chapter 3 initially elaborates on the preparation, characterization and application of a new type of sensing fabric. Carbon nanotubes (CNTs) are grafted on glass fibre (GF) fabrics via chemical vapor deposition (CVD) at a low CNT growth temperature (500 °C), to make CNT-grafted GF sensors, denoted as CNT-g-GF sensors in what follows. Scanning electron microscopy (SEM), transmission electron microscopy (TEM), thermo gravimetric analysis (TGA) and Raman Spectroscopy are introduced to characterize the synthesized CNTs. Single fibre tensile test (ASTM C1557) and fibre-reinforced polymer matrix composite tensile test (ASTM D3039) are performed to interrogate the probable degradation, induced by CVD process, in tensile strength. The loadings of CNTs are comprehensively tailored to enhance the quantum tunnelling effect and thus make the CNT-g-GF sensors responsive to GUWs. Such sensors enable ER-based continuous monitoring, to correlate measured

ER with different stages of curing epoxy resin and in-service applied loads, respectively.

Chapter 4 demonstrates the design philosophy and the entire fabrication process of another type of nanocomposite sensor, which can be implanted into composites reinforced by conductive carbon fibres (CFs). To prepare such sensors, aqueous nanocomposite ink made of graphene nanoplatelets (GNPs) and polyvinylpyrrolidone (PVP) is regulated to obtain the percolation threshold of conductive polymer nanocomposites (CPCs). Thus-prepared ink is sprayed on a partially precured dielectric epoxy film via spray coating. Highly conductive carbon nanotube film (CNT-film)-made wires are fabricated to electrify the sensors for signal transmission. Upon fully cured, the sensors are implanted into 8-ply quasi-isotropic carbon fibre-reinforced polymer (CFRPs) composites. The morphology of such nanocomposite sensors and CFRPs with implanted sensors is interrogated at microscale to have a preliminary assessment of their performance.

The responses of CFRPs with implanted sensors towards quasi-static loads, medium-frequency vibrations and high-frequency GUVs are reported in Chapter 5. On top of that, the possible intrusion to host structures, induced by implantation of nanocomposite sensors, is scrutinized via the tensile and flexural tests, according to the ASTM standards.

With proven sensing performance, nanocomposite sensors reported in Chapter 4 are implanted into composites to implement continuous monitoring from manufacturing through service, in Chapter 6. The cure kinetics of matrix are first understood via the differential scanning calorimetry (DSC) and a Sesták–Berggren autocatalytic kinetic model. After that, the cure progress of composites is *in situ* evaluated by the implanted sensors, based on the established correlation between the propagation traits of GUWs and cure degree of matrix. The same type of implanted sensor is subsequently introduced to perform in-service structural health monitoring (SHM), in which a transient impact to the composite is localized and imaged.

At the end, Chapter 7 serves as the conclusion of the thesis, along with given recommendations for the future study.

CHAPTER 2

State of the Art of Structural Integrity and Health Monitoring of Composites Using Guided Ultrasonic Waves: A Literature Review

2.1 Introduction

This chapter reviews the pivotal issues which are associated with guided ultrasonic wave (GUW)-based cure monitoring (CM) and structural health monitoring (SHM), along with recent developments in nanocomposite-based sensors. The significance and achievements in both CM and SHM are reviewed in this chapter, to give a glance at the dilemmas suffered by current CM and SHM approaches. The requirements of an ideal CM or SHM technique are respectively concluded, to which this PhD study strives to achieve. The fundamentals of GUWs and evaluation approaches of composite status using GUWs are recapped briefly. This chapter further reviews the integratable nanocomposite sensors, according to their distinguished integration

forms. In particular, the major limitation of most nano-engineered sensors is pointed out, revealing the fact that sensors in this category are only able to perceive low-frequency dynamic strains, with which this study has been motivated. This chapter ends up with recent advances in integrated functional composites, with emphasis placed on their functionalities, to explore the potential applications of work arising from this study.

2.2 Structural Integrity and Health Monitoring of Composites

2.2.1 Cure Monitoring

The quality of composites is associated with the manufacturing process and a cure schedule of an in-process composite structure is generally carried out based on the recommendations provided by the material supplier [2]. On the other hand, defects in various forms can be introduced into composite structures during preparation. For example, composites fabricated using prepreg-type materials may face the problem of the excessive residual strain, as such materials are commonly cured using an autoclaving process under high temperature and pressure. The cure anomaly of prepreps would cause warping of thus-cured composite components. On the other hand, to meet the increasingly stringent energy consumption and carbon emission standards, alternative manufacturing techniques (*e.g.*, resin transfer molding (RTM))

and hand lay-up) are now in intensive use. However, composites fabricated using these techniques usually contain preparation flaws such as resin pockets, dry spots or voids. Therefore, to meet the demand of high-quality composites, it is necessary to implement CM of composites to optimize the manufacturing strategy and thus guarantee the quality of fabricated composites.

The initial efforts to implement CM of epoxy resin are mainly limited to laboratorial environments and are not yet ready for industrial applications. These techniques broadly embrace differential scanning calorimetry (DSC) [15], Fourier transform infrared spectroscopy (FTIR) [16], dynamic mechanical analysis (DMA) [17] and torsional braid analysis (TBA) [18]. Other practical approaches developed to implement CM in an *in situ* and on-line manner include the dielectric analysis (DEA) [19], acoustic emission-based CM [20], fibre optics system [21] and ultrasonics-based CM techniques [22, 23]. Each of these conventional techniques owns merits and demerits.

For CM performed using fibre optics, there are two different types: the Fresnel's reflection and strain monitoring. Fibre optics, operating in virtue of Fresnel's reflection, records the change in refractive index between the fibre end and resin, in conjunction with a laser diode and a photo detector. Such a type of sensor can detect the increase in the refractive index under the isothermal cure circumstance and trace

polymerization. Nonetheless, such a method is restricted to isothermal cure conditions, under which the temperature effect on the refractive index is minimized [24]. On the other hand, fibre Bragg grating (FBG) sensors can also be adopted to measure strains induced by the thermal expansion and cure shrinkage of resin in a cure process [25]. The residual strain at the end of cure can be referred as an indicator to estimate the quality of composite components, as higher residual strains are commonly considered to be detrimental.

Dielectric analysis is another well established *in situ* CM technique, which provides indirect measurement of cure in terms of viscosity of the resin in a cure [26]. Such an approach lies in the fact that as the cure progresses, the mobility of polar groups in resin decreases, and therefore the dielectric constant of resin and the impedance of the sensor change accordingly, with which the cure stage of resin is related to the impedance of the sensor [27]. The dielectric measurement for implementing CM is generally in conjunction with the application of sinusoidal voltage excitation, upon which the frequency-dependent dielectric properties of resin can be determined via the Fourier transform of the acquired current waveform [19].

Ultrasonics-based CM is generally fulfilled by measuring and interpreting the velocity and attenuation of guided ultrasonic waves (GUWs) to reflect the cure state of resin in a cure process [28]. Two categories of ultrasonics-based CM methods

exist, namely measuring compression waves in a transmission mode and measuring shear waves in a pitch-catch mode. When ultrasonics-based techniques are introduced to perform CM of large-scale structures, the pitch-catch measuring mode is preferred, as such a method brings more information of monitored resin along the propagation path [29].

Chilles *et al.* [30] used an inductively coupled embedded lead zirconate titanate (PZT) sensor to measure both the velocity and magnitude of guided waves in a cure process. The authors demonstrated that the ultrasonics-based CM technique showed a higher sensitivity to the final post-cure stage, compared with conventional DSC and DEA. Such an inductively coupled sensor also exhibited its structural health monitoring (SHM) capability via detecting a barely visible impact damage (BVID). Without requirements of the wiring system and the control unit, the sensing system brings limited weight addition and intrusion to the host structure, while the manual signal generation and collection is required. Liu *et al.* [31] also used an embedded piezoelectric sensor network to monitor the resin flow front and the cure degree of resin in a vacuum-assisted resin transfer molding (VARTM) process, via interpreting the propagation characteristics of Lamb waves and the electromechanical impedance of the PZT wafer.

2.2.2 In-service Monitoring

BVID caused by a transient impact and the adhesive debonding commonly observed at the lap joints are two representative failure modes [32]. On top of that, harsh environmental conditions (*e.g.*, various fluid contaminants, moisture ingress, cyclic thermal loadings and ultraviolet radiation) generally induce damage in other various forms [32]. Therefore, it is essential to implement SHM of composites with an efficient, reliable and robust sensing system.

Strain measurement-based monitoring, using surface-mounted or internally embedded strain gauges, is a routine and cost-effective approach [32]. Strain gauges do not detect local damage directly, but can give an indication to reflect the health state of monitored structures through strain mapping.

Ultrasonics-based SHM measures and interprets the transmission and/or the reflection of pulsed elastic waves in engineering composites. In this connection, Su *et al.* [33-35] used built-in miniaturized circuited wafers to locate and gauge delamination in carbon fibre-reinforced polymer (CFRP) laminates via investigating propagation attributes of Lamb waves. The proven delamination identification capability indicates the potential of such embedded sensor networks in SHM for composite aircraft structures. To integrate essential components of a sensing system (*e.g.*, actuators, receivers, circuits and electrodes) and reduce the intrusion to

structures, the Stanford Multi-Actuator Receiver Transduction (SMART) layer, as shown in Figure 2.1 – one of the most broadly used integrated sensor networks, was developed and applied in both CM and SHM [11, 36, 37], with high compatibility with various composite fabrication techniques (RTM, filament winding, autoclaving, *etc.*). Impact identification with quantifications of force and location, in a passive mode, and damage detection with assessment in its severity, in a pitch-catch mode, were achieved with the SMART layer [36, 38, 39]. Multiple SMART layers can be co-embedded in a single composite component to extract rich health information of the monitored structure. Qing *et al.* [39] built in-plane and through-thickness sensing paths in a filament-wound composite vessel and scanned the entire vessel to estimate severity of impact-induced damage. With the proven monitoring capability, such a system was further developed in commercial exploitation and named SMART suitcase [38].

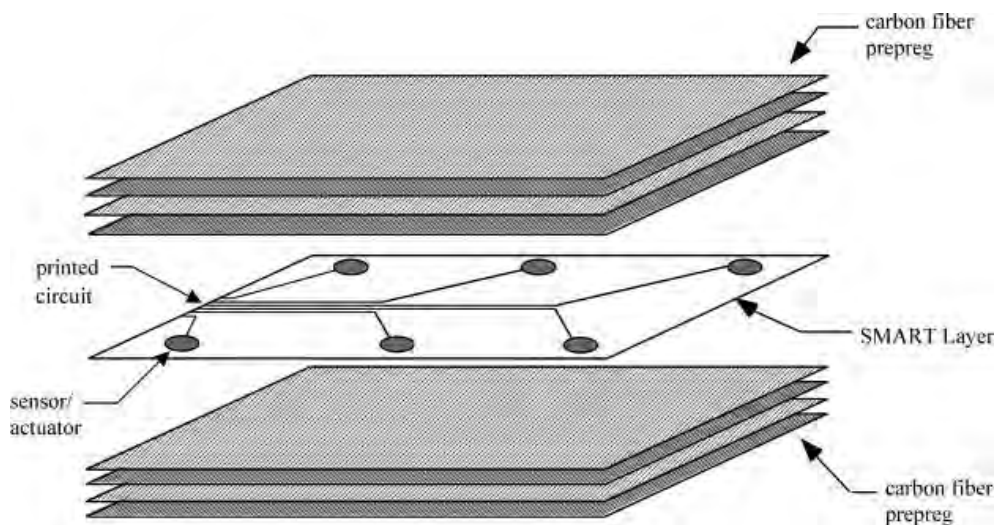


Figure 2.1 Schematic of the SMART layer [11].

Andreades *et al.* [12] fabricated three types of specimens, each containing a pair of PZT wafers at different locations, to compare the sensitivity of surface-mounted and embedded PZT sensors to internal mocked-up delamination made of two layers of release films. GUVs would excite and vibrate the debonding region and thus generate second harmonic which was used to detect and estimate damage. Presence of the second harmonic confirmed the existence of delamination and with the same excitation, the magnitude of the second harmonic received by the embedded PZT sensor was an order of magnitude higher than that received by the surface-mounted PZT sensor, indicating the higher sensitivity of embedded sensors to internal damage.

2.2.3 Summary

As commented in Section 2.2.1, there exist several mature CM techniques which have already demonstrated their applications in engineering practice, to partially or fully achieve detections of cure characteristics listed in Table 2.1. In brief, a desired CM technique is expected to be able to characterize the infusion, gel point and cure degree of resin, accompanying with capabilities to detect the cure anomaly, dry spots, resin pockets, *etc.*

Table 2.1 Capabilities of main CM techniques to detect cure characteristics.

Cure Characteristic \ Method	Resin Fill	Gel Point	End of Cure	Cure Degree	Post Cure
Acoustic Emission	✓	✓	✓	✓	✗
Ultrasonics	✓	✓	✓	✓	✓
Dielectric Analysis	✓	✓	✓	✓	✓
Fibre Bragg Grating	✗	✓	✓	✗	✓

As seen in Table 2.1, ultrasonics-based CM approach fulfill recognitions of all concerned cure characteristics, being one of the most ideal techniques. Therefore, a GUW-based CM approach would offer following merits to assist in improving the quality of thus-fabricated composites:

- i) tailoring the cure schedule to suit the age and the chemical integrity of resin as prepregs are pre-catalyzed and start to cure the moment at which they leave the manufacturing line;
- ii) detecting the cure anomaly that results in inconsistent residual strains of cured composites, with which matrix crack, delamination or warping may be induced [40];
- iii) indicating the cure degree and the completion of the resin cure to reduce both time and energy costs of a cure cycle.

On the other hand, all the commented CM techniques can be extended to perform in-service SHM and fulfill life cycle monitoring of composites. Table 2.2 compares

capabilities of main SHM techniques to detect representative defects, demonstrating the superiority of the ultrasonics-based SHM approach.

Among the different approaches listed in Table 2.2, disadvantages of using dielectric analysis in practice include: 1) restricted to localized measurement which could only provide limited health information of monitored structures; and 2) the intrusive nature of such metallic-type dielectric sensors [41]. Though FBG sensors feature merits such as the high sensitivity and broadband response performance, such sensors also show following demerits: 1) due to their high sensitivity to moisture and chemicals, FBG sensors need to be protected by polymer sheaths which may introduce local mechanical weak points into host composite structures; 2) the brittle nature of FBG sensors requires extra caution during embedment, complicating the fabrication process; and 3) such sophisticated sensors require expensive instrumentation for the analysis of signals.

Table 2.2 Capabilities of main SHM techniques to detect representative defects [32].

Method \ Defect Type	Delamination	Voids	Debonding	Cracking
Ultrasonics	✓	✓	✓	✓
Acoustic Emission	✓	✗	✗	✓
Dielectric Analysis	✗	✗	✗	✓
Fibre Bragg Grating	✓	✗	✓	✓

2.3 Guided Ultrasonic Wave-based Monitoring of Composites

2.3.1 Fundamentals of Guided Waves

Elastic waves in a solid medium can be one of the modalities (*e.g.*, Rayleigh waves, Lamb waves, Stonely waves and Creep waves), distinguished by the motion of particles [42]. Particularly, Lamb waves, which refer to elastic waves propagating in thin plates, will be adopted in this study as the developed integrated composites feature planar dimensions much greater than that of thickness [43].

Lamb waves, as shown in Figure 2.2, can be described by following two equations [44]

$$\frac{\tan(qh)}{\tan(ph)} = -\frac{4k^2qp}{(k^2 - q^2)^2} \text{ for symmetric modes,} \quad 2.1$$

$$\frac{\tan(qh)}{\tan(ph)} = -\frac{(k^2 - q^2)^2}{4k^2qp} \text{ for anti-symmetric modes,} \quad 2.2$$

$$p^2 = \frac{\omega^2}{c_L^2} - k^2, \quad q^2 = \frac{\omega^2}{c_T^2} - k^2 \text{ and } k = \omega / c_p,$$

where h is the plate thickness, k the wavenumber, c_L the velocity of longitudinal modes, c_p the velocity of transverse modes and ω the wave circular frequency. Equations 2.1 and 2.2 imply that Lamb waves are dispersive (*viz.* their velocity dependent on frequency), in spite of their modes.

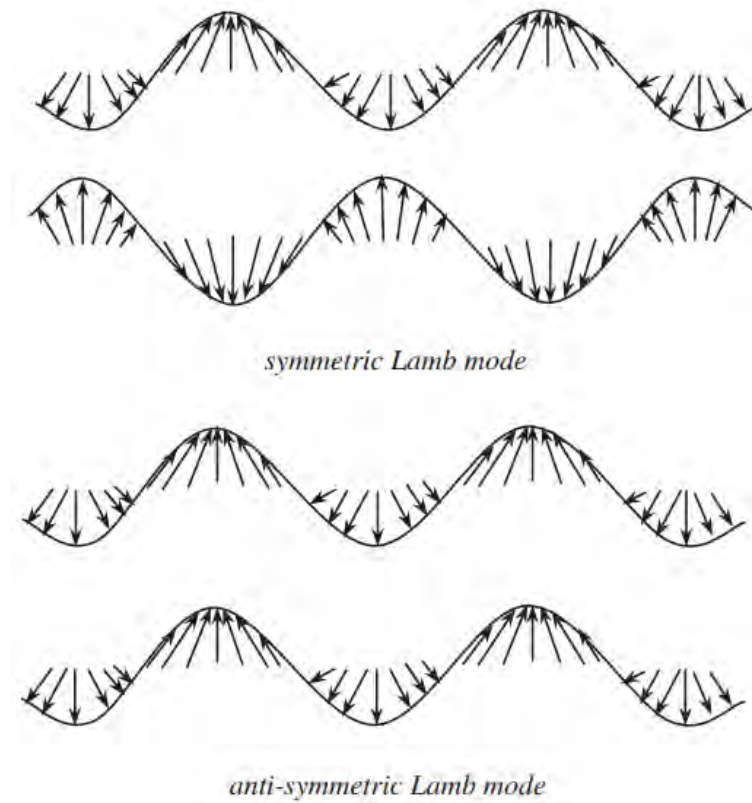


Figure 2.2 Symmetric and anti-symmetric Lamb wave modes [42].

On top of that, a transverse motion, distinguished from vertical shear waves, was first observed by Love in 1911. Such a mode was named as the shear horizontal (SH) mode and is co-employed with Lamb modes in many damage identification schemes [33].

On the other hand, the intrinsic anisotropic properties of composite laminates bring interesting yet complicated propagation attributes of Lamb waves. For an N -layered composite laminate, Lamb waves could be described by the displacement field (u), which satisfies the Navier's displacement equation in each layer [45]

$$\mu^n \nabla^2 u^n + (\lambda^n + \mu^n) \nabla(\nabla \cdot u^n) = \rho^n \frac{\partial^2 u^n}{\partial t^2}, (n = 1, 2, \dots, N) \quad 2.3$$

where ρ_i the density, λ_i and μ_i the Lamé constants of the i^{th} ply. When applying the boundary conditions at free surfaces and $N-1$ interfaces to Equation 2.3, a comprehensive dispersion equation can be acquired

$$|A(\omega, k, \lambda^n, \mu^n, h_n)| = 0, \quad 2.4$$

where the frequency (ω) of Lamb waves relates to the wavenumber (k) and the geometrical feature of the plate (h_n), for a concerned material (λ^n, μ^n).

2.3.2 Evaluation Approaches of Composite Status Using Guided Ultrasonic Waves

GUW-based monitoring techniques have become one of the most predominant monitoring approaches owing to the advantages described in Section 2.2. To determine the health status of the monitored structure, the acquired and processed GUW signals are generally utilized as the input of a proposed algorithm [46]. In an algorithm, the linear features of the captured GUW signals are commonly extracted to fulfill damage detection, which assumes that damage, if exist, would influence the propagation of GUWs. The linear features of GUWs mainly contain wave reflection [47], wave scattering [47], mode conversion [48] or energy dissipation [49]. According to the extracted feature, several damage detection approaches have been proposed, as typified by approaches based on time-of-flight (ToF) [50], signal correlation [48] and signal energy [49]. Specifically, the ToF-based methods

generally utilize the waves which reflect or scatter from the damage. Taking a composite plate as an example, in Figure 2.3, the mock-up damage (simulated by a bonded mass with a radius of 10 mm and a mass of 200 g) can act as a secondary wave source [51]. In the captured signals, an additional wave packet would present behind the first arrival wave component in the time domain, as the scattered waves go through a longer propagation path than the first arrival wave component. With a configured sensor network, the information, reflecting the differences in arrival time (*i.e.*, ToF) and provided by multiple available actuating-sensing paths, can perform damage localization [52].

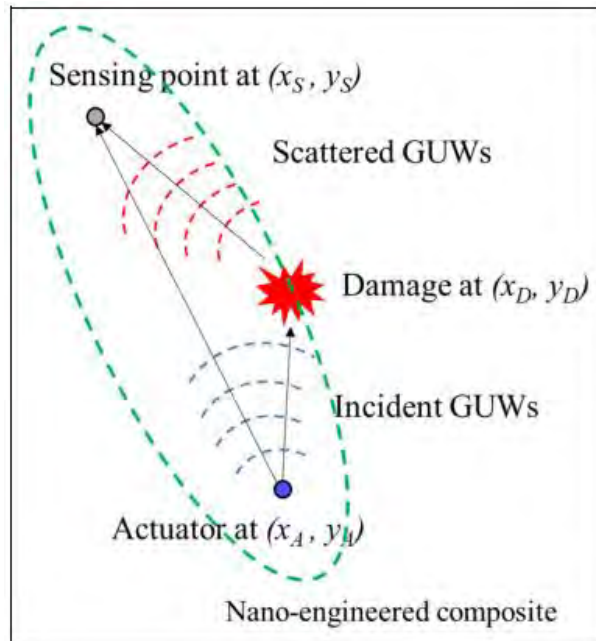


Figure 2.3 Schematic of the ToF algorithm [51].

The signal correlation-based approaches generally compare the correlation of captured signals between the original healthy status and the current monitored status. Taking a rod as an illustration, a crack in the propagation path of the probing wave would result in the decrease in wave transmission and mode conversion [53]. Consequently, a smaller value of correlation means a more severe damaged status of the rod. The signal energy-based approach measures the energy sum in the specified time duration. A representative application of damage detection is the dissipation of wave energy due to the bolt loosening [49].

With extensive efforts on GUV-based SHM, some of diagnostic approaches, relying on extracting and interpreting the linear features of GUVs, have been commercialized and applied in practical engineering applications [54]. In summary, the variations in linear features of GUVs are discernable when the size of damage is of the same order as or larger than the probing wavelength.

2.3.3 Sensing Approaches

Sensors, employed to implement advanced and robust GUV-based monitoring, broadly include but are not limited to polyvinylidene fluoride (PVDF) film sensors, PZT wafers and FBG sensors. The external deployment of these sensors may be cumbersome, let alone aforementioned degradations in stability, durability and repeatability of long-term signal acquisition. Recently, the internal embedment of

sensors attracts attention to improve the durability and accuracy of measurement [30], along with the isolation of moisture, corrosion and impact. More importantly, the embedment of sensors from the very beginning of manufacturing provides the possibility for *in situ* CM, to extend the monitoring span of composites.

When above conventional ultrasonic sensors are embedded in composites, it is conceivable that sensors would downgrade mechanical properties of host structures, though their original intention is to perform monitoring. Konka *et al.* [13] also confirmed that the embedment of a PZT wafer remarkably reduced the interlaminar shear strength (ILSS) of fibre-reinforced polymer (FRP) composites by up to 15%, along with the observation that the premature failure initiated from the PZT wafer edge. This can be attributed to significant differences in mechanical properties between the PZT materials and the composites, which discontinue strains at sensor interfaces and engender high stress concentration therein.

Additionally, the associated wires/cables and electrodes also intensify the structural integrity degradation. Xiao *et al.* [3] examined the influence of embedded metallic materials on tensile properties of carbon fibre-reinforced polymers (CFRPs), revealing that delamination at interfaces between the metal and the matrix was the key damage, which implied that embedding conventional metallic wires may result in integrity degradation of composites. When sensors are deployed in CFRPs, they

have to be encapsulated with dielectric layers to be isolated from conductive carbon fibres (CFs). Such an insulating measure, however, further compromises the integrity of composites. Generally, dielectric films such as the polyimide (Kapton) [11, 55] are used to insulate sensing systems from conductive fibres. However, the dielectric films, though thin, can alter the microstructure of a fibre-reinforced matrix, influence the interlaminar stress distribution in sensor vicinity, introduce artificial defects and consequently lower the load-carrying capability of structures. Andreades *et al.* [12] demonstrated that both flexural and compression strengths of CFRPs decreased by 8% and 12%, respectively, due to embedded transducers coated with polyimide films.

Though the robustness and the efficiency of conventional embedded sensing approaches have been well demonstrated, their potential intrusion to host structures should not be neglected. In summary, a desired integrated sensing system should meet following requirements:

- i) the embedment of sensors, associated wires and electrodes should not be at the cost of the original integrity of host composites;
- ii) the system should be able to quantitatively estimate the presence, nature, location and severity of damage;
- iii) the stability, durability and repeatability of long-term signal acquisition should be guaranteed.

2.4 Nanocomposite-based Sensors

On the other hand, nanocomposites, which exhibit flexible, lightweight and ductile, are now being broadly employed as sensing elements to implement both CM and SHM of composite materials.

2.4.1 Properties of Carbonaceous Nanomaterials

Carbon Nanotubes

Carbon nanotubes (CNTs), one-dimensional (1D) carbonaceous nanomaterial, can have an aspect ratio larger than 1000 [56]. Such a material can be regarded as cylinders which are made up of rolled-up graphite planes [57, 58], as schematically shown in Figure 2.4. Depending on the number of graphene layer, there are two categories of CNTs: single-walled CNTs (SWCNTs) and multi-walled CNTs (MWCNTs). Specifically, MWCNTs consist of two or more layers of graphene sheets that coaxially arrange around a hollow core via van der Waals forces. In each layer, carbon atoms are chemically bonded via sp^2 carbon-carbon bonds, which endow CNTs with excellent mechanical properties. Outperforming most carbon allotropes, both the theoretical and experimental results show that the Young's modulus and tensile strength of CNTs reach 1.2 TPa and 50-200 GPa, respectively [59]. Besides the superb mechanical properties of CNTs, electrical conductivities of SWCNTs and MWCNTs are as high as 10^4 – 10^8 S/m and 10^5 – 10^7 S/m, respectively,

which offer CNTs potential in developing property-enhanced or multifunctional composites. CNTs were first synthesized in 1991, after that, several methods developed to produce CNTs include discharge, laser ablation and chemical vapor deposition (CVD) [60].

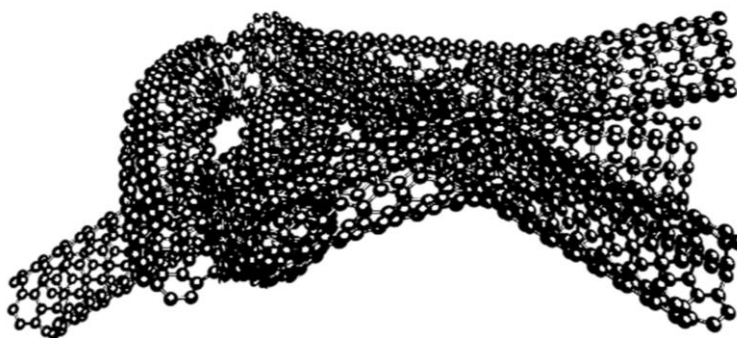


Figure 2.4 Schematic of carbon nanotubes [61].

Graphene and Derivatives

Graphene, two-dimensional (2D) carbonaceous nanomaterial, also attracts attention owing to its distinctive tensile properties (Young's modulus: ~ 1 TPa; tensile strength: ~ 130 GPa) [62], thermal conductivity (~ 5000 $\text{Wm}^{-1}\text{K}^{-1}$) [63], electrical conductivity ($\sim 10^8$ S/m) [64] and specific surface area (SSA, 2630 m^2/g) [65]. Graphene indeed is a monolayer of sp^2 hybridized carbon atoms packed in a 2D honeycomb lattice [66], Figure 2.5. Generally, graphene is synthesized via CVD or physical exfoliation methods, restricted to small batch production due to the difficulty in preparation [67]. Therefore, graphene-derived materials, such as multilayer graphene, graphene

nanoplatelets (GNPs) and graphene oxide (GO), are much broadly investigated and applied owing to their availability. Additionally, the oxidized functional groups of GO facilitate the even dispersion of itself in the polymer matrix, while at the cost of the intrinsic electrical conductivity of graphene as the extensive content of sp^3 carbon-carbon bonds along with the present of defect. The electrical conductivity of GO can be retrieved to some extent via restoring the sp^2 bonds [67]. It is a cost-effective method to synthesize graphene sheets, commonly reduced graphene oxide (rGO), via reducing GO chemically or physically. As competitive nanofiller candidates, the incorporation of graphene and its derivatives substantially improves properties of FRPs and endows FRPs with multifunctionalities (to be detailed in the sequent section).

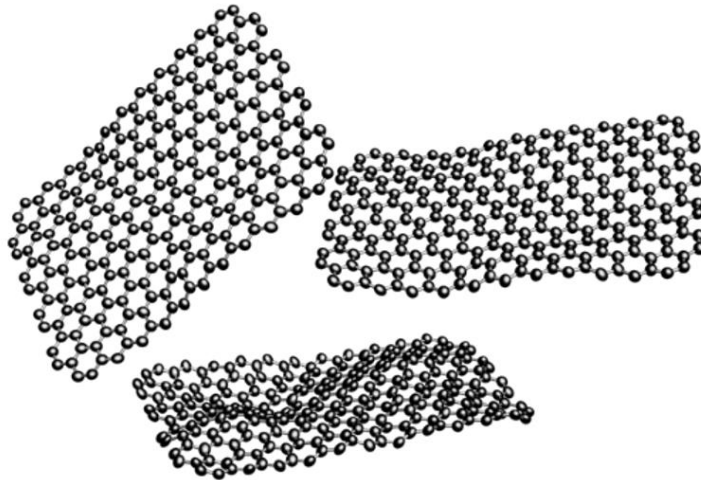


Figure 2.5 Schematic of graphene [61].

2.4.2 Fabrication and Performance

There exist various methods to develop nanocomposite-based sensors, each of which owns advantages and disadvantages. To make the content of this section more compact, representative and enlightening, current achievements and restrictions in this domain will be reviewed according to preparation methods.

(a) Matrix Modification

Blending carbonaceous nanoparticles with polymer improves mechanical properties of thus-fabricated nanocomposites whilst simultaneously increases their thermal and electrical conductivities. Hernández-Pérez *et al.* [68] demonstrated remarkable increase in the impact strength (by 84%) of epoxy resin with the incorporation of 1.0 wt.% MWCNTs. Owing to their low-density and 1D features, CNTs are an ideal reinforcement to construct percolated conductive networks within matrix with a low percolation threshold (generally <0.1 wt.%) [69]. Thus-created conductive paths transferred insulating polymers to be semiconductive or conductive via increasing the electrical conductivity by up to nine orders of magnitude [69]. The intrinsic piezoresistivity of created conductive networks enable the nanocomposites to self-sense the strain and reflect their health information. In a pilot study, Thostenson and Chou [70] created sensing networks via dispersing MWCNTs in epoxy resin using a calendaring approach. Specifically, a three-roll mill was adopted to apply high shear forces on the MWCNT-resin mixture to untangle and enhance the dispersion of

nanotubes, with a gradually decreasing gap setting down to 5 microns. The authors utilized percolated CNT networks to evaluate the nature, onset and development of damage. As the CNTs were dispersed in the matrix, such sensing networks were significantly sensitive to matrix-dominated failure modes by nature. Similarly, Boger *et al.* [71] modified epoxy resin with either carbon blacks (CBs) or CNTs, to produce hybrid composites with load-sensing and health monitoring capabilities. In a dynamic tensile test, it was observed that the gradually increased electrical resistance (ER) measured by sensors was accompanied with a decrease in the stiffness of specimens, which indicated the occurrence of degradation. Different from most published studies which employed a single type of carbonaceous nanomaterial to decorate polymer, Li *et al.* [72] co-introduced CNTs and GNPs to develop multifunctional epoxy nanocomposites. Vertically-aligned CNTs directly grew on GNPs via CVD and then the hybrid nanofillers were dispersed in epoxy resin using a three-roll mill. The tensile results showed that the CNTs and GNPs synergistically increased the modulus by 40% and ultimate tensile strength (UTS) by 36% with respect to the pristine epoxy, much higher than that of the single nanofiller-decorated nanocomposites. The enhancements were attributed to that the CNT-GNP hybrids gave rise to optimized dispersion of nanoparticles along with better interfacial properties between matrix and reinforcements, leading to a remarkably increased load transfer efficiency. To further exploit such novel nanocomposites as *in situ* sensors, their ER responses were measured under both quasi-static and cyclic loads.

For most nanocomposites, which are blended with a single type of carbonaceous nanomaterial, their ER increases proportionally with the applied strain and finally reaches infinity when failure completes. Nonetheless, the authors in this work found that the ER of nanocomposites first increased with the applied strain, followed by a decrease when the strain exceeded ε_c (a critical strain defined). Such a phenomenon was on account of the reason that with the formation of micro-voids and shear bands, the rotation of the hybrid nanofillers rearranged the nanostructure and made the separated nanoparticles come into contact again.

Though achievements have been made in carbonaceous nanoparticle/polymer nanocomposites and fibre-reinforced, nanofiller-decorated polymer composites, there still exist some demerits limiting the development and application of nanocomposite-based sensors which are directly created via blending polymers with carbonaceous nanomaterials. For example, due to their high affinity among adjacent CNTs and low affinity with polymers, CNTs tend to agglomerate and thus lead to uneven dispersion in matrix, which significantly limits their enhancing effect. Such a phenomenon is partially solved via dispersing CNTs into polymers with the assistance of sonication, extrusion and shear mixing techniques. Besides physical approaches to enhance the dispersion of carbonaceous nanomaterials, chemical grafting is also introduced to facilitate the dispersion of nanoparticles in polymers, such as the formation of hydrogen bondings, coordination bonds or $\pi-\pi$ interaction. Nonetheless, the

incorporation of nanoparticles remarkably increases the viscosity of resin, which leads to the difficulty in wetting and commonly causes residual voids in structures.

Besides being blended into matrix, carbonaceous nanoparticles can also be directly deposited on fibre surfaces via various techniques, to work as sensing elements and may simultaneously enhance the ILSS and/or interfacial shear strength (IFSS) of thus-fabricated composites.

(b) Dip Coating

As the simplest way to deposit carbonaceous nanomaterials on fibre surfaces, dip coating involves preparation of a solution, in which carbonaceous nanoparticles are dissolved in either DI water or a solvent, and immersion of fibres in the prepared solution. Yang *et al.* [73, 74] deposited MWCNTs onto glass fibre (GF) yarns via dip coating, to form multifunctional interface sensors which can simultaneously enhance the IFSS and monitor the accumulated interfacial damage. The density of MWCNTs deposited on GF yarns was regulated via adjusting the concentration of MWCNT solutions, duration of ultrasonic dispersion and number of immersion cycles. When integrated in a thermoplastic composite, such sensors can first monitor the interphase behaviors of composites under mechanical loadings. After identification of damage, the sensors self-healed the damaged region via generated Joule heat based on the mechanism that the thermoplastic would melt with applied heat and then heal the

damaged cracks or delamination. The results showed that with the regulated amount of MWCNTs on GF yarns, the IFSS was increased by 48.9%. The authors endowed a single type of sensor with three functionalities, namely mechanical reinforcing, monitoring and self-healing, which can be referred as an inspiration for the future development of functional composites. In a modified manner, Luo *et al.* [75] deposited CNTs and rGOs on GF tows in a continuous and automotive way, as shown in Figure 2.6.

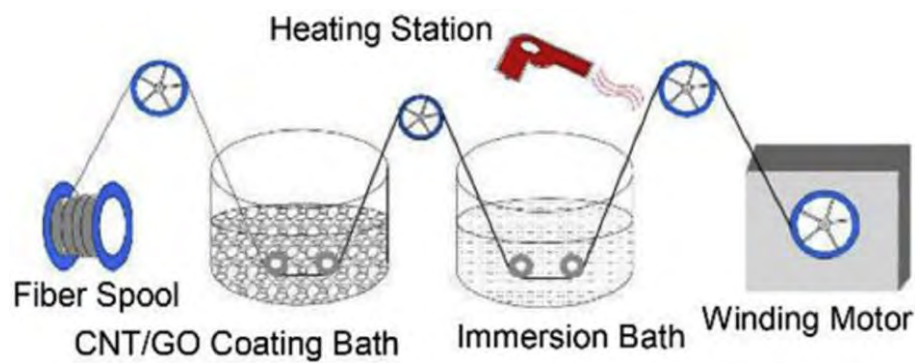


Figure 2.6 Schematic of a roll-to-roll fibre winding and dip coating process for continuously depositing carbonaceous nanomaterials on fibres [75].

Thus-decorated GF tows were braided into the as-received GF fabric and then acted as 1D line sensors within composites, to monitor the resin flow front and cure progress of epoxy resin in a VARTM process. The authors also revealed that the sensing performance and sensitivity of fibre sensors depend on their underlying nanostructures. To specify, for CNT-decorated fibre sensors, it is by nature easy for

resin to penetrate into conductive networks owing to the loose-packed nanostructure and thus results in high sensitivity. As for rGO-decorated fibre sensors, the 2D rGOs stacked relatively tightly and only limited resin can migrate into networks through gaps formed by adjacent rGOs, with resulting poor performance of sensors. Above revealed sensing mechanism offers a strategy to tailor the sensitivity of nanocomposite sensors when performing CM. Additionally, a dry spot and a partially infused spot, respectively simulated using one circular and one semicircular polyimide films, were identified, reflected by variations in ramping rates of ER measured by the line sensors. Though the authors demonstrated that a sensing grid can be created via braiding multiple sensors into the fabric, the limitation of line sensors that they could only reflect information in their adjacent areas still exists. Outperforming line sensors, Dai and Thostenson [76] created a thin, porous area sensor via dip coating CNTs onto a nonwoven textile and performed electrical impedance tomography (EIT) to map the resin flow in a infusion process. Without internally configurated wires and electrodes, such an EIT method can monitor a large area of host composites via simple boundary measurement. Such an EIT method successfully mapped the shape and location of the resin flow front and showed the dry and unsaturated spots. The authors also pointed out the potential of such area sensors in implementing in-service SHM.

Though convenient, the dip coating method generally provides a random distribution of carbonaceous nanomaterials on fibre surfaces and thus may be inefficient to improve properties which are originally targeted [77].

(c) Spray Coating

Spray coating, a convenient yet versatile approach, has the greatest potential for industrial scale-up [78, 79]. A mass of studies proved that spray coating is an efficient technique to improve both electrical and interlaminar properties of composites, along with endowed *in situ* damage sensing capability [14, 78-81]. Zhang *et al.* [78] directly sprayed CNTs onto CF prepregs, with a good control in localization and formation of CNT networks. Excellent *in situ* sensing performance was observed with a good correlation between the ER variation measured by CNT networks and crack propagation. Additionally, out-of-plane mechanical properties of CFRPs, say Mode-I fracture toughness, was remarkably increased by 50% with an extremely low loading (0.047 wt.%) of CNTs. Without sacrificing the original integrity of host composites, Nag-Chowdhury *et al.* [14] homogeneously introduced nanocomposite sensors in glass fibre-reinforced polymer (GFRP) composites via spraying CNTs on GF fabrics prior to the infusion of epoxy resin. Unlike other studies which dissolved conductive carbonaceous nanoparticles and/or dielectric polymer matrices in organic solvents, this study dispersed CNTs into epoxy resin and then sprayed thus-mixed epoxy resin layer by layer to formulate ultrathin sensors on

a layer of GF fabric. As a characteristic highlight, the sensors were electrified via CF yarn-made threads to minimize the intrusion due to the communication system. Such electrically active layer, accompanying with other nine plies of as-received fabrics, was then laid up and infused with epoxy resin via VARTM to prepare samples for the load sensing purpose. The fabrication scheme of such nonintrusive and self-sensing composites is shown in Figure 2.7. It was well established in that study that the embedded sensors can detect the initiation, closing, reopening and propagation of cracks in cyclic tensile tests. Featuring ultrathin thickness (1.5 μm) and controllable planar dimension (1~100 mm^2), such sensors can be densely deployed inside GFRPs at desired locations to monitor damage accumulation and anticipate fracture of composite structures. Luo *et al.* [82, 83] decorated GFs with carbonaceous nanomaterials to calibrate the impedance of fibre sensors, on which basis the polymer cure progress was evaluated. Cure monitoring was followed with the failure prediction using the same decorated GFs when the composites were loaded.

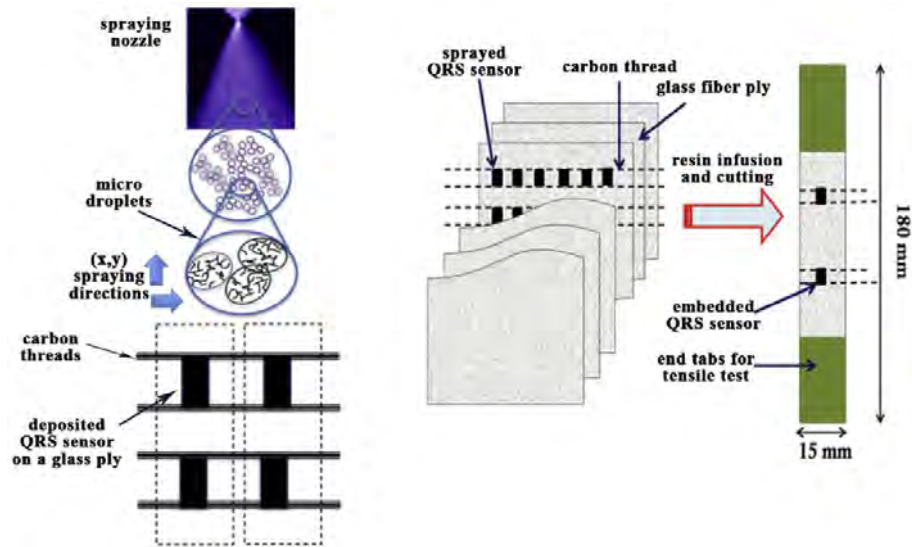


Figure 2.7 Fabrication scheme of nonintrusive and self-sensing composites [14].

(d) Electrophoretic Deposition

Electrophoretic deposition (EPD) is a robust and two-step technique, in which charged particles in a suspension move towards and then deposit on an opposite charged electrode, driven by an applied electric field, schematically shown in Figure 2.8. EPD owns merits such as the relatively short processing duration, low-cost equipment and adjustable thickness of deposited matters [84-86]. Interest in EPD continuously increases recently, particularly in the field of carbonaceous nanomaterials, with which advanced nanostructured coatings can be formed at interphases of fibres and matrix to enhance properties of composites.

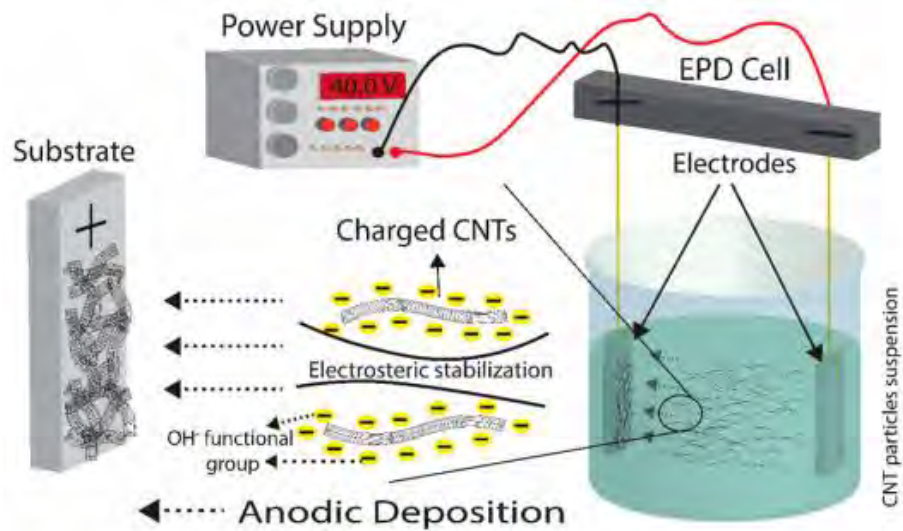


Figure 2.8 Schematic of an EPD process [87].

Zhang *et al.* [86] deposited CNTs on GF surfaces via both EPD and dip coating approaches and thoroughly investigated and compared properties of thus-produced hierarchical structures. It was shown that the EPD approach delivered a more even and continuous CNT distribution, compared with the dip coating method. Mimicking a biological bone structure, interphases decorated with heterogenous CNTs, between fibres and matrix, improved the IFSS of composites according to results obtained from the fragmentation test. The ER variation of the developed semiconductive MWCNT–GFs in a tensile test can be divided into three stages, namely (i) linear, (ii) non-linear and (iii) abrupt change, which respectively corresponded to the elastic deformation, plastic deformation and fracture phase of interphases. Nonetheless, the authors also pointed out the issue that large scatters among measured individual ER data were noted due to the nonuniform deposition of MWCNTs which undermined

the monitoring performance of the hybrid GFs. Sung *et al.* [85] also deposited the uniform functionalized CNT coating on GF fabrics and demonstrated the robustness of EPD compared with dip coating, due to the formation of chemical bondings in the EPD process. The EPD technique was also applied to successfully deposit carbonaceous nanomaterials on CFs [88-90]. In a brief, a successful EPD process prerequisites a stable dispersion of nanofillers in appropriate solvents and sonication is commonly maintained during an EPD process to avoid the settling of nanoparticles, reduce the bubbling and promote the penetration of nanoparticles into fibre bundles. Besides, for the deposition of nanoparticles on dielectric fibres, intimate contact between the electrode and fibres is necessary as the deposited coating initially grows on the cathode, followed by advanced growth on fibres as the formed conductive coating acts as the extension of the electrode and promotes the deposition. However, though the proven effectiveness of EPD compared with dip or spray coating methods, its application in large-scale structures is still limited owing to its cumber.

(e) Chemical Vapor Deposition

CVD is one of the most popular techniques to synthesize CNTs or graphene [91, 92]. In such a process, hydrocarbon precursors thermally decompose to carbon radicals at metallic catalysts, which not only work as catalysts to lower the energy barrier of reaction but also determine the morphology of thus-synthesized CNTs or graphene. Irrespective of the increased popularity, multiple factors, such as the selection of the

hydrocarbon source, choices of the catalyst precursor and growth temperature, can influence the efficiency of such an approach. All these factors deserve thorough investigation and discussion. CVD also permits the growth of CNTs or graphene in a variety of forms via regulating growth parameters. More importantly, such a technique allows the use of diverse substrates. Therefore, the direct growth of CNTs or graphene on fibres becomes a promising technique to produce multifunctional composites. A representative CVD set-up is schematically shown in Figure 2.9.

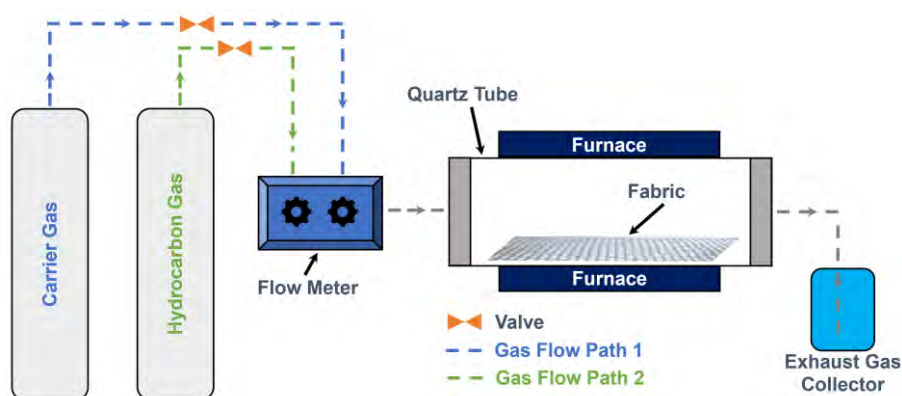


Figure 2.9 Schematic of a CVD set-up.

The growth of CNTs or graphene via CVD on conductive fibres commonly targets to enhance interfacial and/or interlaminar strengths and increase thermal and electrical conductivities of composites. Yao *et al.* [93] reported an enhancement, by 15%, in the ILSS via growing functionalized CNTs on CFs. Sha *et al.* [94] also demonstrated that grafting vertical graphene on CFs via plasma-enhanced CVD can improve the IFSS by ~118.7%. Pozegic *et al.* [95] showed that fuzzy CNT networks created on

CFs endowed hybrid CFRPs with superior electrical conductivities; the electrical conductivities remarkably increased at both in-plane (330%) and out-of-plane (500%) directions. Different from conductive fibres, decorating dielectric fibres with carbonaceous nanomaterials via CVD usually aims at creating self-sensing FRPs. Ebastian *et al.* [96] showed that fuzzy CNT-decorated GF sensors exhibited the similar gauge factor (1.6–2.3) to the standard strain gauge (~2.0) and responded to stimuli at longitudinal, transverse and off-axis directions. Tailoring mass fractions of CNTs via modulating CVD parameters, He *et al.* [97] showed that the CNT shell synchronously improved electrical, thermo-mechanical and flexural properties of the hybrid GFRPs to varying degrees. Moreover, the damage-related ER variation could be introduced to implement *in situ* SHM of composites.

Nonetheless, unlike the above other fibre decoration techniques which can be carried out at the ambient temperature, CVD has to be performed under the relatively harsh condition for the synthesis of CNTs or graphene on fibres. Luca *et al.* [98] showed that a CVD process with 760 °C CNT growth temperature decreased the tensile strength of GFs from ~4.15 to ~1.99 GPa. To reduce adverse effects of CVD on core properties of fibres, Sha *et al.* [94] grafted vertical graphene on CFs at 400 °C via plasma-enhanced CVD and did not sacrifice the tensile strength and modulus of fibres.

(f) Interleaving

Interleaving is another broadly adopted approach which incorporates independent nanocomposite-based mediums among dry fabrics or prepregs at the lay-up procedure. Buckypaper, consisting of entangled CNT networks, is one of the most popular sheets applied to work as sensing elements in composites [2, 99, 100]. Lu *et al.* [2] produced Buckypaper via a spray-vacuum filtration approach and then embedded it between GF prepregs to perform process monitoring in a real-time manner. The ER of Buckypaper responded to resin phase changes accordingly in dynamic cure processes and simultaneously indicated the lowest viscosity point and the gel point of resin, which demonstrated such Buckypaper-based sensors owned the potential to optimize the manufacturing process and improve the quality of thus-cured composites. Aly *et al.* [100] used Buckypaper-based sensors to monitor flexural loading-induced strains at the application phase of composites, the ER variation acquired in monotonic and dynamic flexural tests showed that the Buckypaper-based sensors appeared to reflect mechanical states of and the damage development in host composites.

Interleaves, in other diverse forms, also drew attention in past decades. For instance, Ou *et al.* [101] deposited continuous CNT veils on CF fabrics and then double cantilever beams (DCBs), with or without interleaves, were prepared to investigate the toughening effect of CNT veils. The fractographic analysis showed that the

interlaminar crossing played a major role in toughening. Though the authors did not mention the sensing capability of such CNT veils, however, it is intuitionistic that propagated cracks would alter the nanostructure of the veils and thus result in the ER variation, which can be introduced to monitor the crack propagation via appropriate data interpretations.

2.4.3 Summary

With minimized intrusion, nanocomposites have offered the new possibility to revamp the monitoring philosophy of FRPs through a life cycle. However, the working principle of sensors in this category is mainly based on the premise that the change in the resin state or the presence of damage can incur the variation in the ER measured by the nanocomposite-based sensors, which is a global parameter, only qualitatively and holistically reflecting the alteration in material properties between a pair of electrodes.

In contrast to the electrical impedance, GUWs carry rich localized information accumulated along propagation paths, enable quantitative estimation of the cure progress and structural integrity. However, GUWs far exceed the responsive frequency regime of most nanocomposite-based sensors, which are targeted to capture variations in the ER induced by quasi-static or low-frequency strains.

2.5 Functionalized Composites with Expanded Capacities

In addition to implement self-cure monitoring and self-integrity monitoring, at manufacturing and application phases respectively, the appropriate incorporation of carbonaceous nanomaterials endows conventional FRPs with other functionalities, which broadens applications of the composite materials. On top of that, the recent prosperity in additive manufacturing and automated manufacturing also gives new vitality to composite materials. Representative non-structural functions include:

- i) self-sensing (perception of strains, damage, temperature, *etc.*);
- ii) self-healing (automatic repair after the occurrence of damage, provided by thermoplastic polymers or encapsulated healing agents);
- iii) energy storage (structural batteries and capacitors, with the use of conductive CFs as electrodes and modifications of other structural components);
- iv) electromagnetic interference shielding (to protect electronics and shield radio waves, relying on absorption and/or reflection of electromagnetic radiation).

Among the aforementioned multifunctionalities, sensing is a particularly interested non-structural function in this study, to implement both CM and SHM. As capabilities of functional composites in both CM and SHM domains have been adequately reviewed above, only the residual listed functionalities will be reviewed in this section.

(a) Self-healing

Self-healing is a function with which a composite structure heals itself automatically when damage occurs. Such a function is extremely valuable for structures serving in outer space which cannot be repaired with human intervention. Besides the ability to sense the appearance of damage, the self-healing function also requests the capacity to self-heal. There are three representative materials applied to implement self-healing, namely encapsulated healing agents [102, 103], remendable polymers [104] and thermoplastic polymers [105].

(b) Energy Storage

Energy storage can be achieved via either battery (in the form of chemical energy) or capacitor (in the form of electrical energy) [106, 107]. Particularly, structural battery composites gain burgeoning development in the past decade, to provide mass-less energy storage for electrically powered devices (*e.g.*, electromobile). There are two differentiated approaches to develop structural battery composites. The first category directly integrates batteries, which are in the form of thin films, into composites (essentially sandwiched structures) [108, 109]. The second category endows every constituent with multiple functions [110, 111]. For instance, carbon fibres act as both reinforcements and electrodes in structural battery composites while the polymer functions as matrix and electrolyte.

(c) Electromagnetic Interference Shielding

Conventional CFRPs are effective in electromagnetic interference (EMI) shielding, over the broad frequency regime ranging from 0.3 MHz to 1.5 GHz. With incorporation of carbonaceous nanoparticles, the shielding effectiveness of composites can be improved because of the larger surface area of carbonaceous particles, the induced skin effect and the introduced multiple reflections [112].

2.6 Summary

To summarize, the recent advances and current dilemmas in cure monitoring, structural health monitoring and composites with the integrated sensing system have been reviewed in this chapter, to guide the development of integrated functionalized composite structures with the self-sensing capability.

Integratable nanocomposites, featuring the high sensitivity and compatibility, are now being considered as one of the most promising sensors for CM and SHM of host structures, substituting conventional intrusive, rigid and heavy sensors. Nevertheless, most current proposed nanocomposite-based sensors failed to response to dynamic strains of high frequency and low magnitude, let alone GUWs which are one of the most vital tools applied in CM and SHM. Therefore, it is of vital importance to

develop integratable and GUV-sensitive nanocomposite sensors which feature following characteristics:

i) **able to precisely perceive broadband dynamic strains:**

most reported nanocomposite-based sensors were engineered to perceive the ER or low-frequency cyclic strains, lacked the capability of responding to dynamic strains of high frequency, let alone the acquisition of GUVs of several hundred kilohertz or even megahertz; sensors with a broad responsive frequency regime are desired as they can be adopted in various sensing scenarios;

ii) **minimize the mechanical degradation of host composites:**

as commented earlier, conventional GUV-based monitoring approaches are regularly implemented in conjunction with the use of PZT-type sensors for GUV acquisition, embedment of which unavoidably degrades the original structural integrity of host composites; on top of that, associated wires and electrodes should also be of minimized intrusion, which is rarely considered in proposed nanocomposite sensing systems;

iii) **scalable and lightweight:**

the nanocomposite-based sensors should be produced in a cost-effective and convenient manner. Additionally, the sensors should be lightweight and flexible, which allows them to be densely deployed in engineering structures, even with a curved shape, to extract rich information of the monitored components, while not at the cost of bringing the weight penalty;

iv) **powerful continuous monitoring capability:**

the sensors should enable the use of a single type of sensor for uninterrupted monitoring across multiple stages of composites. In detail, the sensors are desired to be able to characterize the infusion, gel point, cure degree and cure anomaly of resin during manufacturing, followed with the employment in both passive and active acousto-ultrasonics-based SHM at the in-service state of the host composites.

CHAPTER 3

Carbon Nanotube-grafted Sensing Fabrics: Development, Characterization and Applications

3.1 Introduction

In this chapter, a genre of sensing fabrics, developed from direct grafting carbon nanotubes (CNTs) on glass fibre (GF) fabrics, is initially developed to fulfill structural integrity monitoring (SIM) of hybrid glass fibre-reinforced polymer (GFRP) composites. CNTs are *in situ* grafted on fabrics via chemical vapor deposition (CVD) at 500 °C. Scanning electron microscopy (SEM), transmission electron microscopy (TEM), thermo gravimetric analysis (TGA) and Raman spectroscopy are respectively conducted to characterize the morphology, loading and quality of synthesized CNTs. GF fabrics are grafted with different mass fractions of CNTs, to develop sensing fabrics deployed with CNT-grafted GF (CNT-g-GF) sensors, which can be adopted to implement guided ultrasonic wave (GUW)-based

integrity monitoring. Tensile tests at two scales, namely single fibre tensile test (ASTM C1557) and fibre-reinforced polymer matrix composite tensile test (ASTM D3039), are performed to examine the effects of the proposed CVD technique on tensile properties of fibres. The responsivity of sensing fabrics, with different loadings of CNTs, towards GUWs is evaluated on an ultrasonic measurement platform, to acquire appropriate sensitivity to ultrasonics. Additionally, such CNT-g-GF sensors are introduced to execute continuous, spontaneous monitoring of self-conditions of GFRPs, from cure through service, by measuring the change in electrical resistance (ER) of CNT-formed piezoresistive networks.

3.2 Grafting of Carbon Nanotubes on Fabrics

Plain weave E-glass GF fabrics (High Gain[®] 175 gsm) are applied as the reinforcement while the selected matrix consists of epoxy resin (WEST SYSTEM[®] 105) and hardener (WEST SYSTEM[®] 209). The mass ratio of epoxy resin and hardener is 3.68 to 1, as recommended by the manufacturer. Analytical grade ethanol (Honeywell[®] 24194) is adopted as both the hydrocarbon precursor for the growth of CNTs and the solvent for the catalyst precursor (cobalt (II) nitrate hexahydrate supplied by International Laboratory[®]), and the 5 vol% H₂/N₂ gas mixture (LINDE[®]) is simultaneously used as the reducing and carrier gas for the proposed CVD process.

The cobalt (II) nitrate hexahydrate is dissolved in the ethanol to formulate a sprayable catalyst precursor suspension with a concentration of 5.0 wt.%, followed by being sonicated in an ultrasonic bath (Brandson[®] 5800 Ultrasonic Cleaner, 40 kHz) for two hours to facilitate the dissolution of solute. The aqueous suspension is then sprayed on as-received fabrics using an airbrush (HD-130), which are pre-covered with a polyimide molding film with elaborately designed hollowed-outs, to initiate the growth of CNTs in the sequent CVD process. The coated fabrics are then dried in an oven at 60 °C for 15 min.

CNTs grow on the cobalt nitrate hexahydrate-coated GF fabrics through a CVD process, schematically shown in Figure 3.1. In such a process, GF fabrics are inserted into a quartz tube attached to a furnace, in which an inert environment is maintained by purging the H₂/N₂ gas mixture at 100 sccm for 2 h, prior to heating. The tube is heated at a rate of 10 °C/min and then kept at 450 °C for 30 min, to warrant full reduction of the catalyst precursor in the hydrogen-maintained atmosphere. The temperature continues to rise to 500 °C, to initiate the growth of CNTs. The ethanol vapor at 85 °C is introduced into the tube via shifting the flow path of the gas mixture from Path 1 to Path 2, in Figure 3.1, to supply carbon source for the synthesis of CNTs. The growth of CNTs lasts for 30 min while the H₂/N₂ gas mixture is continuously fed into the tube at a flow rate of 50 sccm during the entire CVD

process, to promote the growth. The furnace is then cooled down to the room temperature with a rate of 10 °C/min.

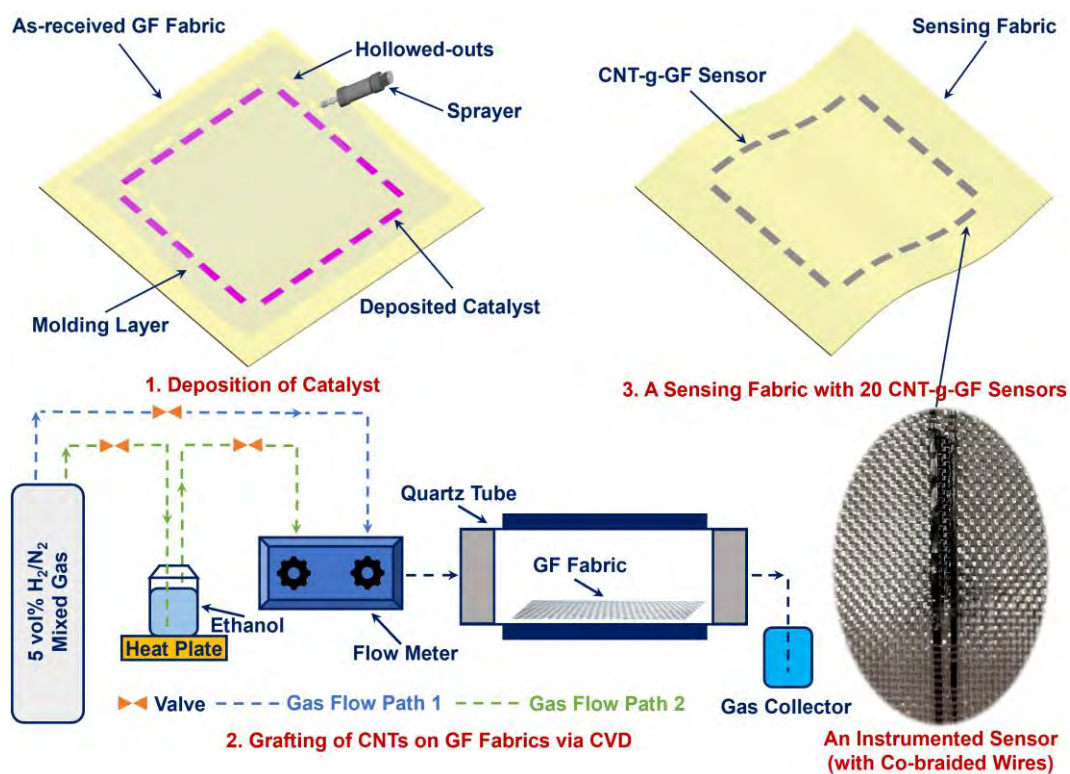


Figure 3.1 Preparation flowchart of GUV-responsive sensing fabrics.

3.3 Characteristics of Synthesized Carbon Nanotubes

Through regulating the amounts of the deposited catalyst precursor, which is achieved via spraying different volumes of the catalyst precursor suspension on fabrics in this study, GF fabrics are grafted with CNTs of six representative loadings. As can be visually inspected in Figure 3.2(a), the colour of CNT-g-GFs gradually

gets darker with the increasing loading of CNTs. The morphology of CNT-g-GFs is investigated on a SEM platform (TESCAN[®] MAIA3). Taking the total mass of CNT-g-GFs as the reference, the mass fractions of grown CNTs are quantified via a thermal gravimetric analyzer (Mettler Toledo[®] TGA/DSC 3+). For each circumstance, the chopped CNT-g-GF powder is heated from 25 to 800 °C at a rate of 10 °C/min in an air-purging (50 sccm) atmosphere. The TGA curves demonstrate that the representative mass fractions of CNTs are 0.38 wt.%, 0.45 wt.%, 0.64 wt.%, 0.81 wt.%, 0.85 wt.% and 1.07 wt.%, in Figure 3.2(b). It can be acquired in Figure 3.2(b) that the decomposition of CNTs initiates at ~420 °C and completes at ~580 °C. The morphology of CNT-g-GFs with various mass fractions are shown in Figure 3.3, which will be detailed along with their responsivities to GUWs in Section 3.4.

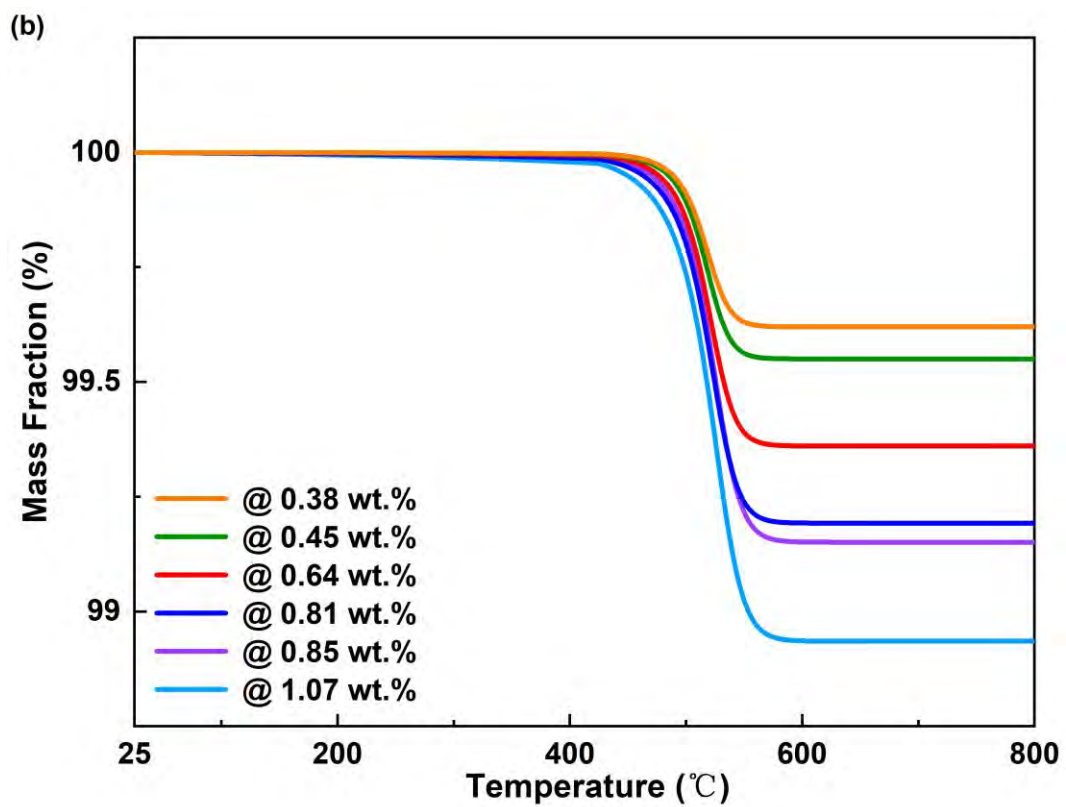
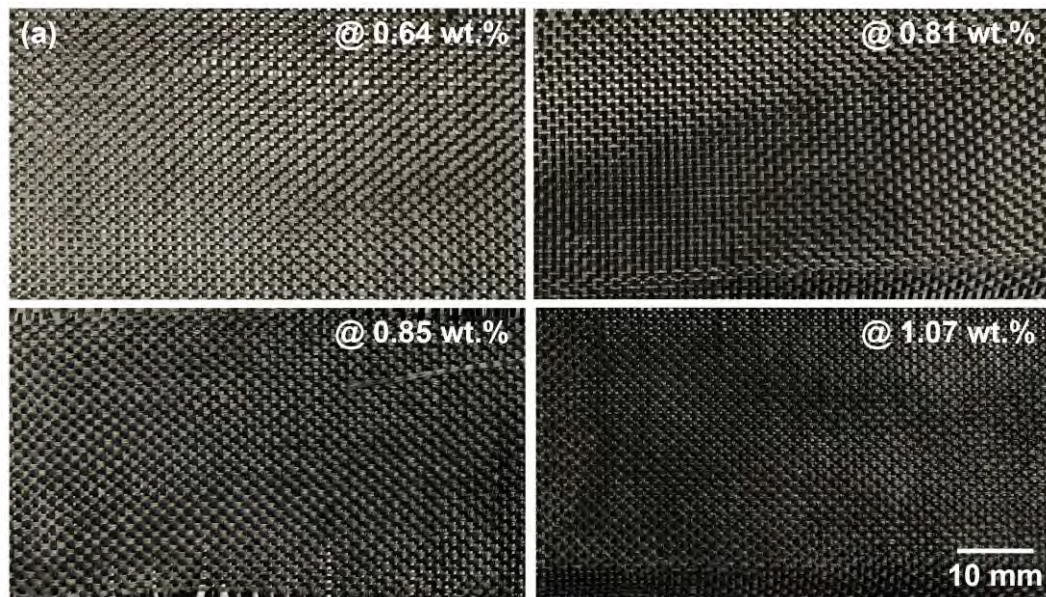


Figure 3.2 (a) Photograph of; and (b) TGA curves of CNT-g-GFs, with various mass fractions of CNTs.

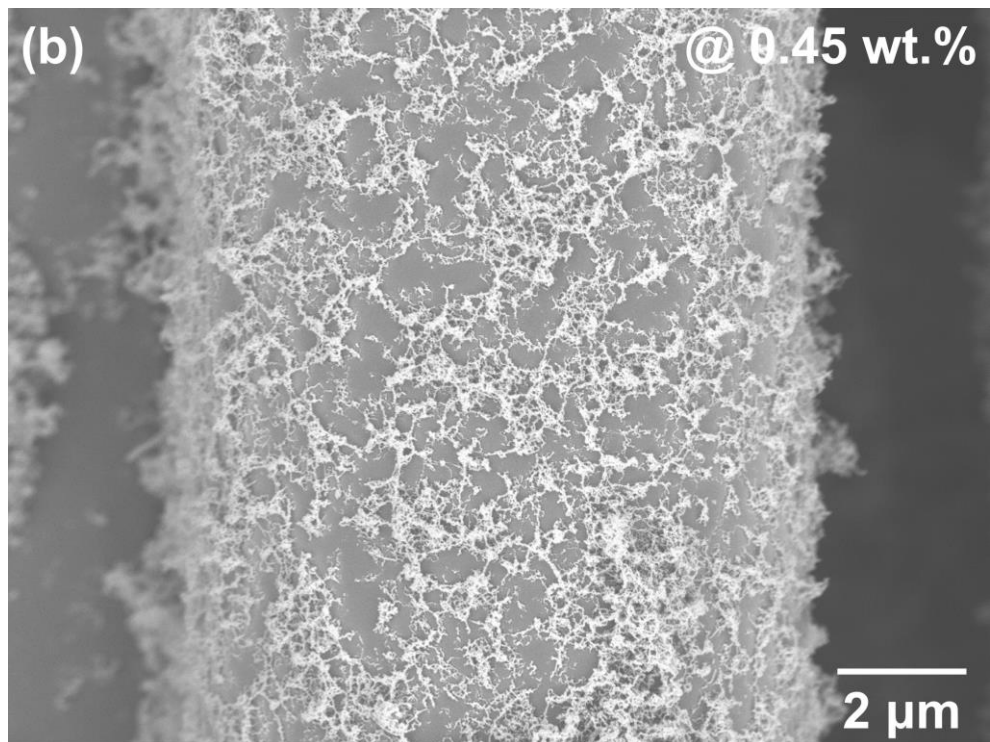
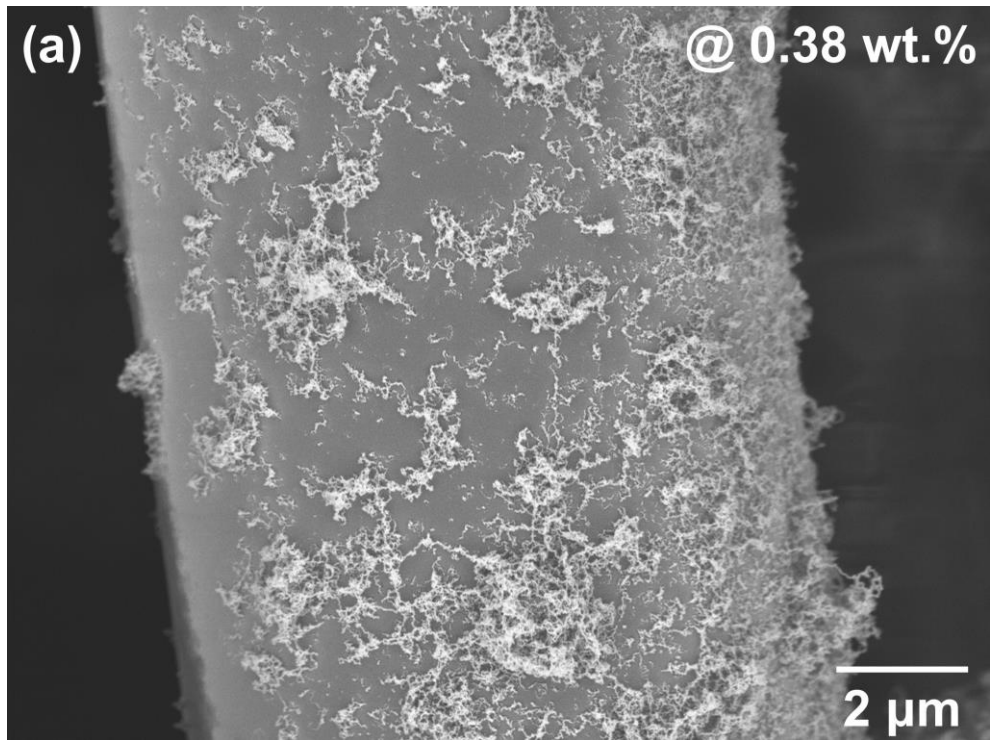


Figure 3.3 SEM images showing the morphology of CNT-g-GFs with different CNT loadings.

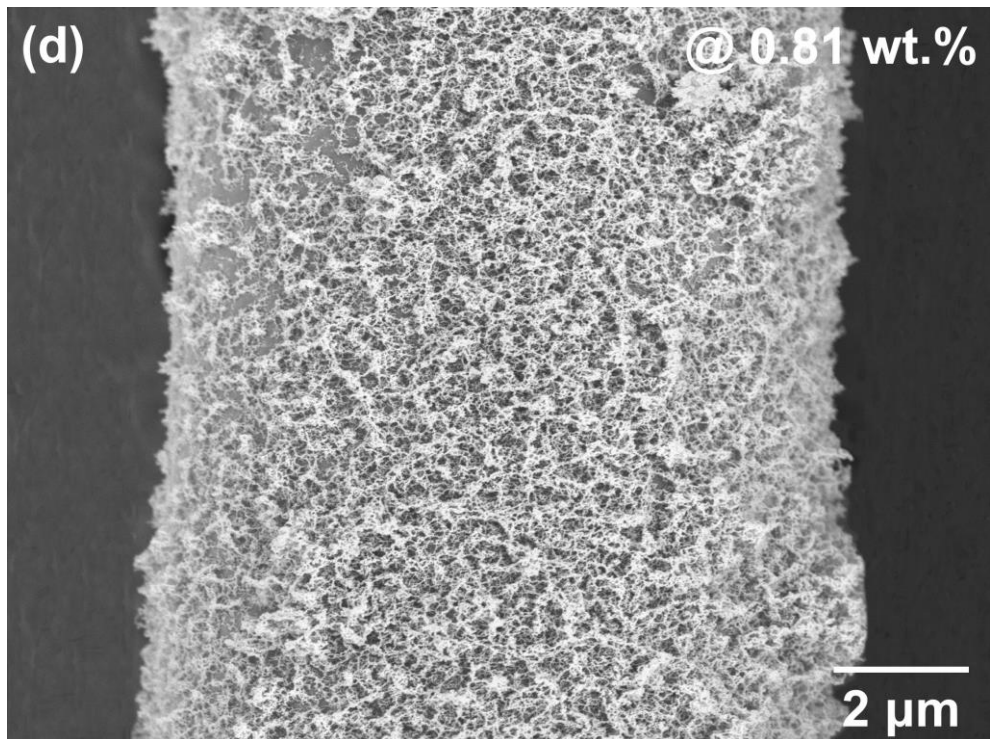
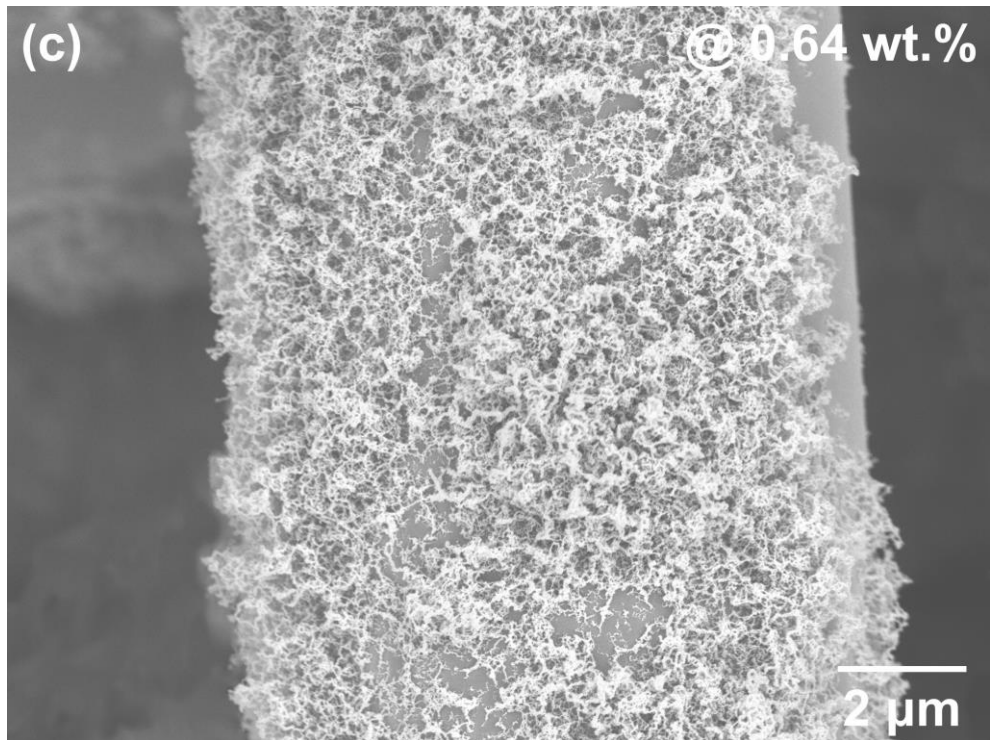


Figure 3.3 *Cont.*

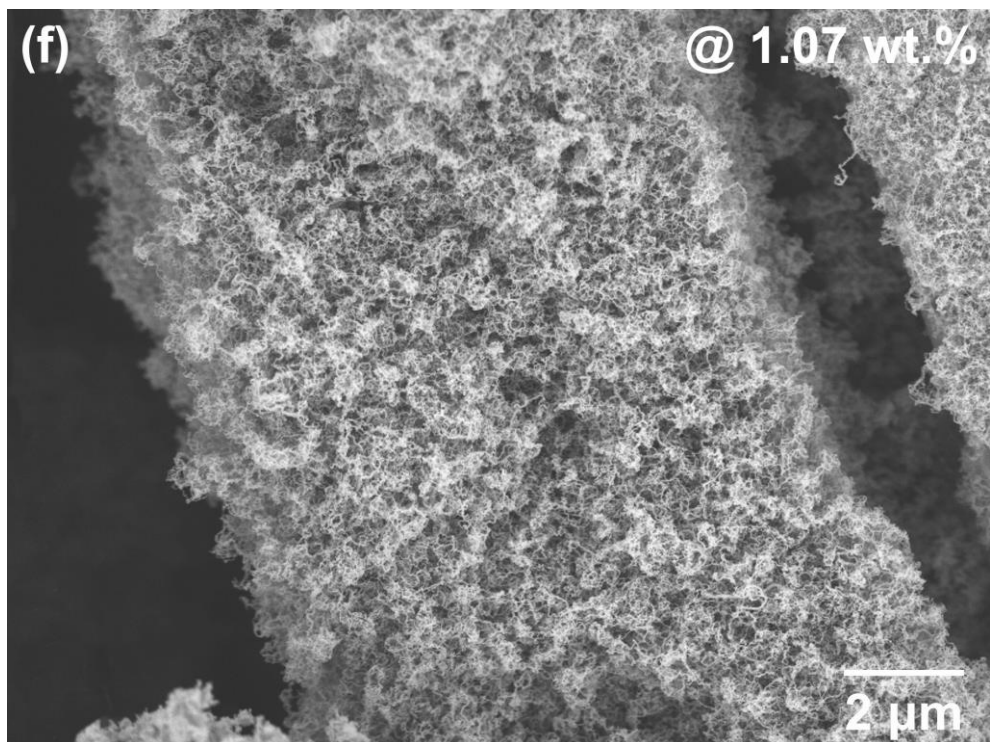
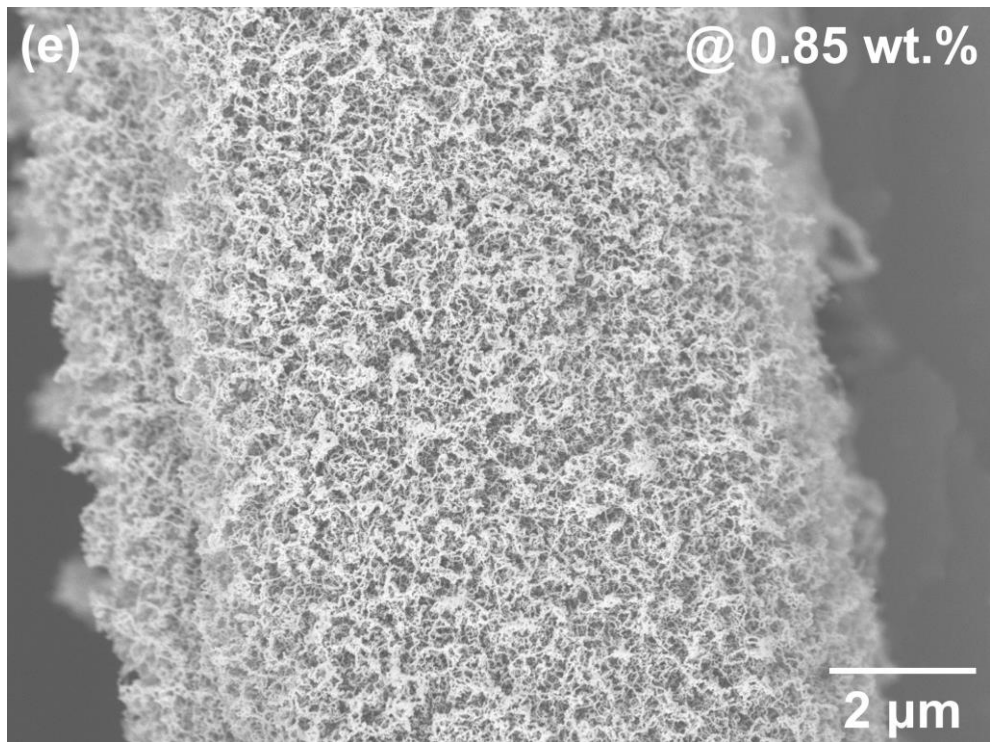


Figure 3.3 *Cont.*

The Raman spectra of synthesized CNTs are acquired with a Raman spectrometer (Witec[®] alpha300R) using a 532 nm laser as the excitation, to evaluate their quality. Figure 3.4 provides the Raman spectra of CNT-g-GFs with mass fractions of 0.64 wt.%, 0.81 wt.%, 0.85 wt.% and 1.07 wt.%. The peak, positioned at circa 1340 cm⁻¹, is known as the D-band corresponding to the disorder structure while the G-band locating at circa 1580 cm⁻¹ represents the *sp*² carbon-formed graphitic structure. To quantify the quality of synthesized CNTs, the I_d/I_g ratio, a good indicator revealing the quality of CNTs, is calculated. For investigated four categories, their I_d/I_g ratios are all less than 0.89, indicating a high degree of graphitization.

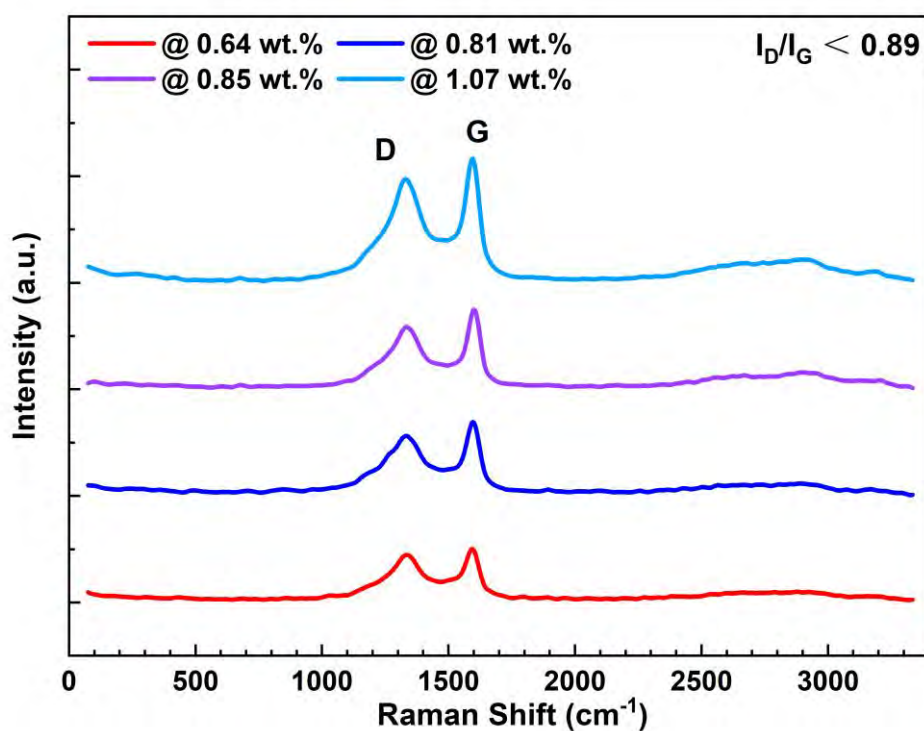


Figure 3.4 Raman spectra of CNT-g-GFs.

The tubular structure of synthesized CNTs is revealed on a TEM platform (JEOL® JEM-2011), in Figure 3.5, showing the co-axial, thin-walled tubular structure of CNTs. It can be measured in Figure 3.5 that the inner and outer diameters of the CNT are ~20 nm and ~42 nm, respectively.

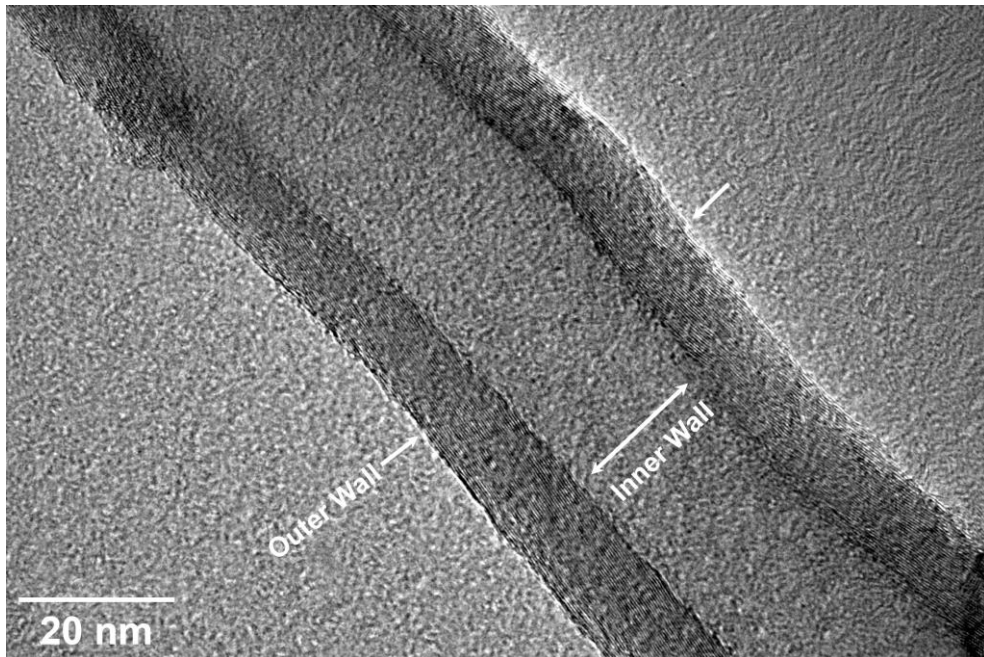


Figure 3.5 TEM image of a synthesized CNT.

3.4 Response to Guided Ultrasonic Waves

With the method described in Section 3.2, CNTs are initiated to grow at 20 targeted regions of a GF fabric, each of which will be configured as a sensor with a planar dimension of $30 \times 2 \text{ mm}^2$, to make a sensing fabric. 20 thus-developed sensors configure a sensor network in a square fashion, with a side length of 300 mm. Such-

made sensing fabric is then laid up, as the 4th ply, together with another seven plies of as-received fabrics, to fabricate an 8-ply orthotropic laminate ($500 \times 500 \times 1.15 \text{ mm}^3$) via the vacuum-assisted resin transfer molding (VARTM) technique. In VARTM, the following procedures are operated in sequence: a peel ply is placed upon and fully covers the stacked eight plies of fabrics; a flow mesh is then placed on the peel ply with two spiral tubes located oppositely; after that, the preform is sealed using a vacuum bag; the de-gas mixed matrix is then injected into the bag to infuse the dry fabrics. The matrix fully cures at the ambient temperature after 24 hours. Replacing conventional metallic wires/cables which inevitably intrude the host structures as commented in Section 2.3.3, highly conductive CNT-films (DexMat[®]) are braided into the fabric, to connect the sensors with the signal acquisition system, shown in Figure 3.1. The resistance of CNT-films, with a planar dimension of $1 \text{ m} \times 1 \text{ mm}$, is only $\sim 20 \Omega$, guaranteeing the good signal transmission. On top of that, the VARTM technique imposes a high pressure to tightly connect the CNT-films with CNT-g-GF sensors, with the abandonment of electrodes. To interrogate the responsivity of the sensing fabrics to high-frequency GUWs, thus-fabricated hybrid GFRPs with a sensing fabric are tested on an ultrasonic measurement system which will be detailed in Section 5.2.3.

The ER of conductive CNT networks (R) embraces three key components, namely the intrinsic resistance of conductive CNTs (R_{CNT}), the contact resistance ($R_{Contact}$)

owing to direct contact among adjacent CNTs and the tunnelling resistance ($R_{Tunnelling}$) induced by the tunnelling effect. It has been concluded that GUWs generally induce microstrains, which are insufficient to cause destruction of conductive pathways (*e.g.*, separation or loss of contacts of CNT nanoparticles) and lead to measurable variation in $R_{Contact}$ [113]; on top of that, the change in R_{CNT} can be neglected due to the superb conductivity of CNTs. To acquire appropriate sensitivity of CNT-g-GF sensors towards GUWs, it is therefore essential to promote the variation in $R_{Tunnelling}$ and trigger the tunnelling effect when GUWs disturb the CNT-g-GF sensors. On the other hand, the quantum tunnelling effect is particularly prominent when the nanoparticles, synthesized CNTs in this work, are in close proximity with others [114]. With such a sensing philosophy, the synthesized CNTs are far preferable to be distributed in a close but not direct contact manner, which can be achieved via regulating the mass fractions of grafted CNTs.

To put the investigation into perspective, Figure 3.6 compares signals, at representative 175 kHz, captured by CNT-g-GF sensors with various loadings of CNTs, observing different response sensitivities. It should be noted that to eliminate the effects induced by the distance and the directivity of wave propagation, the signals captured by the middle sensor on each side are used for comparison. All signals perceived by CNT-g-GF sensors are pre-averaged 1024 times to minimize measurement uncertainty and subsequently filtered with a first-order Butterworth

filter to mitigate ambient noise. To specify, with sparse CNTs (@ 0.38 wt.%), the conductive pathways are discontinuous, Figure 3.3(a), showing non-responsiveness to dynamic strains, in Figure 3.6(a). With gradually increased loadings (@ 0.45 wt.%, 0.64 wt.%), the CNTs come into contact or are in close proximity with neighboring particles to stimulate the piezoresistivity of CNT networks and the CNT-g-GF sensors at these two mass fractions demonstrate responsiveness to GUWs, though relatively weak. Such a phenomenon is attributed to that as can be observed in Figures 3.3(b) and (c), there still exist some bare regions on the GF surface, indicating insufficient formation of conductive pathways. With appropriate mass fractions of CNTs (@ 0.81 wt.%, 0.85 wt.%), the GFs are fully and evenly grafted with CNTs, forming adequate electron transmission paths, Figures 3.3(d) and (e). GUW-induced strains alter the distance of adjacent CNTs, trigger the tunnelling effect and lead to remarkable variation in $R_{tunnelling}$, providing high sensitivity towards GUWs, Figures 3.6(d) and (e). At the weight ratio of 1.07 wt.%, the CNT-g-GF sensor exhibits a reduced sensitivity to GUWs, Figure 3.6(f). That is because at such a loading, the majority of CNTs are distributed in a contact manner, Figure 3.3(f), CNTs entangle and agglomerate one with the other, which suppresses the variation in ER manifested by the sensors, when GUWs introduce dynamic strains to CNT-g-GFs.

To further scrutinize the sensing performance of CNT-g-GF sensors (@ 0.85 wt.%), Figure 3.7 comprehensively depicts their responses towards ultrasonics with a frequency regime from 200 to 375 kHz, arguing that such sensors are capable of precisely capturing dynamic strains with a high signal-to-noise ratio.

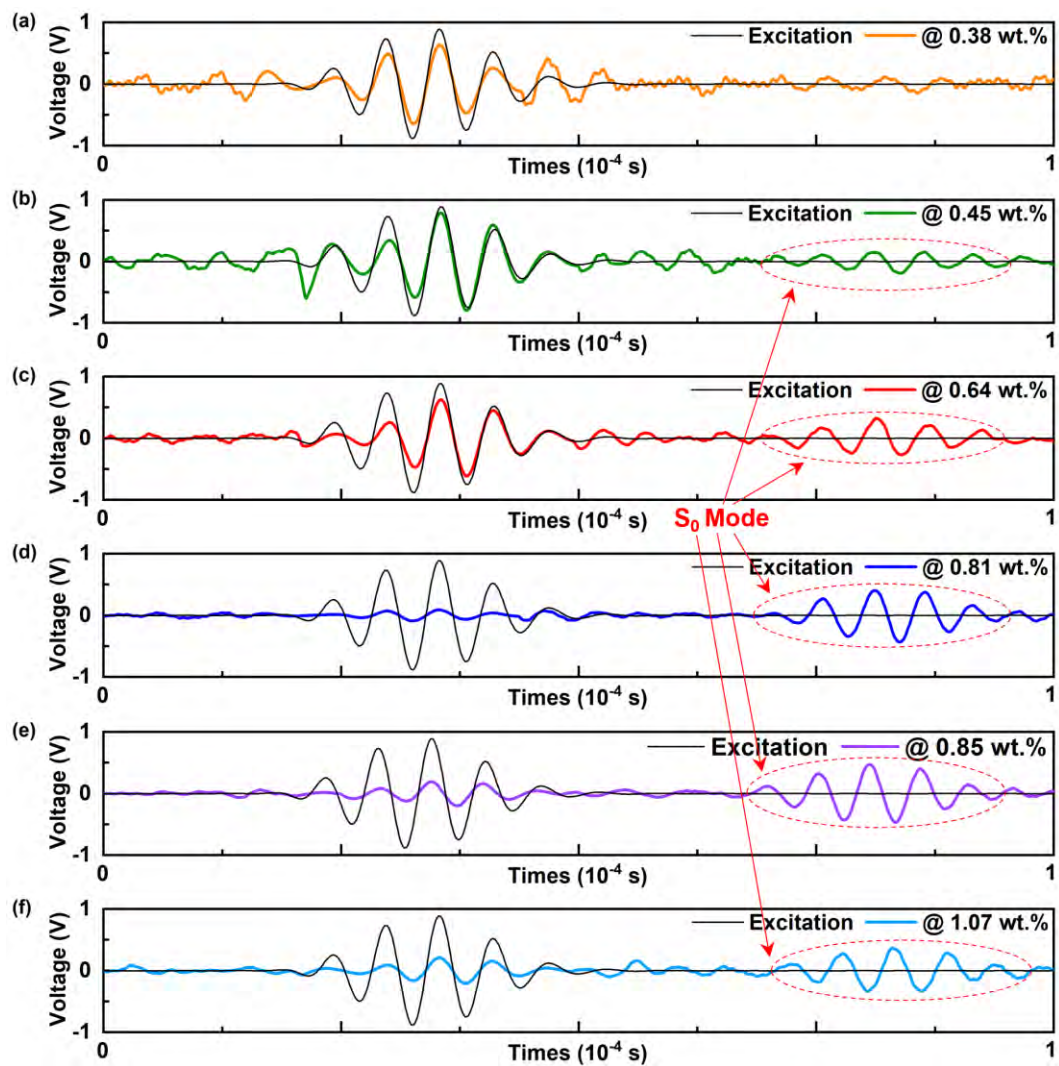


Figure 3.6 Signals captured by CNT-g-GF sensors with different CNT loadings, at 175 kHz.

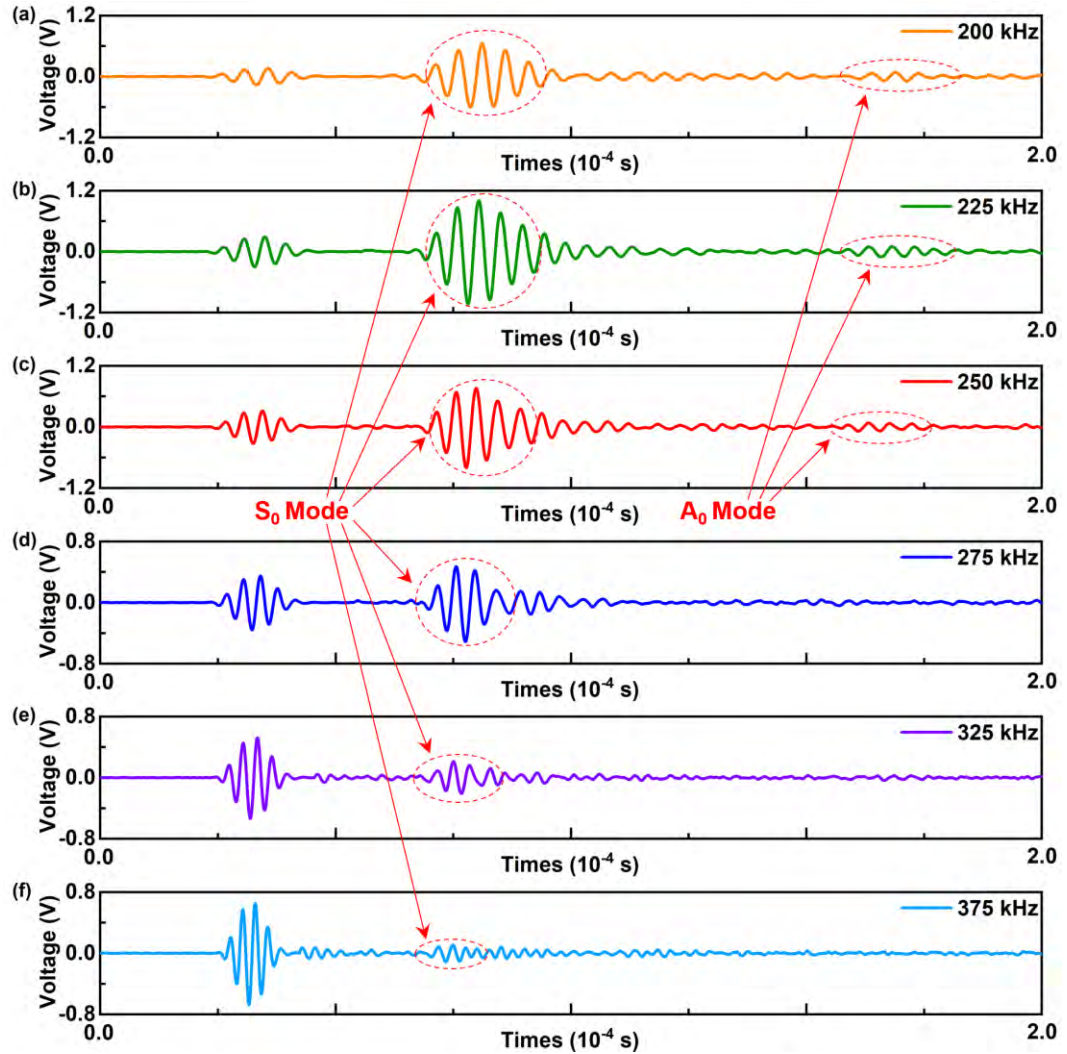


Figure 3.7 GUW signals captured by the CNT-g-GF sensors @ 0.85 wt.%, in a frequency regime from 200 to 375 kHz.

3.5 Tensile Properties

Single fibre tensile test is performed with a dynamic mechanical analyser (TA Instruments® Q800), with a force resolution of 0.001 N. A single fibre is adhered to a thin cardboard support frame containing a 5 mm-long square window which works

as the gauge section of specimen, shown in Figure 3.8. 30 specimens are tested for each group.

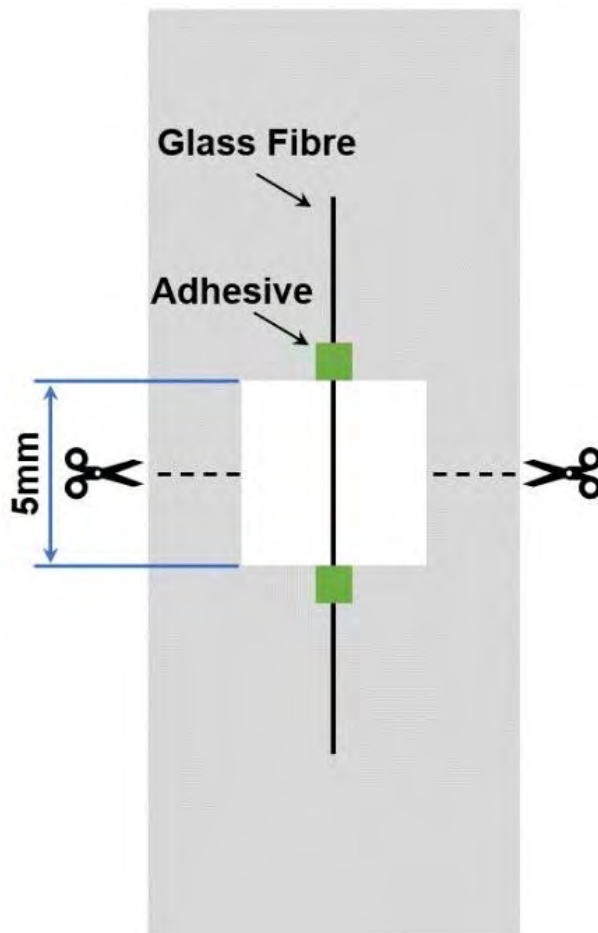


Figure 3.8 Schematic of single fibre tensile specimen.

The Weibull statistical method is recalled to analyze the results of single fibre tensile test, for assessing the axial properties of glass fibres with or without grafted CNTs.

The tensile strength of the fibre can be determined as

$$\sigma = \frac{4F}{\pi d_f^2}, \quad 3.1$$

where F is the force to failure and d_f the fibre diameter. The scattered distribution of the single fibre tensile results shown in Figure 3.9, acquired with both the as-received GFs and the CNT-g-GFs @ 0.85 wt.%, can be attributed to the high variability characteristic of single fibre tensile test. With two-parameter Weibull distribution [115, 116], the experimental data are analyzed using

$$F(\sigma) = 1 - \exp(-L(\sigma / \sigma_0)^{\beta_w}), \quad 3.2$$

where $F(\sigma)$ is the failure probability of fibre breaking under a stress equal to or less than σ , L the length ratio of the reference length (equals to 1 in this work), σ_0 the characteristic fibre strength and β_w the Weibull modulus (shape parameter) indicating the dispersion degree of results. Taking the logarithm form of Equation 3.2,

$$\ln \ln\left(\frac{1}{1 - F(\sigma)}\right) = \beta_w \ln \sigma - \beta_w \ln \sigma_0, \quad 3.3$$

in which the failure probability $F(\sigma)$ comes from

$$F(\sigma) = i / (n + 1), \quad 3.4$$

where n is the total number of specimens and i the i^{th} specimen in sort of tensile strength ranked from small to large. As shown in Figure 3.9, the characteristic strengths of as-received GFs and CNT-g-GFs @ 0.85 wt.%, fitted using the Weibull distribution equation, are 2905 and 2634 MPa, respectively. The slight decrease, by 9.3%, in tensile strength of GFs reveals that the proposed CVD process has minimal impact on the core properties of GFs, benefiting from the relatively short synthesis duration (30 min) and relatively low growth temperature (500 °C).

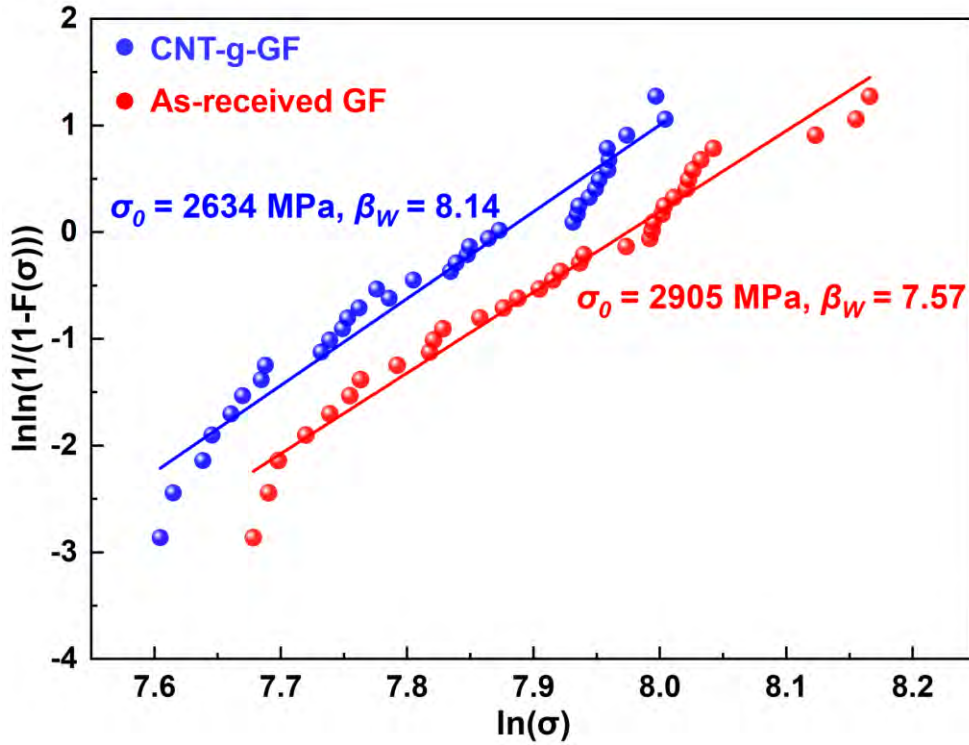


Figure 3.9 The Weibull distribution of fracture stress of all tested specimens, with acquired characteristic strengths and Weibull moduli.

Additionally, to investigate the influence of proposed CVD process on the tensile attributes of corresponding integrated composites, the tensile test issued for fibre-reinforced polymer matrix composite is conducted on a universal testing system (INSTRON[®] 5982) with a crosshead speed of 2 mm/min. Three 8-ply orthotropic laminates ($250 \times 25 \times 1.15 \text{ mm}^3$), each containing a layer of CNT-grafted sensing fabric (the 4th ply), are prepared, along with another three original laminates for comparison.

Figure 3.10 displays the tensile results of laminates with or without a CNT-grafted sensing fabric. In Figure 3.10(a), the obtained stress-strain curves argue high degree of consistency in elastic attributes of two sets of laminates. It can be acquired from Figure 3.10(b) that there are only slight variations in averaged ultimate tensile strength (0.39%) and Young's modulus (0.96%) of laminates with or without a CNT-grafted sensing fabric, confirming no significant degradation due to sensor integration.

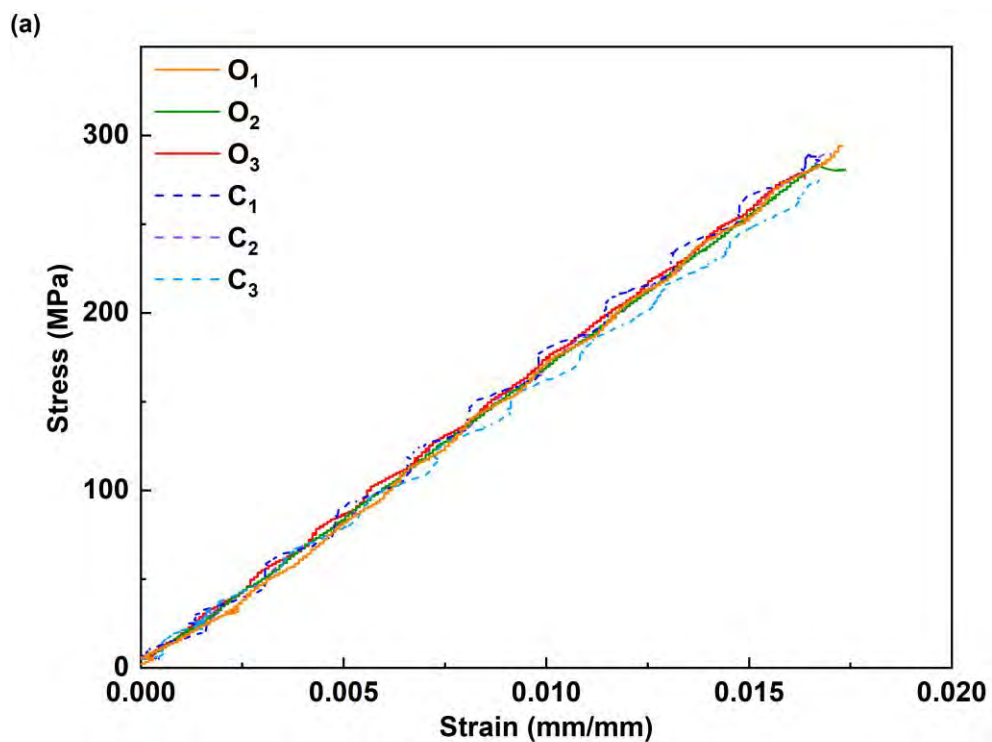


Figure 3.10 Stress-strain curves of composites (C_1 - C_3 : with a CNT-grafted fabric; O_1 - O_3 : without the CNT-grafted fabric); and (b) averaged tensile moduli and strengths of composites with or without a CNT-grafted fabric.

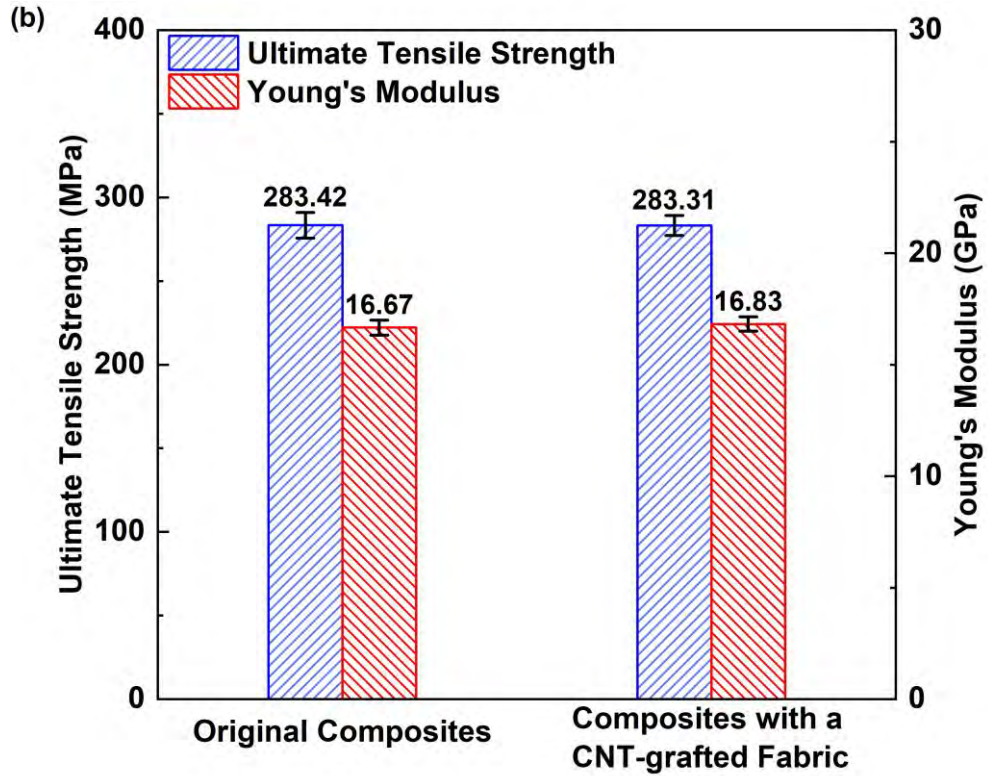


Figure 3.10 *Cont.*

3.6 Electrical Resistance-based State Diagnosis of Composites with Carbon Nanotube-grafted Glass Fibre Sensors

With the above method, CNTs are also initiated to grow in a specific region ($120 \times 10 \text{ mm}^2$) of a GF fabric, to form an area CNT-g-GF sensor with hairy CNT networks.

The CNT-g-GF sensor in the fabric spans across the whole width of the fabric (to facilitate the circuit connection). Such-made fabric layer is then inserted into another eight plies of GF fabrics during stacking, as the middle layer, to fabricate a 9-ply orthotropic GF laminate following a VARTM technique. The CNT-g-GF sensor is

circuited via a pair of electrodes ($10 \times 10 \text{ mm}^2$ each), as shown in Figure 3.11. Externally connected, the electrodes and cables avoid intrusion to the laminate. To eliminate the effects of fluctuating pressure and temperature on the ER measurement, a vacuum leak test is carried out prior to the infusion of resin, ensuring a constant pressure applied; and the preform is kept in a thermotank ($25 \text{ }^\circ\text{C}$) through the entire infusion and cure processes, to remain a stable ambient temperature.

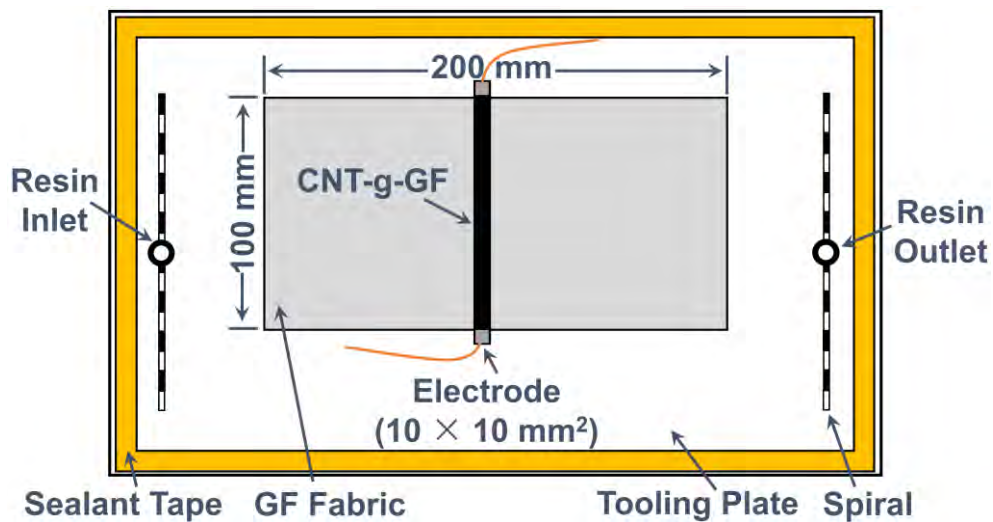


Figure 3.11 Fabrication of a GFRP laminate with an area CNT-g-GF sensor via the VARTM technique.

Figure 3.12 correlates the ER measured by the CNT-g-GF sensor with the status of epoxy cure through laminate fabrication. In Figure 3.12, ΔR and R_0 signify the variation in ER and the initial resistance of the CNT-g-GF sensor, respectively. In VARTM, the entire cure progress of epoxy embraces three sequential stages, namely:

- 1) the infusion stage – the injection of epoxy resin, to impregnate fabrics; 2) the

equilibrium stage – the full infiltration of low-viscosity epoxy resin with fabrics, to infill dried spots and voids; and 3) the cure stage – the full consolidation of epoxy in the laminate. As observed,

- 1) in the infusion stage: the epoxy resin is quickly introduced to infuse both the fabrics and the CNT-g-GF sensor in the laminate, leading to a rapid increase in the measured ER, Figure 3.12(b). During this period, epoxy modules penetrate into and expand CNT networks and remarkably alter the original nanostructure of networks, as a result of which both the tunnelling resistance (due to a higher dielectric constant of matrix compared with that of air) and the contact resistance (due to the loss of contact among adjacent CNTs) of the CNT-g-GF sensor increase;
- 2) in the equilibrium stage which takes ~40 min: the progressive epoxy cure contributes to a high ER value, in Figure 3.12(c). This is attributable to the fact that after infilling the majority of the inter- and intra-roving voids in fabrics, the resin molecules continue to migrate into and interrupt the CNT networks, at a reduced speed owing to the barriers formed by the micro- or nano-scale dry voids within the CNT networks, leading to a mild increase in ER; and
- 3) in the cure stage: with continuous polymerization of epoxy as cure develops, the volume shrinkage of epoxy resin becomes dominant, causing CNTs closer one to another. As a consequence, the ER measured by the CNT-g-GF sensor tends to decrease, as noted in Figure 3.12(d).

The above three cure stages, in which the CNT networks in the CNT-g-GF sensor are morphologically altered as cure develops, are illuminated schematically in Figure 3.12(e). In terms of the ER measured by the CNT-g-GF sensor, the cure progress of composites can be monitored continuously.

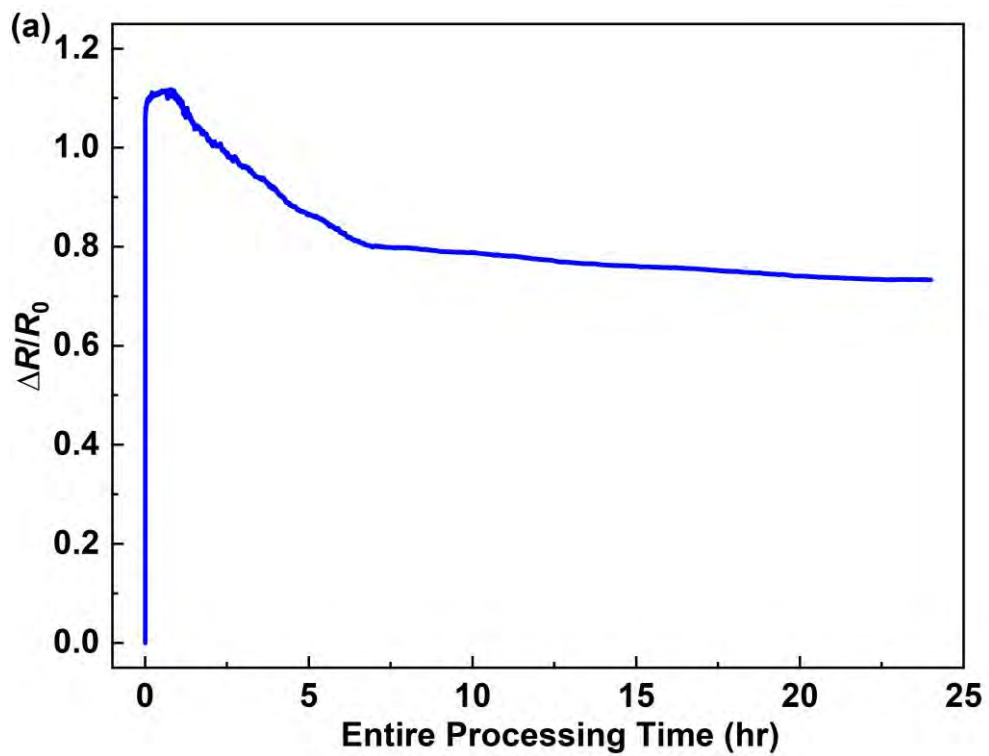


Figure 3.12 Variation in ER measured by the area CNT-g-GF sensor in a VARTM process: (a) entire process; (b) infusion stage; (c) equilibrium stage; (d) cure stage; and (e) morphological alteration of the CNT-g-GF sensor in different stages.

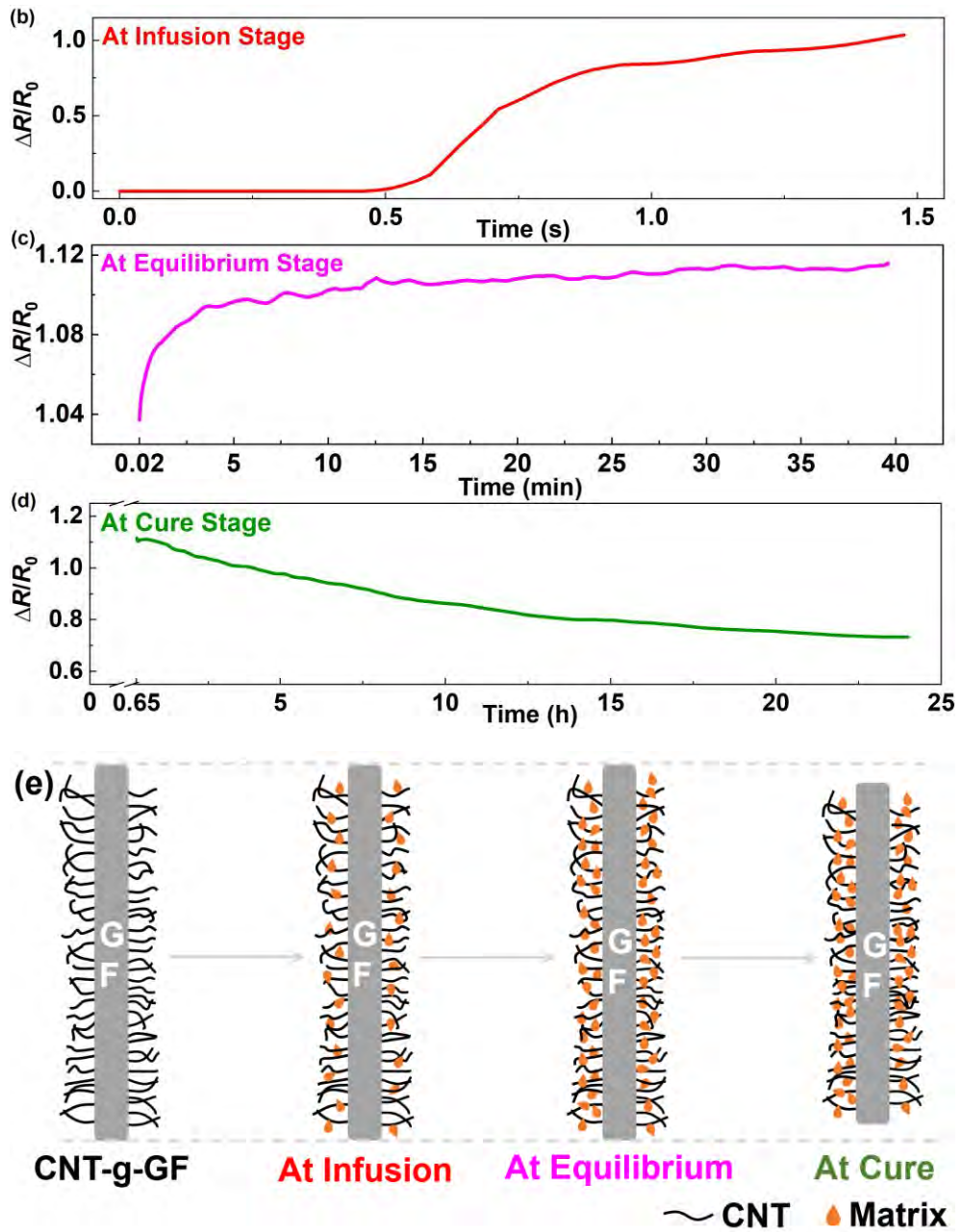


Figure 3.12 Cont.

Upon full cure, the finished GFRP laminate with the CNT-g-GF sensor possesses the capability of self-sensing in-service loads. A series of tests under different loading conditions are conducted for validation. With specimen depicted in Figure 3.13, Figure 3.14 representatively shows the response of the laminate under a quasi-static

tensile load (tensile rate: 3 mm/min) on a universal test platform (INSTRON® 5982). Within a strain scope of 0~1.5% (in an elastic deformation range of the laminate), the CNT-g-GF sensor-measured ER varies linearly against the load applied, in Figure 3.14. To quantify the measurement sensitivity, a gauge factor (G) is defined as

$$G = \frac{\Delta R}{R_0 \cdot \varepsilon}, \quad 3.5$$

where $\Delta R = R - R_0$ (R : the current resistance; R_0 : the initial resistance), and ε the strain induced by the applied load. With Equation 3.5, G is calculated to be 30.2, which is remarkably higher than that of a standard strain gauge which is ~2.0 in general.

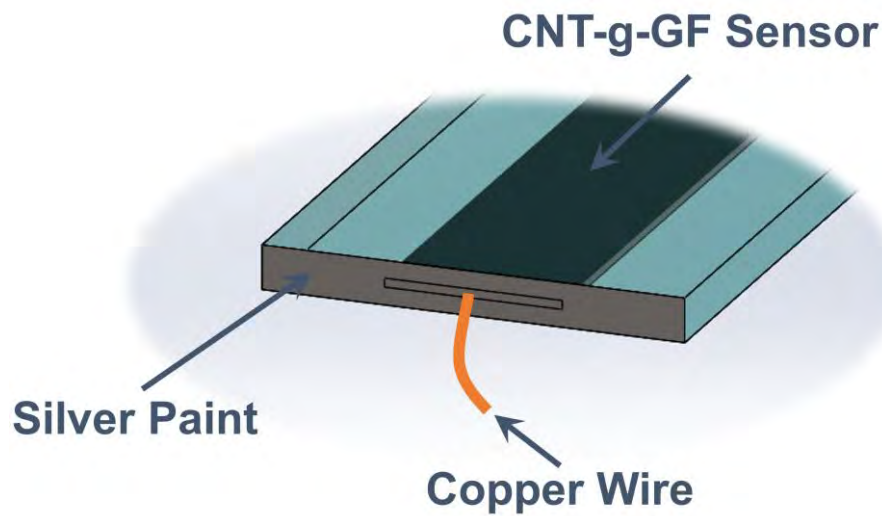


Figure 3.13 A laminate with the CNT-g-GF sensor for sensing in-service loads.

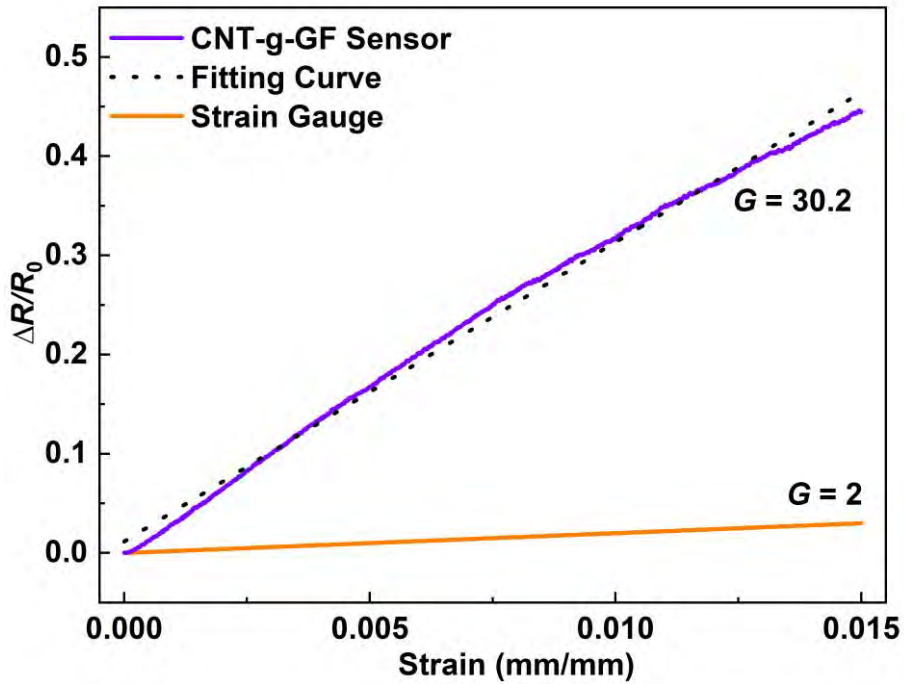


Figure 3.14 Variation in the ER measured by the CNT-g-GF sensor when the laminate is subject to a quasi-static load.

3.7 Summary

In conclusion, the fundamental characteristics of synthesized CNTs have been thoroughly interrogated. *In situ* grafting of CNTs on GF fabrics is achieved by CVD with a low CNT growth temperature (500 °C), to configure sensing fabrics with CNT-g-GF sensors. The Raman spectra of synthesized CNTs confirm their high graphitization degree, with I_d/I_g ratios < 0.89 . The success in growing CNTs at such a low temperature is a joint consequence of appropriate selections of hydrocarbon source, catalyst precursor and carrier gas, which differentiate this study from reported work. Single fibre tensile test (ASTM C1557) reveals the slight degradation,

by 9.3%, in single fibre tensile strength owing to exposure to the CVD process while the fibre-reinforced polymer matrix composite tensile test (ASTM D3039) confirms unmeasurable variation in mechanical attributes of hybrid composites owing to the sensor integration. Through tailoring the mass fractions of CNTs, the CNT-g-GF sensors @ 0.85 wt.% demonstrate the highest sensitivity towards GUVs in virtue of the quantum tunnelling effect, with a broad frequency range from 175 to 375 kHz. Additionally, synthesized CNTs endow the composites with the ER-based continuous monitoring capability from cure through service. As a demonstration, ER measured by an area CNT-g-GF sensor is correlated with epoxy cure in three key stages during composite fabrication, whereby to implement cure self-monitoring. Thus-fabricated laminate with the CNT-g-GF sensor also possesses the capability of self-sensing in-service loads, with a high gauge factor of 30.2. In addition to implement either ER- or GUV-based monitoring, the proposed integrated functional composites own the potential in electromagnetic shielding, lightning strike protection, *etc.*

CHAPTER 4

Implantable Nanocomposite Sensors

4.1 Introduction

In the above chapter, sensing fabrics with carbon nanotube (CNT)-grafted glass fibre (GF) sensors are developed to implement either electrical resistance (ER) measurement-based or guided ultrasonic wave (GUW)-based monitoring of glass fibre-reinforced polymer composites, while not at the cost of mechanical attributes of host composites. Both the matrix modification or fibre decoration approaches are only adaptive to composites reinforced by dielectric fibres. Nonetheless, for critical load-bearing components, carbon fibres (CFs) are preferred owing to their higher specific strength and modulus, which brings a problem that it is mandatory to insulate the sensors, electrodes and wires from conductive CFs to prevent the short-circuit. Motivated by such a recognition and by expanding the above work to develop nano-engineered sensors for GUW-based monitoring of carbon fibre-reinforced polymer (CFRP) composites, this chapter takes advantage of recent technological advances in nanocomposites and additive manufacturing, aspiring to a new genre of

ultrathin, implantable piezoresistive sensors. Such sensors are desired to be capable of perceiving broadband signals and implementing G UW-based structural integrity monitoring (SIM) for CFRPs, yet without compromising the composites' original integration, mechanical properties and electromechanical performance. A specific kind of conductive polymer nanocomposites (CPCs) is prepared, formulated with graphene nanoplatelets (GNPs) and polyvinylpyrrolidone (PVP), as the sprayable ink for sensor fabrication. The sensors are deposited on dielectric membranes made of partially pre-cured B-stage epoxy, and then electrified using highly conductive CNT-film-made wires, to be implanted into CFRPs and form a sensor network.

4.2 Sensing Mechanism: Quantum Tunnelling Effect

G UWs for structural health monitoring (SHM) are often generated in a range from several hundred kilohertz (kHz) to several megahertz (MHz), within which G UWs feature a magnitude of the order of microstrain or even nanostrain. Crucial to the faithful acquisition of G UWs is the sensitivity of the sensor material to external disturbances. To endow sensors with sufficient sensitivity to G UWs of high frequency and ultralow magnitude, the quantum tunnelling effect is exploited. The tunnelling effect, a quantum mechanical phenomenon, is triggered at nanoscale in a morphologically proper conductive network, when the insulative barriers among

neighboring conductive nanoparticles are smaller than a critical threshold (of the order of several nanometers in general) [114], under which electrons can move through these barriers and consequently induce the tunnelling current [117]. The percolation threshold represents a critical fraction of conductive nanoparticles in the formed networks, beyond which a slight increase in the content of conductive nanoparticles can lead to a remarkable leap in the electrical conductivity of the material [118]. Because the barriers to break (so that tunnelling current can be triggered) are of the order of several nanometers only, it is possible for a GUW, even of ultralow magnitude, to alter inter-distances among nanoparticles and activate the tunnelling effect, provided the nanoparticle-formed network is morphologically appropriate and the content of conductive nanoparticles is close to the percolation threshold. A triggered tunnelling current alters the piezoresistivity manifested by the nanocomposite material.

Driven by such a quantum tunnelling effect-based sensing mechanism, a new type of nanocomposite-based piezoresistive sensor is developed. Upon even dispersion of nanoparticles in matrix, the electrical properties of synthesized nanocomposites can be calibrated using the percolation theory [118], as

$$\sigma_c \propto (f - f_c)^{t_{pt}}, \text{ when } f > f_c \quad 4.1$$

where σ_c signifies the electrical conductivity of nanocomposites, f the fraction of nanoparticles, f_c the percolation threshold, and exponential t_{pt} a constant reflecting

the dimensionality of nanocomposites [114]. The ER of the sensor (R) embraces three key components: the intrinsic resistance of nanoparticles ($R_{Nanoparticle}$), the contact resistance due to direct contact among nanoparticles ($R_{Contact}$) and the tunnelling resistance among nanoparticles ($R_{Tunnelling}$) that is induced by the tunnelling effect, namely

$$R = R_{Nanoparticle} + R_{Contact} + R_{Tunnelling} . \quad 4.2$$

The tunnelling effect is particularly prominent when the content of conductive nanoparticles is close to the percolation threshold of the nanoparticle-formed conductive networks, and therefore $R_{Tunnelling}$ dominates the responsivity of a sensor when the sensor perceives a GUW signal, schematically shown in Figure 4.1 – this is different from the case when the sensor is subject to an external load with a relatively large magnitude (*e.g.*, structural vibration or tensile-induced strain), under which the change in ER of the sensor is mainly attributed to the breakup of conductive networks or loss of contact among nanoparticles (*i.e.*, change in $R_{Contact}$).



Figure 4.1 Schematic diagram of the quantum tunnelling effect.

4.3 Preparation of Implantable Sensors

4.3.1 Synthesis of Nanocomposite Ink

A standard solution mixing process is applied to prepare the sprayable nanocomposite ink. PVP (Sigma-Aldrich® PVP K-30) is chosen as the matrix and GNPs (TANFENG®; thickness: <5 nm; diameter: 10-50 µm; SSA: 360-450 m²/g; and purity: >95 wt.%) are selected as the modified nanofillers to form conductive pathways in CPCs. CPCs thus-produced are dispersed in 20 ml ethanol (Honeywell® 24194). The solution is magnetically stirred at 500 rpm at an ambient temperature (25 °C) for 2 hours, followed with sonication-assisted dispersion (Brandson® 5800 Ultrasonic Cleaner, 40 kHz) for 1 hour, to facilitate even dispersion of GNPs in PVP. 10 ml DI-water is added to augment the condensation point of solvent to circa -42 °C [119]. The complete preparation process of the sprayable CPC ink is depicted in Figure 4.2.

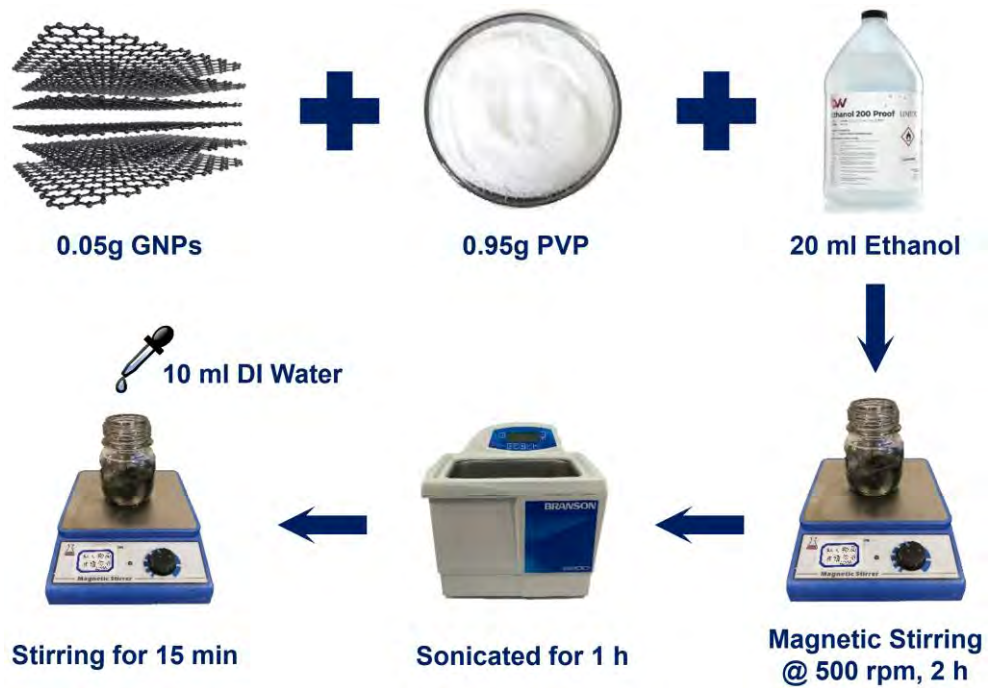


Figure 4.2 Flowchart of the preparation process of the sprayable CPC ink.

To determine the percolation threshold of CPCs, different GNPs-to-PVP mass ratios, varying from 4.0 to 8.0 wt.%, are investigated, respectively. The ER of CPCs is calibrated with a digital graphical sampling multimeter (Keithley[®] DMM7510). The obtained correlation between the electrical conductivity (σ_c) of the prepared CPCs and GNPs loadings is shown in Figure 4.3. Applying the power-law function linear fitting [61] on Equation 4.1, the percolation threshold of CPCs is determined to be 4.93 wt.%.

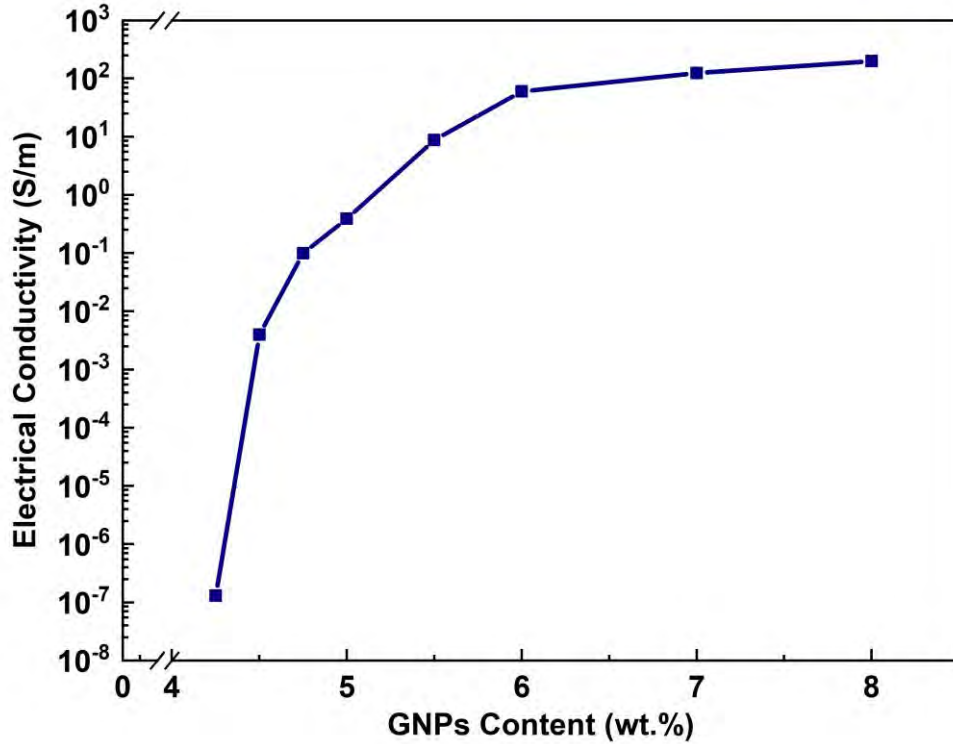


Figure 4.3 Correlation between σ_c of CPCs and loadings of GNPs.

4.3.2 Deposition of Nanocomposite Ink on the B-stage Epoxy Film

The sensors, measuring $20 \times 3 \text{ mm}^2$ each, are fabricated via spraying the aqueous CPCs onto a substrate – a partially pre-cured B-stage epoxy film, using an airbrush (HD-130). The scanning speed of nozzle (5 cm/s), stream pressure (0.35 MPa) and distance of target to nozzle (10 cm) are precisely controlled in the spraying process to warrant consistent initial resistance of sensors.

To make the substrate, B-stage epoxy is spread on a high temperature-resistant release film (AIRTECH® WL5200B nonperforated peel ply) using a spreader at 80 °C, which is proven to be effective to reduce the viscosity of epoxy and prevent

uncontrollable pre-cure, Figure 4.4. The epoxy film thus-produced presents the following attributes: 1) the same material properties as the matrix of CFRPs, to which the sensors are to be implanted; 2) the strong bonding formed among sensors, CF prepreps and CNT-film-made wires (to be detailed in Section 4.3.3); and 3) high flexibility (therefore adaptive to a curved structure) and customizable thickness. These merits warrant high compatibility and non-invasive attribute of implanted sensors with CFRPs. To limit possible flowing of epoxy in following cure, the epoxy film is partially pre-cured, whereby to minimize the effect of epoxy on the morphology of nanocomposite ink deposited on the substrate. The cure degree of epoxy is determined using the differential scanning calorimetry (DSC) technique (Mettler Toledo[®] DSC3). The cure degree (α) can be defined as the ratio of the released reaction enthalpy $H(t)$ till a time t of interest, and H_T signifies the total reaction enthalpy which is to be obtained via integrating the heat flow over the entire exothermic peak area [120], as

$$\alpha = \frac{H(t)}{H_T}. \quad 4.3$$

The evolved heat flow and corresponding cure degree (α) measured by DSC at 130 °C is shown in Figure 4.5 and Table 4.1 exemplarily lists five groups of measurement of α against the heating duration.

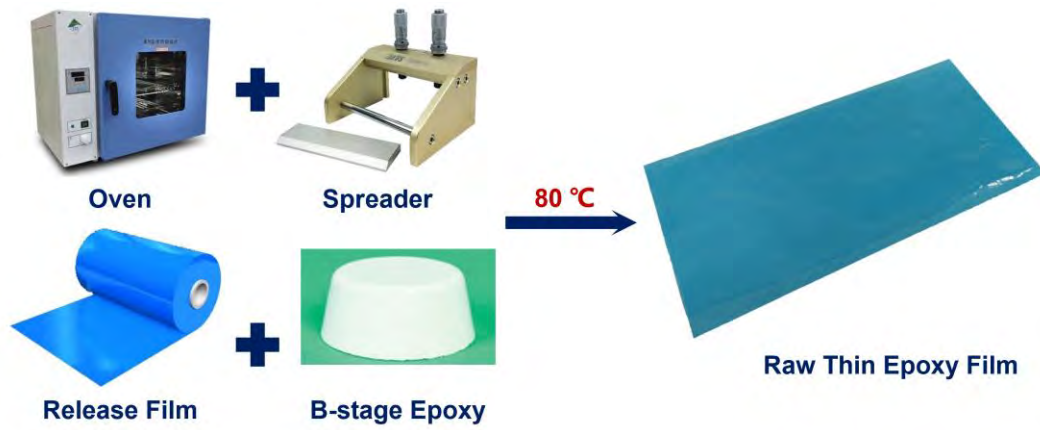


Figure 4.4 Fabrication of the B-stage Epoxy Film.

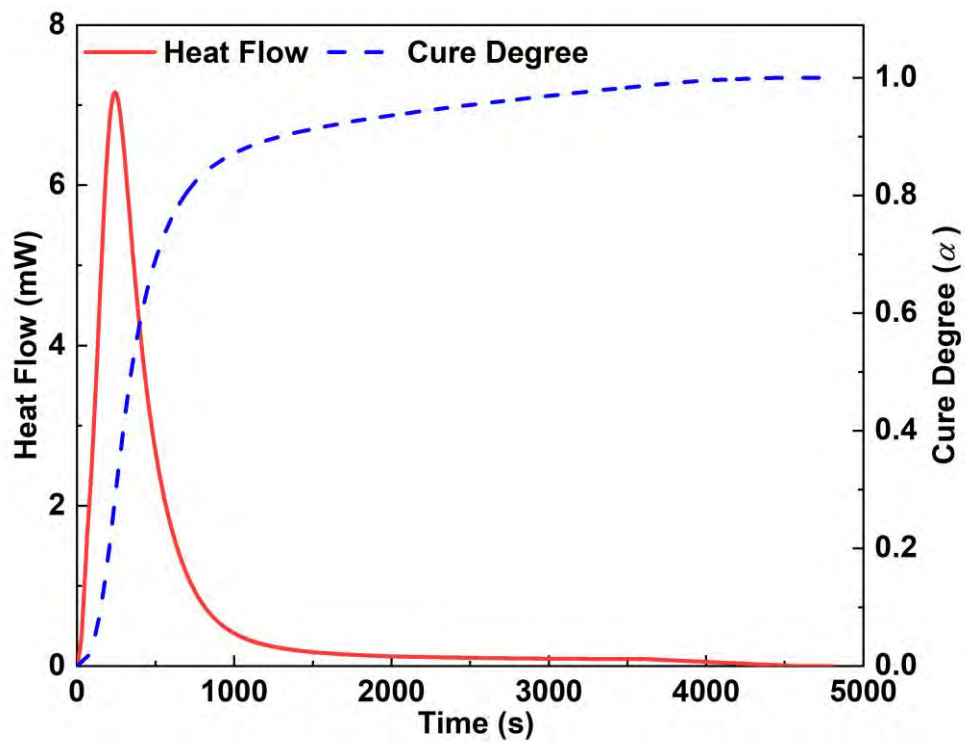


Figure 4.5 Heat flow and cure degree vs. time measured by DSC @ 130 °C.

Table 4.1 Cure degree vs. heating duration.

Heating Duration [s]	154	206	251	296	348
Cure Degree [α]	0.1	0.2	0.3	0.4	0.5

During deposition of the nanocomposite ink on the substrate, the epoxy film remains active and adhesive, the morphology of which may alter under a thermal load. To evaporate the solvent exhaustively, the epoxy film is treated with a freeze-drying process. Figure 4.6 compares the morphology of a series of nanocomposite inks which are deposited on epoxy films processed with different pre-treatments, in which different heating durations are adopted. For comparison, the nanocomposite ink is also deposited on an epoxy film which is not processed with such freeze-drying. It can be observed that the original morphology of the nanocomposite ink deposited on a raw epoxy film without any pre-treatment is not maintained through the cure process, as a result of the resin flowing. With an increase in the pre-cure degree, the deposited nanocomposite ink demonstrates improved deposition quality, and a good morphology sustains when $\alpha = 0.4$ afterwards. Also noted in Figure 4.6 is that exhaustive evaporation of solvent facilitates a precise shaping of the nanocomposite ink on the substrate.

Another pre-cured B-stage epoxy film is thus produced and then placed atop the above epoxy film on which the nanocomposite ink has already been deposited. Both films, atop and beneath the sensors, respectively called “*upper membrane*” and “*lower membrane*” in what follows, serve as a pair of dielectric membranes, to insulate the sensors from the conductive CFs upon sensor implantation in CFRPs.

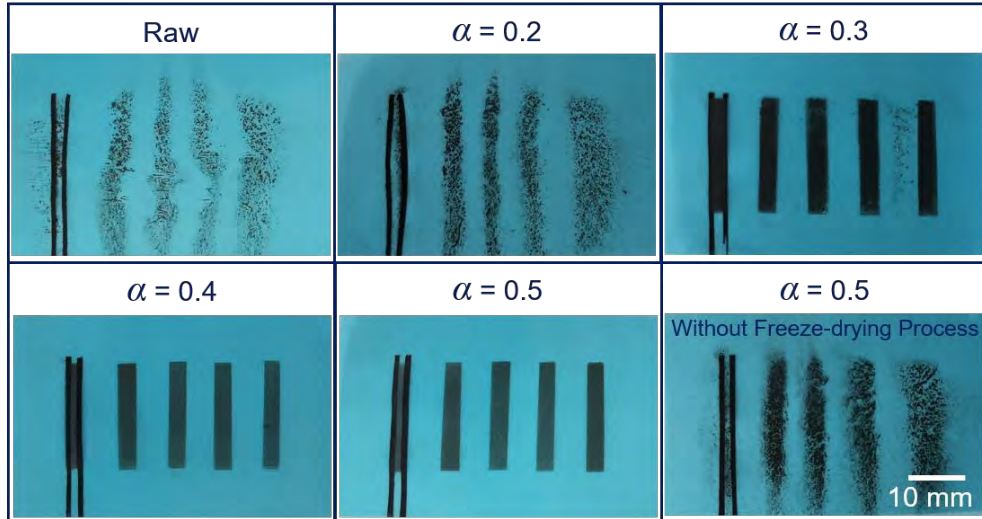


Figure 4.6 Comparison of ink deposited-epoxy films processed with different pre-treatments.

4.3.3 Fabrication of Carbon Nanotube-film-made Wires

As the sensor-associated electrodes and wires inevitably intrude the composites when being embedded, it is therefore essential to develop a communication system (*e.g.*, electrodes and circuits) with minimized intrusion to host structures. As displayed in Figure 4.7, different types of mediums are tried to make the wires, each of which possessing obvious advantages and drawbacks. In detail, the T300 CF bundle (with one thousand filaments) are too thick to be fully infused with above prepared epoxy films, which may bring mechanical weak points to structures; the CNT fibre is fragile though highly conductive; the copper foil, a metallic cable, may cause discontinuity of structures. To further minimize the intrusion to the host composites and guarantee the good transmission quality of signals when sensors (along with

associated wires) are implanted, highly conductive wires are fabricated using CNT-film (DexMat[®]) made of pure CNTs, Figure 4.7. The wire is tailored ~1 mm in width and ~10 microns in thickness. With key parameters listed in Table 4.2, the linear resistance of CNT-film-made wire is only ~20 Ω per meter in length and 1 mm in width.

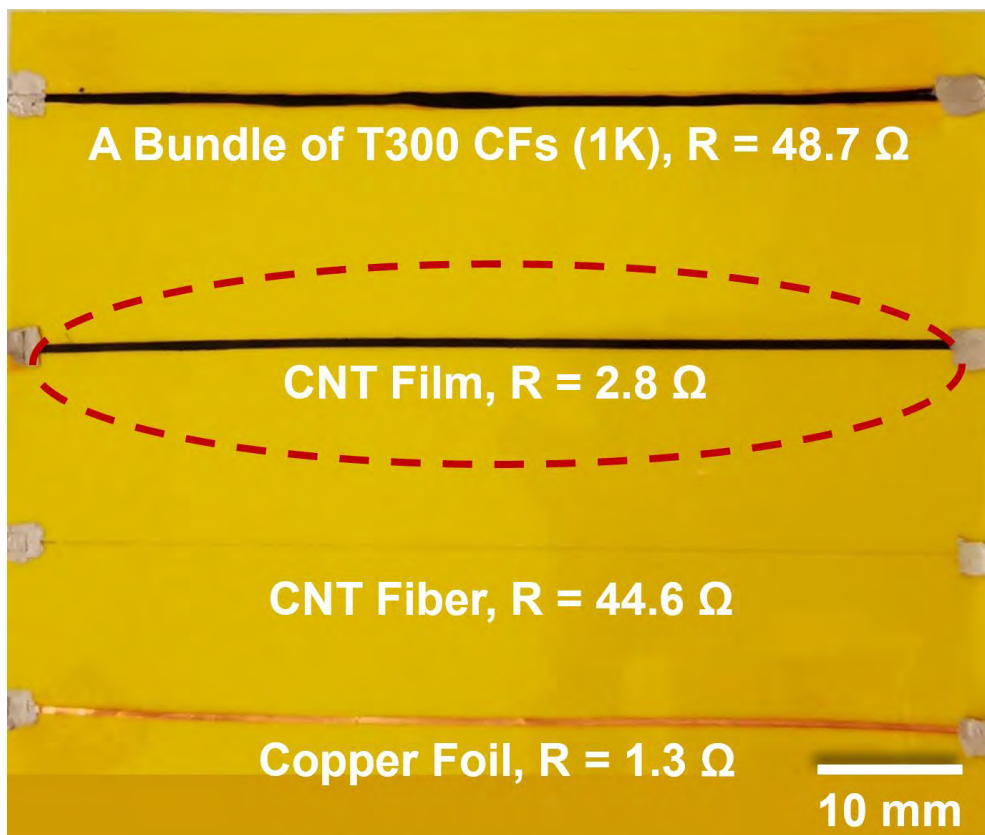


Figure 4.7 Morphology and ER of tried mediums to make the wires.

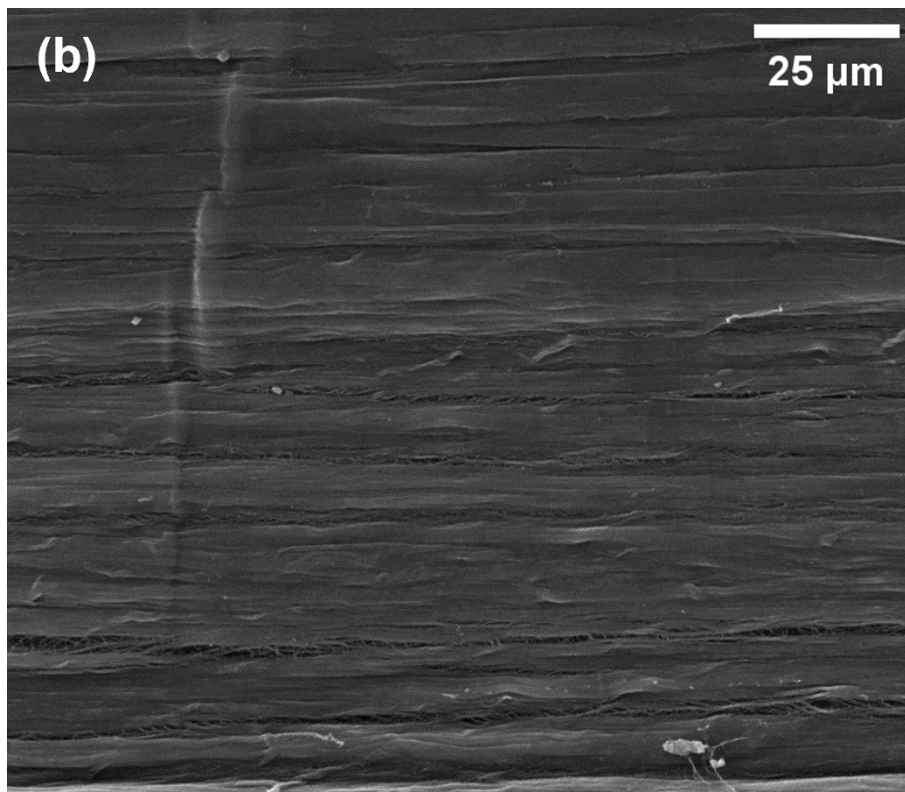


Figure 4.8 (a) Photograph (DexMat[®]); and (b) SEM image of the CNT-film.

Table 4.2 Key parameters of CNT-film-made wires.

Width [mm]	1±0.1
Thickness [micron]	10±5
Linear Density [g/m]	0.02±0.01
Linear Resistance [Ω /m]	20.0±3.0
Conductivity [MS/m]	5±1
Tensile Strength [MPa]	500±100

Two CNT-film-made wires are aligned along the two opposite edges of each sensor, prior to the encapsulation by the upper membrane. Thus-encapsulated sensors are then fully cured under a vacuum-assisted heating condition (130 °C, 60 min). Notably, different from conventional sensors such as PZT wafers internally embedded in or surface mounted on composites, which are electrified via a pair of electrodes, the vacuum-assisted cure process in this approach imposes a high pressure to indent the CNT-film-made wires into nanocomposite sensors, guaranteeing a good conductive connection but without additional electrodes. Abandoning the conventional electrodes further minimizes the intrusion of the implanted sensors to the host composites.

Lightweight, flexible, small and ultrathin, thus-fabricated sensors can be deployed in a large quantity in a CFRP structure to configure a dense sensor network. The

complete fabrication process of the sensors is illustrated in Figure 4.9, and sensors produced in their final fashion are pictured in Figure 4.10.

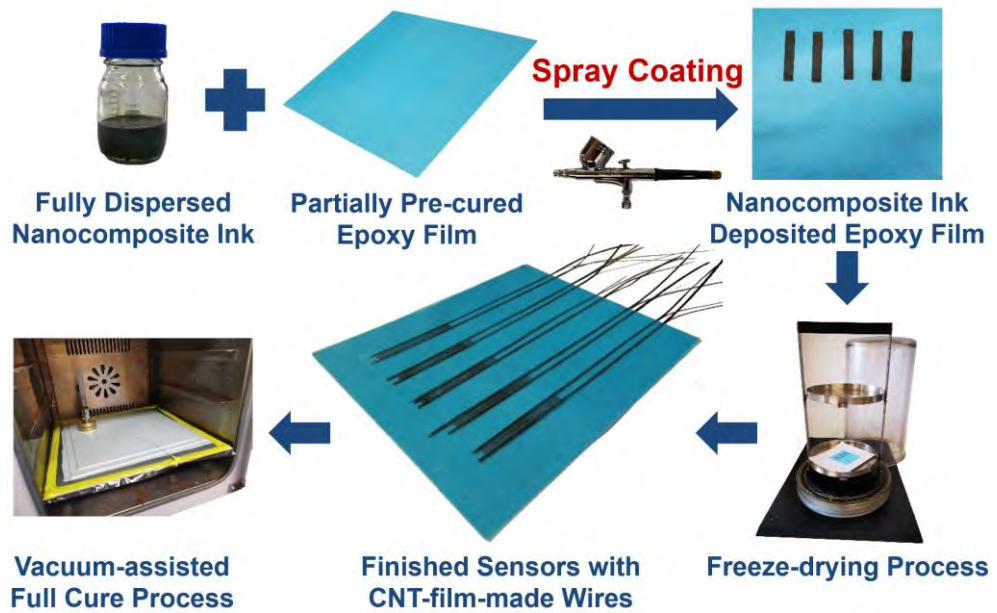


Figure 4.9 Flowchart of the fabrication process of implantable sensors.

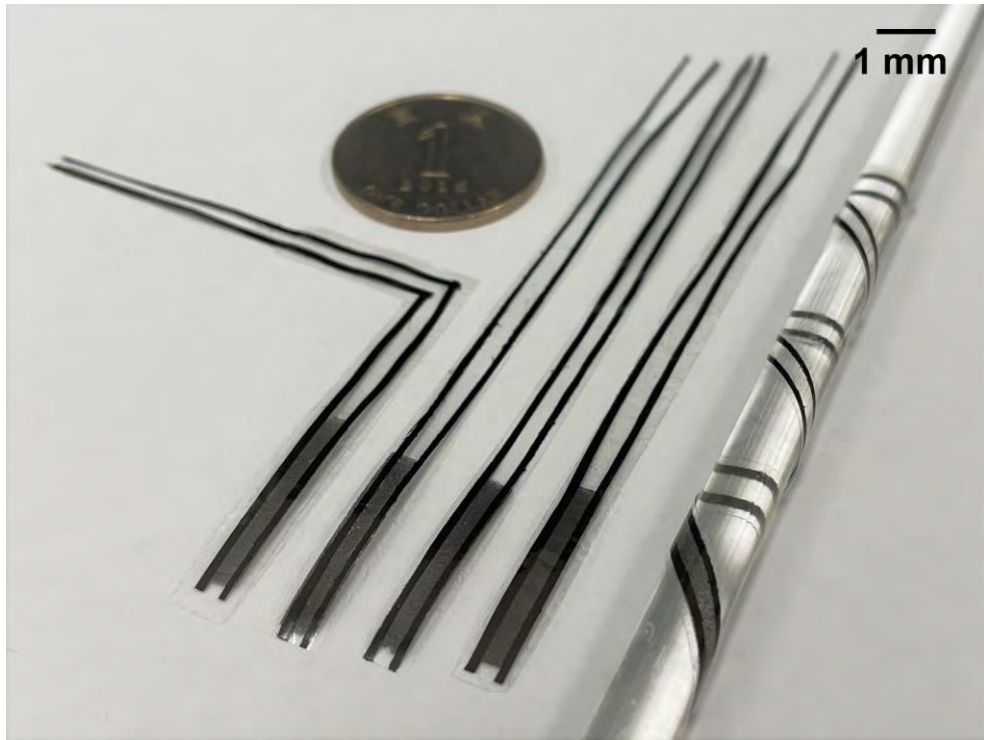


Figure 4.10 Photograph of fabricated nanocomposite sensors, with a sensor wrapped on a thin rod (diameter: 8mm) showing the good flexibility of the sensor.

4.4 Implantation of Networked Sensors into Composites

A series of 8-layer quasi-isotropic CFRP laminates of different dimensions, following a stacking sequence of $[0^\circ/90^\circ/45^\circ/-45^\circ]_s$, are made using unidirectional (UD) CF preregs (Torayca[®] T300), to each of which the fabricated nanocomposite sensors are implanted to form a sensor network, as schematically illustrated in Figure 4.11. A standard autoclaving cure cycle (Econoclave[®] EC1.2MX2.4M) is followed with key parameters listed in Table 4.3. Figure 4.12 schematically demonstrates the

consumable lay-up applied in the autoclaving cure cycle. Upon full cure, the nominal thickness of each CFRP laminate measures 1.15 mm approximately. Each laminate is then trimmed using a water jet cutter (OMAX[®] PROTOMAX). Figure 4.13 representatively shows a CFRP laminate (300 × 300 mm²), with four implanted nanocomposite sensors, under preparation and in its finished fashion.

Table 4.3 Key parameters of a standard autoclaving cure cycle.

Stage	1	2	3	4	5	6	7
Temperature [°C]	T ₀		80		130		T ₀
Heating Rate [°C/min]		+1.5		+1.5		-1.5	
Duration [min]			30		60		
Pressure	Vacuum bag: -25 inHg						
	Autoclave: 150 psi						

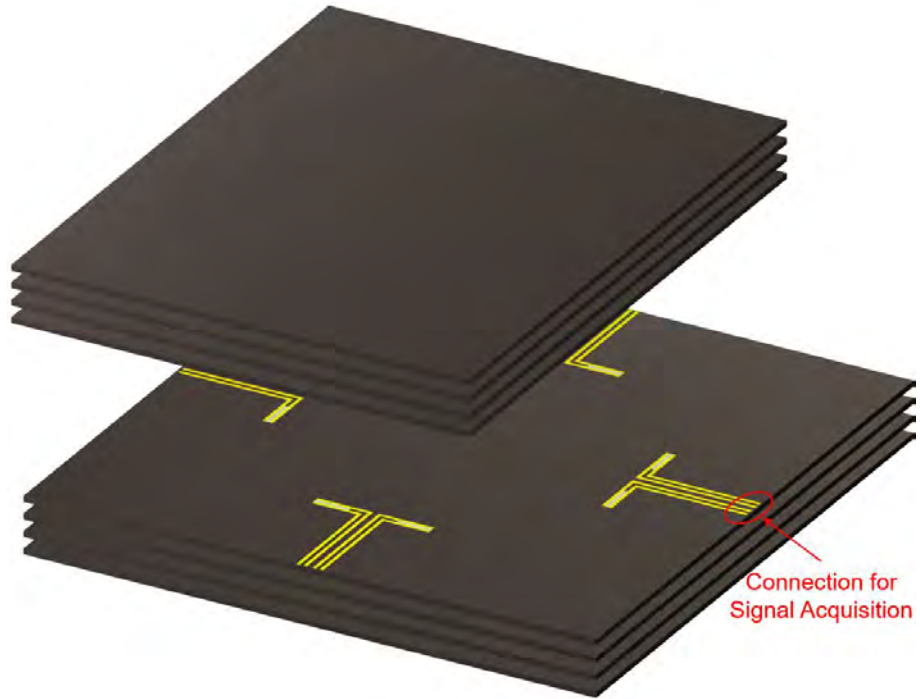


Figure 4.11 Schematic of a CFRP laminate with an implanted sensor network.

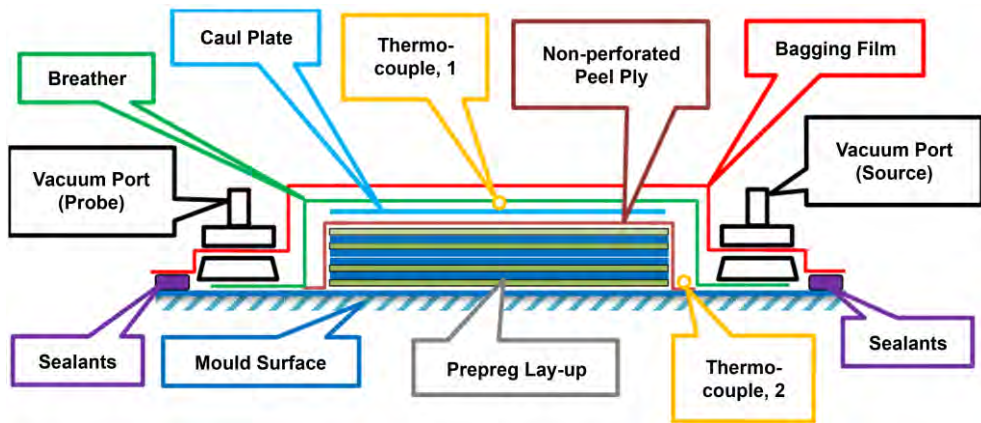


Figure 4.12 The applied consumable lay-up in the autoclaving cure cycle.

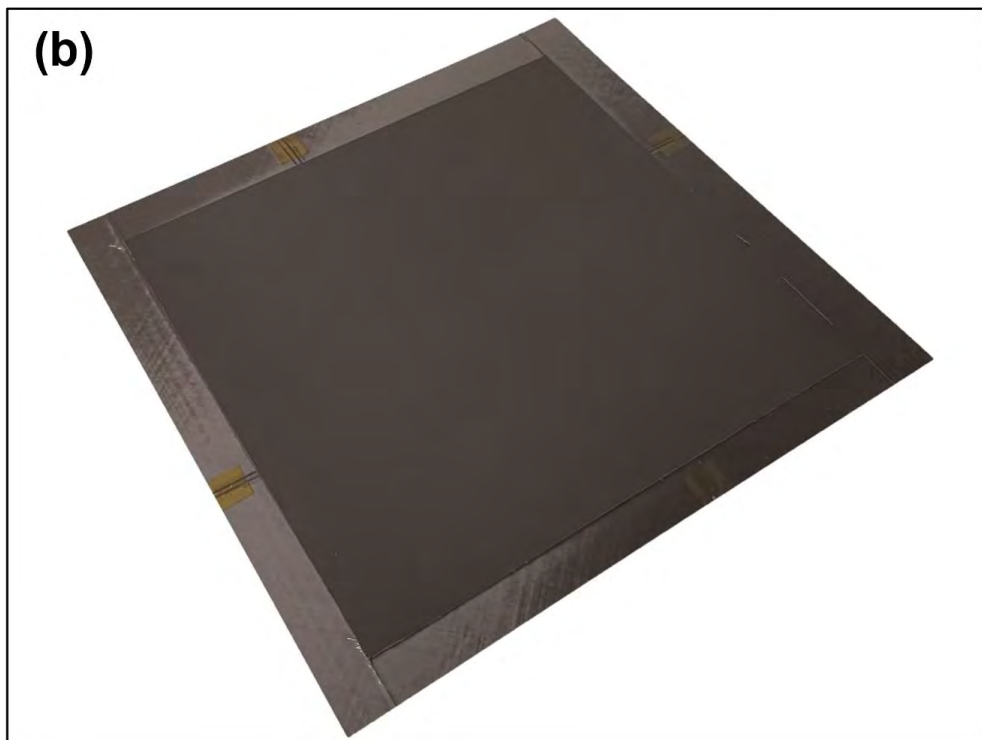
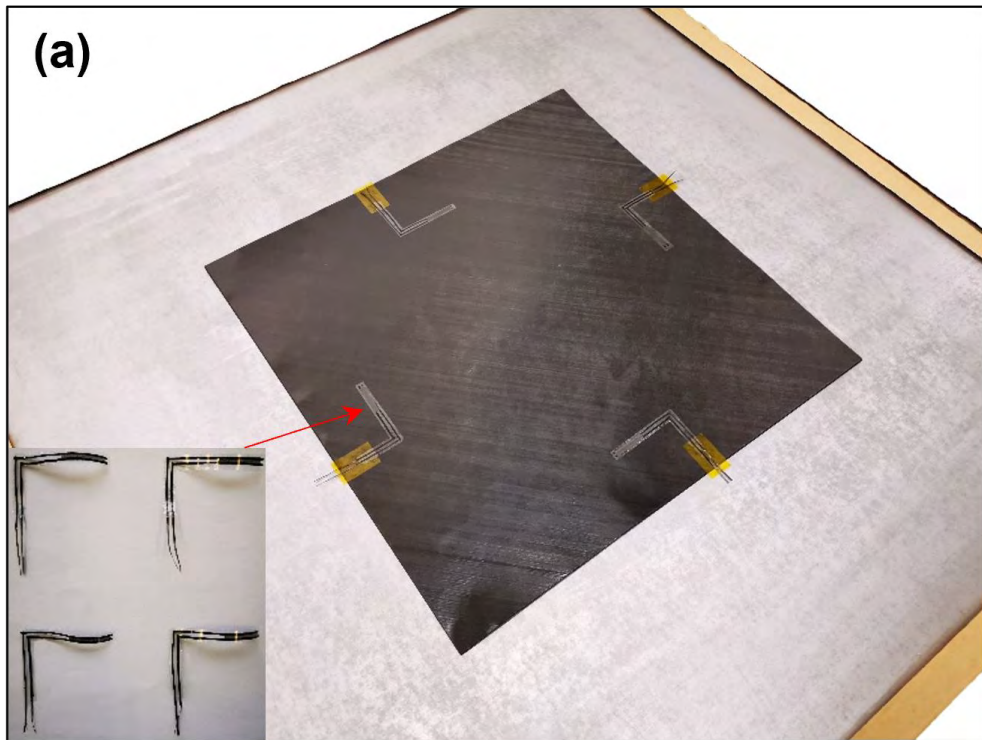


Figure 4.13 A CFRP laminate with four implanted nanocomposite sensors: (a) under preparation; and (b) in its finished fashion.

4.5 Morphological Characterization

To gain an insight into the nanoscale morphology of the fabricated nanocomposite sensors and the microscopic structure of the sensor-implanted CFRP laminate, the morphological characterization is performed on a scanning electron microscopy (SEM) platform (TESCAN[®] Vega 3), with representative SEM images displayed in Figures 4.14, 15 and 16. It is observed in Figure 4.14(a) that GNPs are evenly dispersed in PVP matrix and in Figure 4.14(b) at a smaller scale. The even and uniform distribution of GNPs in PVP is a prerequisite to trigger the tunnelling current when the GUW traverses the sensor. Figure 4.15(a) shows the entire cross-section of a CFRP laminate with an implanted sensor with CNT-film-made wires. The thickness of the implantable sensor including its wires measured in Figure 4.15(b) is $\sim 45 \mu\text{m}$. Figure 4.16(a) shows the vicinity of the implanted sensor, and at a smaller scale in Figure 4.16(b), in both of which it can be noted that the interface between the composite matrix and the sensor (including wires) is obscure, implying a high degree of compatibility of the nanocomposite sensor with CFRPs. In conclusion, a neglectable degree of intrusion from implanted sensors and their associated wires to the laminate is noted.

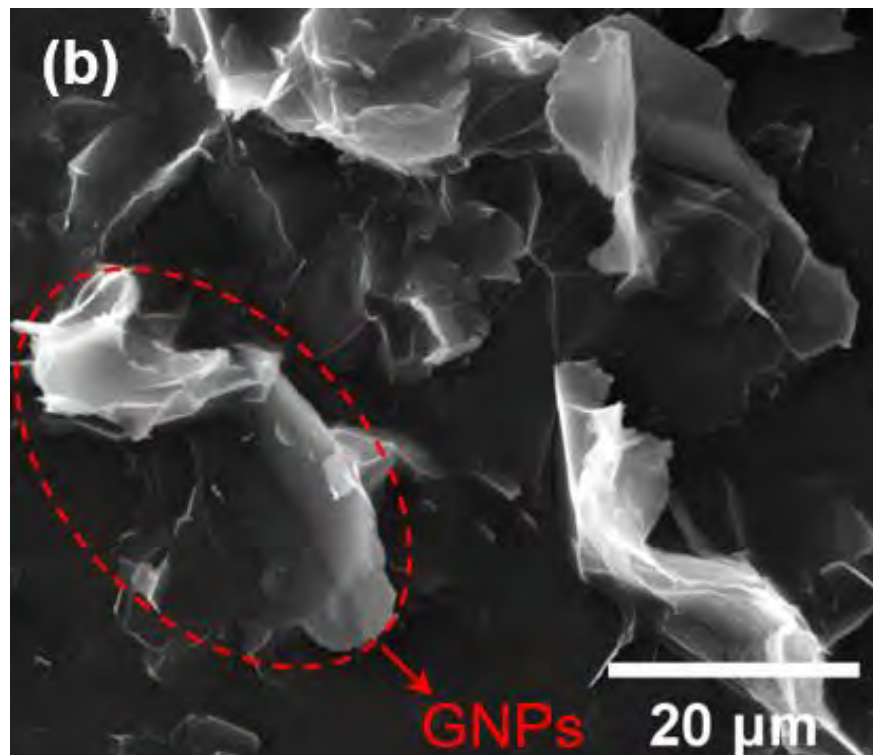
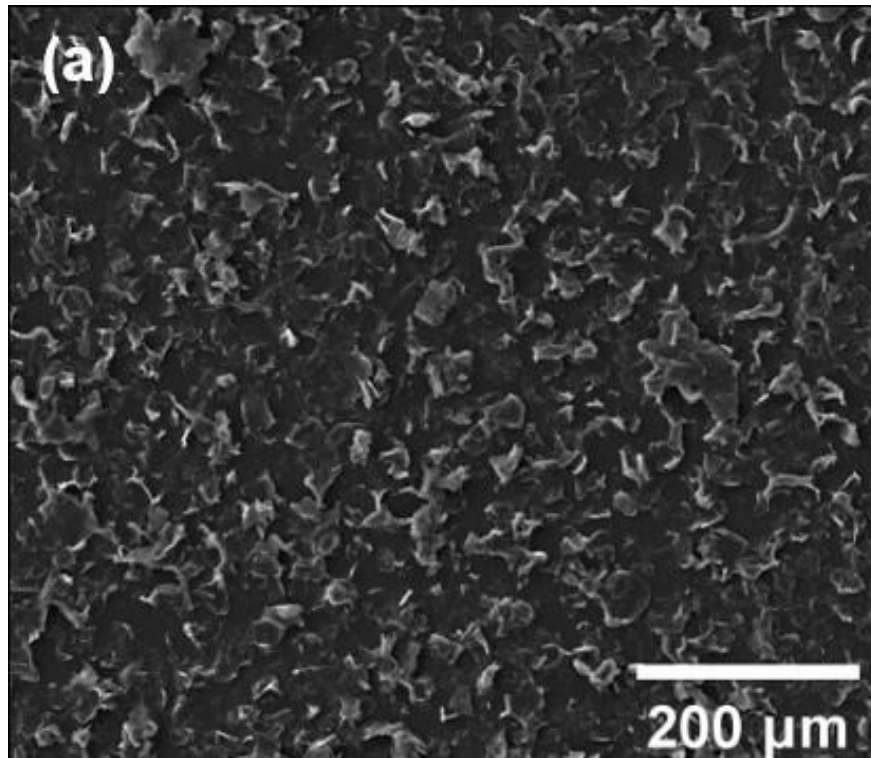


Figure 4.14 SEM images of the GNPs/PVP nanocomposite sensor, at two different

scales.

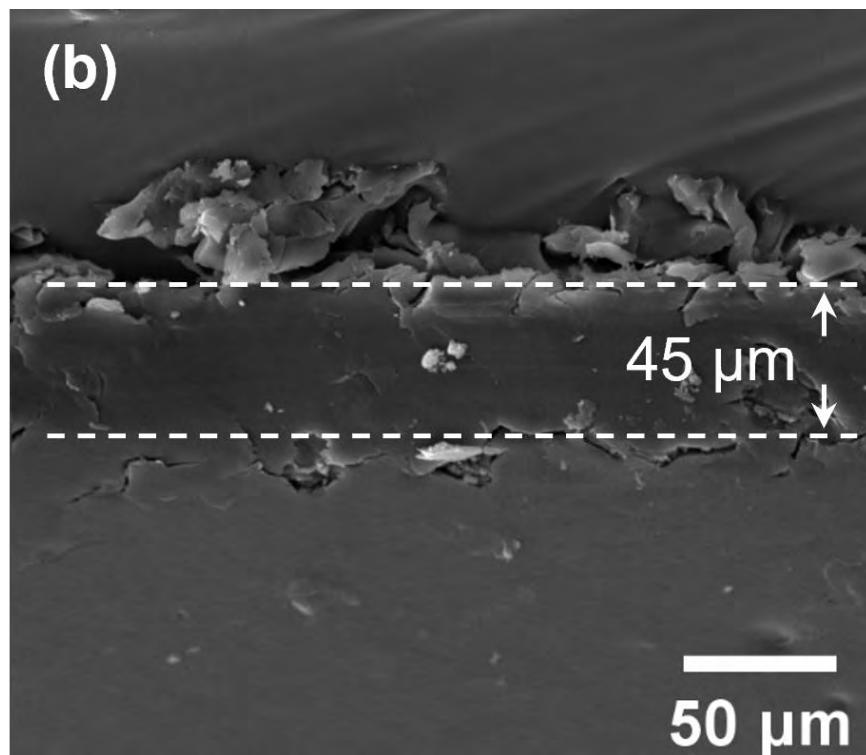
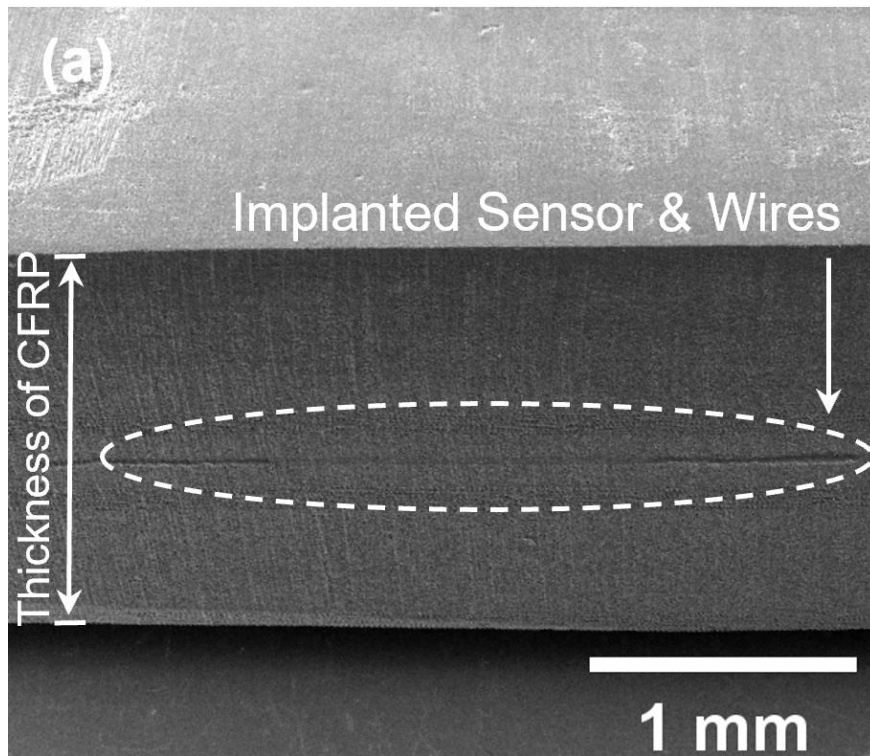


Figure 4.15 (a) Cross-sectional view of a CFRP laminate with an implanted sensor and wires; (b) an individual implantable sensor.

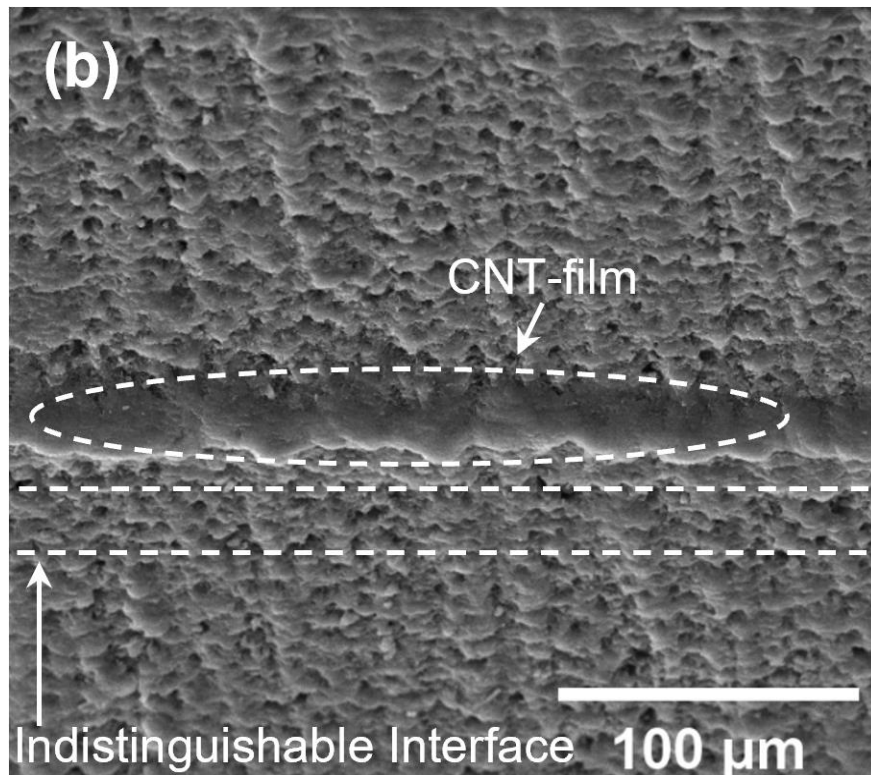
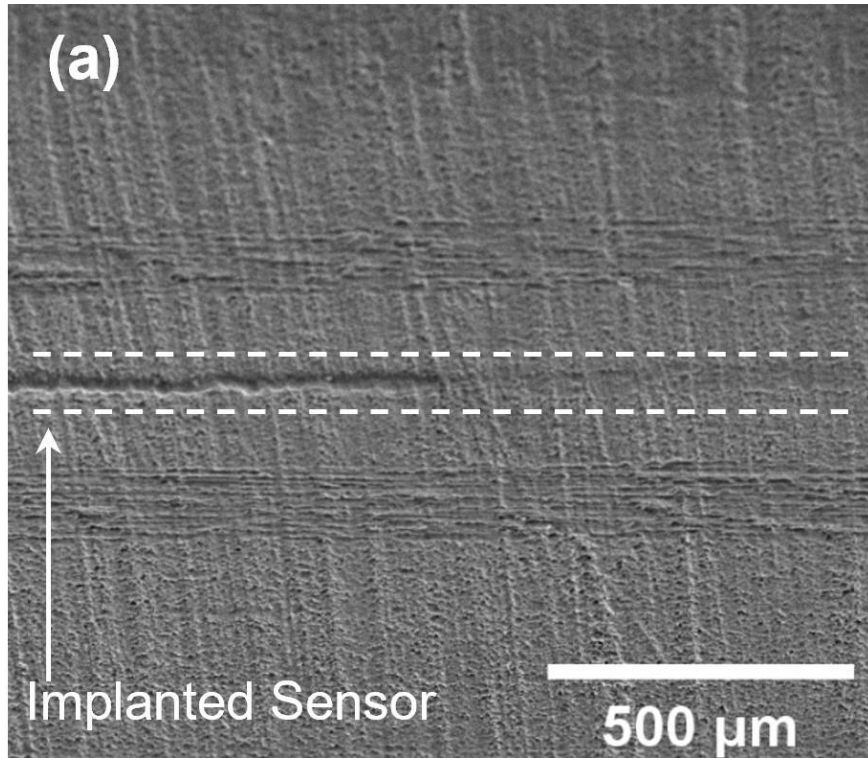


Figure 4.16 (a) Vicinity of the implanted sensor; and (b) the interface between the implanted sensor and host composite.

4.6 Summary

In conclusion, the sprayable nanocomposite ink formulated with GNPs and PVP are tailored to acquire the percolation threshold (4.93 wt.%) of conductive nanoparticles, to provide sufficient tunnelling paths within nanocomposites. Thus-tailored nanocomposites are deposited on dielectric membranes made of partially pre-cured ($\alpha = 0.4$) B-stage epoxy films and electrified using highly conductive CNT-film-made wires, to produce implantable sensors with thickness of $\sim 45 \mu\text{m}$. Morphological investigation via SEM confirms the even distribution of GNPs in PVP matrix and high compatibility between the implanted sensors and the host CFRPs, which are two essential prerequisites to obtain favourable performances of CFRPs with implanted sensors in both mechanical and dynamic response domains.

CHAPTER 5

Characterization of Composites with Implanted Sensors

5.1 Introduction

The fundamental characteristics of thus-fabricated implantable nanocomposite sensors have been investigated to prove their potential in perceiving broadband dynamic strains and visually inspected high compatibility with host carbon fibre-reinforced polymer (CFRP) composites in Chapter 4. With implanted sensors, responses of CFRP laminates, when subjected to quasi-static loads, medium-frequency vibrations and high-frequency guided ultrasonic waves (GUWs), respectively, are investigated *in situ*. More importantly, to scrutinize possible degradation in mechanical properties of CFRP laminates due to sensor implantation, two types of mechanical tests – the tensile and flexural tests, are conducted in accordance with ASTM standards. In each type of test, five CFRP laminates, each implanted with a thus-fabricated implantable sensor, are prepared in accordance with the manufacturing approach described in Section 4.4, along with another five

counterpart laminates of the same dimension but without any implanted sensor, for comparison.

5.2 Dynamic Response Analysis

5.2.1 Quasi-static Tensile Loads

An 8-ply quasi-isotropic CFRP laminate ($250 \times 25 \times 1.15 \text{ mm}^3$), with an implanted sensor placed between the 1st and 2nd plies, is prepared and applied with a quasi-static tensile load, as shown in Figure 5.1. A digital graphical sampling multimeter (Keithley[®] DMM7510) measures the change in electrical resistance (ER) of the implanted sensor via explored carbon nanotube (CNT)-film-made wire ends during the loading process, as depicted in Figures 5.1(b) and (c). For comparison and calibration, the normal strain at the laminate cross-section, where the sensor is implanted, is measured using an advanced video extensometer (AVE). Figure 5.2(a) presents the stress-strain correlation of the laminate, accompanying with the ER variation of the implanted sensor versus the applied strain, to observe a linear change in ER prior to yielding. To calibrate the sensitivity of the sensor, the gauge factor (G) defined in Section 3.6 is recalled.

In Figure 5.2, G is determined to be 34.5 within the elastic regime, which is much higher than that of a standard strain gauge (~ 2.0 in general). As seen in Figure 5.2(b),

$\Delta R/R$ curve is in consistency with the strain curve (provided by the AVE) within the elastic domain, while the large discrepancy is only observed after yielding, which can be attributed to the inconsistency of the gauge length for the AVE measurement, as seen in Figure 5.1(b) – AVE measures the strain between the two gauge points (25 mm) while the implanted sensor reflects the local strain (1 mm gap between two CNT-film-made wires).

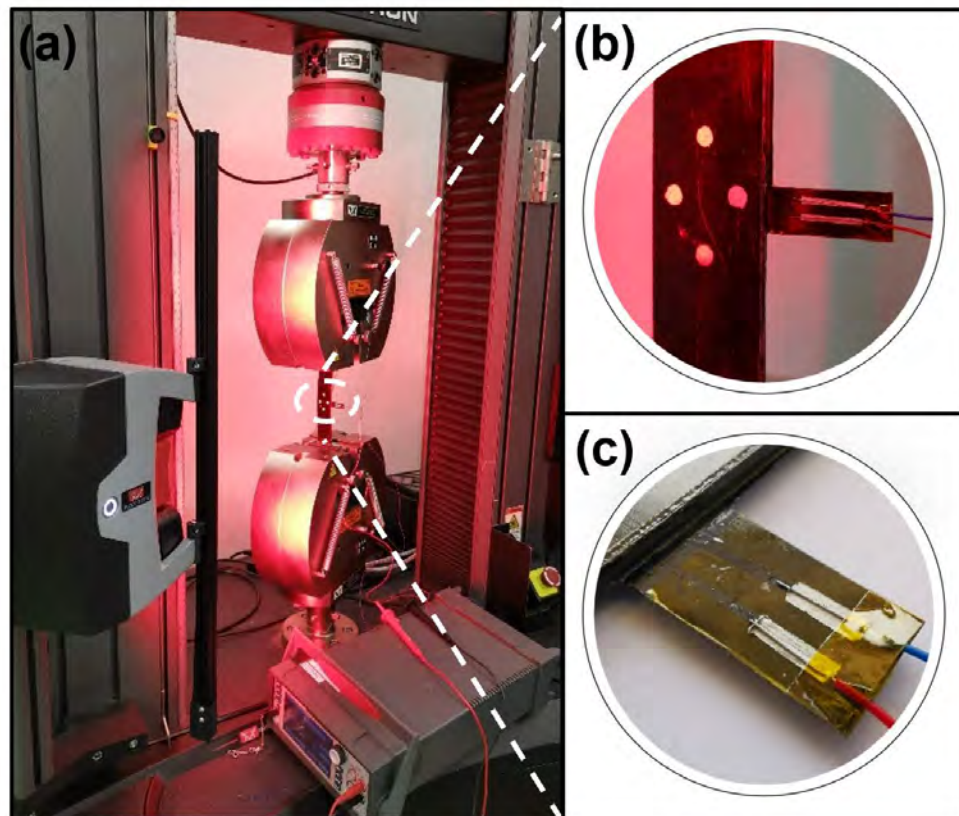


Figure 5.1 (a) Set-up for measuring the strain in the laminate under a quasi-static load; (b) gauge points on the laminate for AVE measurement, beneath which the sensor is implanted; and (c) the junction of the implanted sensor to the multimeter.

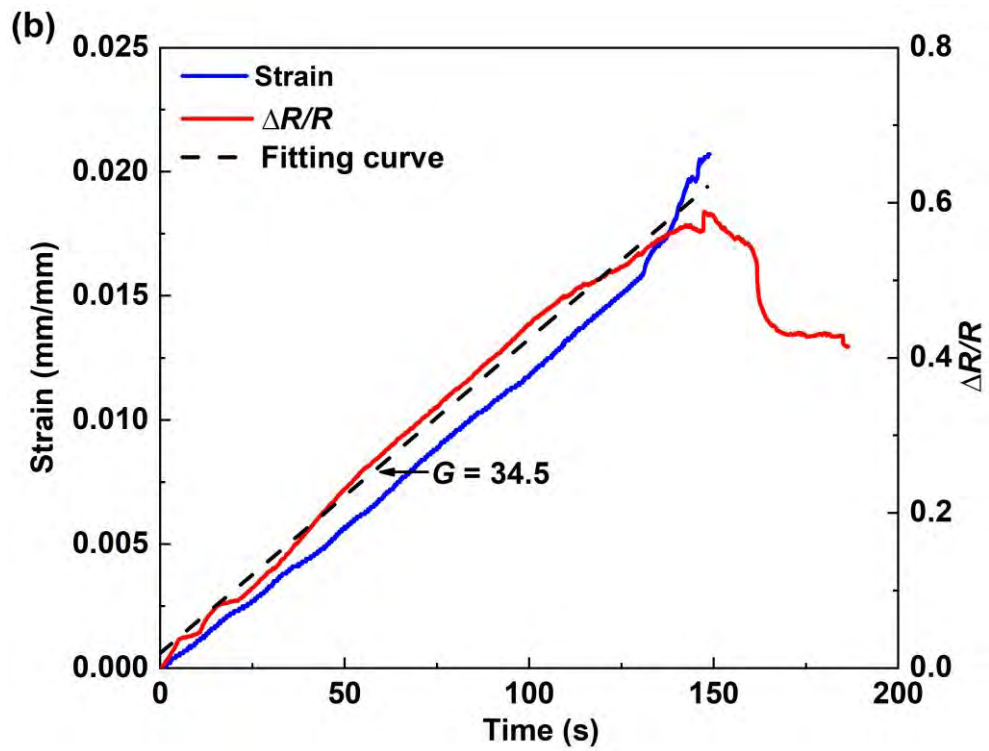
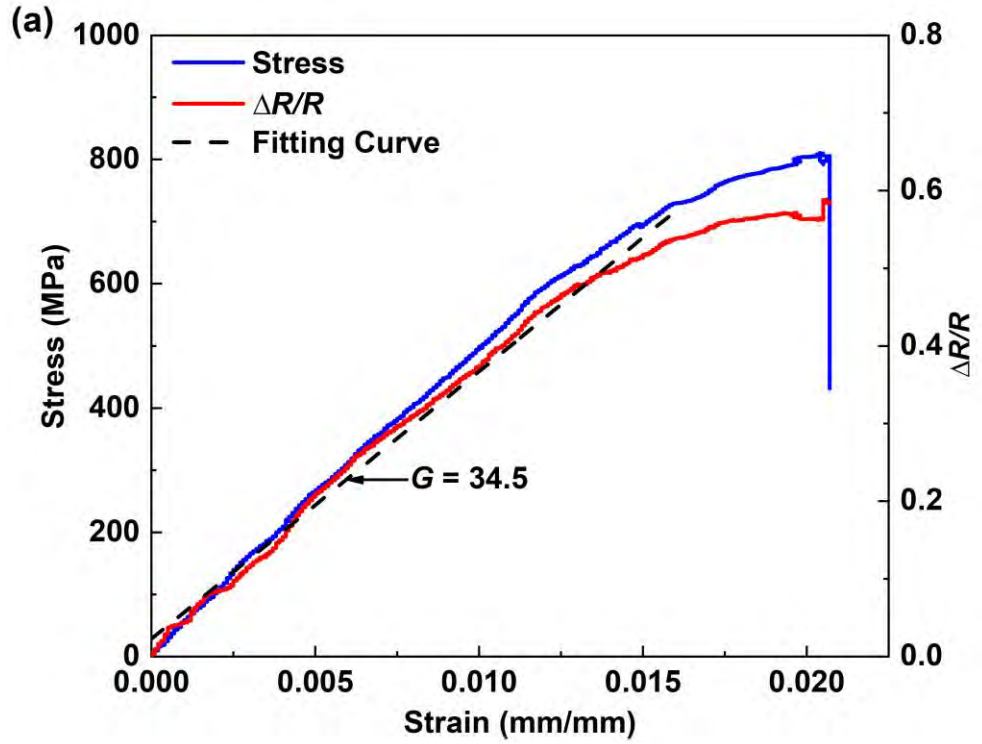


Figure 5.2 (a) Stress/ER changes vs. strain; and (b) strain/ER changes vs. time under a quasi-static tensile load.

The piezoresistive behavior of the nanocomposite sensors manifested under the static loadings can be interpreted using the sensing mechanism detailed in Section 4.2. When the strain is relatively large in magnitude (in the current case), the variation in contact resistance ($R_{Contact}$), due to the structural change in the GNP-formed conductive networks within the sensor, is dominant over the variations in tunnelling resistance ($R_{Tunnelling}$) and in intrinsic piezoresistivity of GNPs ($R_{Nanoparticle}$).

5.2.2 Medium-frequency Vibrations

The responsivity of a CFRP laminate with an implanted sensor to medium-frequency structural vibrations is investigated. An 8-ply quasi-isotropic CFRP laminate ($250 \times 25 \times 1.15 \text{ mm}^3$) with an implanted sensor is prepared, and one end of the laminate is clamped on a dynamic vibration test platform as a cantilever beam, as depicted in Figure 5.3. The sensor is implanted between the 1st and 2nd plies of the laminate, 150 mm from the clamped end. A standard strain gauge with a gauge resistance of 120Ω is surface-glued on the subface (the 1st ply) of the laminate for calibration. Continuous sinusoidal vibration signals in a sweeping frequency (from 100 to 1000 Hz) are generated with a waveform generator (HIOKI[®] 7075), to drive a vibration exciter (B&K[®] 4809) which is in contact with the bottom of the CFRP laminate, 35 mm from its free end. Both the implanted sensor and the surface-glued strain gauge are linked to a signal acquisition system which consists of a Wheatstone bridge (to

convert measured piezoresistive variations to electrical voltage signals), a signal conditioner (KYOWA[®] CDV-900A) and an oscilloscope (Agilent[®] DSO9064A).

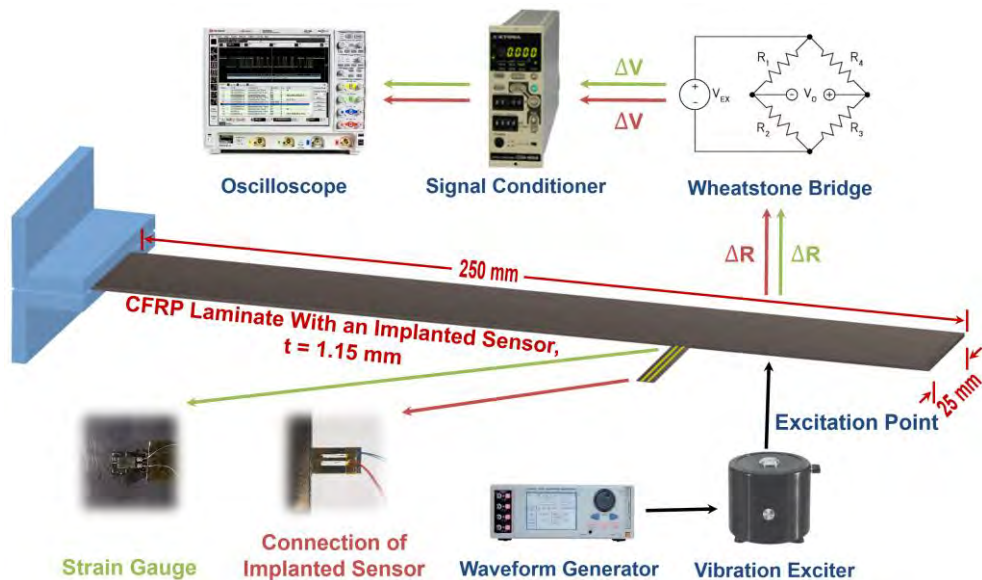


Figure 5.3 Schematic of set-up for acquiring dynamic responses in the vibration test.

Bandpass filters are applied to the captured raw signals for screening measurement noise. The processed signals obtained at three typical frequencies: 100, 500 and 1000 Hz, are compared in Figure 5.4. In Figures 5.4(a) and (b), waveform distortion and hysteresis are not observed between signals acquired by the implanted sensor and by the surface-glued strain gauge. To take a step further, signals captured by the nanocomposite sensor at 1000 Hz, under different degrees of excitation (4, 6, 8 and 10 V), are compared in Figure 5.4(c), to affirm a linear relationship between the response intensity of the sensor and the magnitude of excitation. Here, it is noteworthy that the nanocomposite sensors developed are a sort of piezoresistive

sensor, and therefore electrical voltage signals, rather than strain signals, are presented in Figure 5.4, showing the variation in piezoresistivity measured by the sensor.

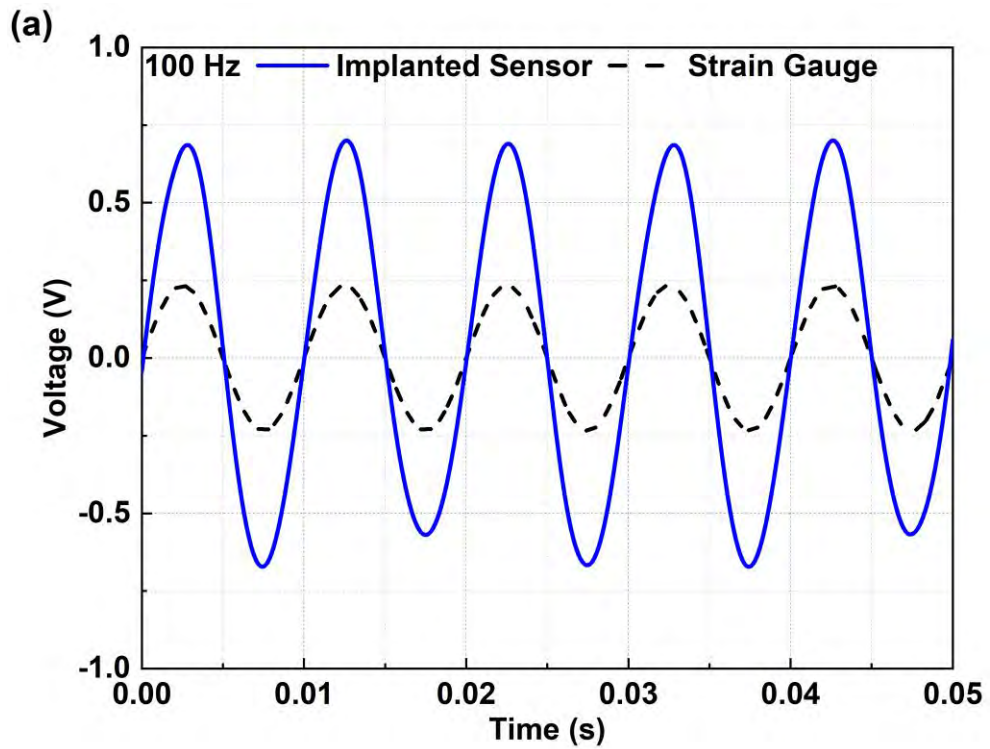


Figure 5.4 Responses of a CFRP laminate with an implanted sensor to vibrations at

(a) 100; (b) 500; and (c) 1000 Hz.

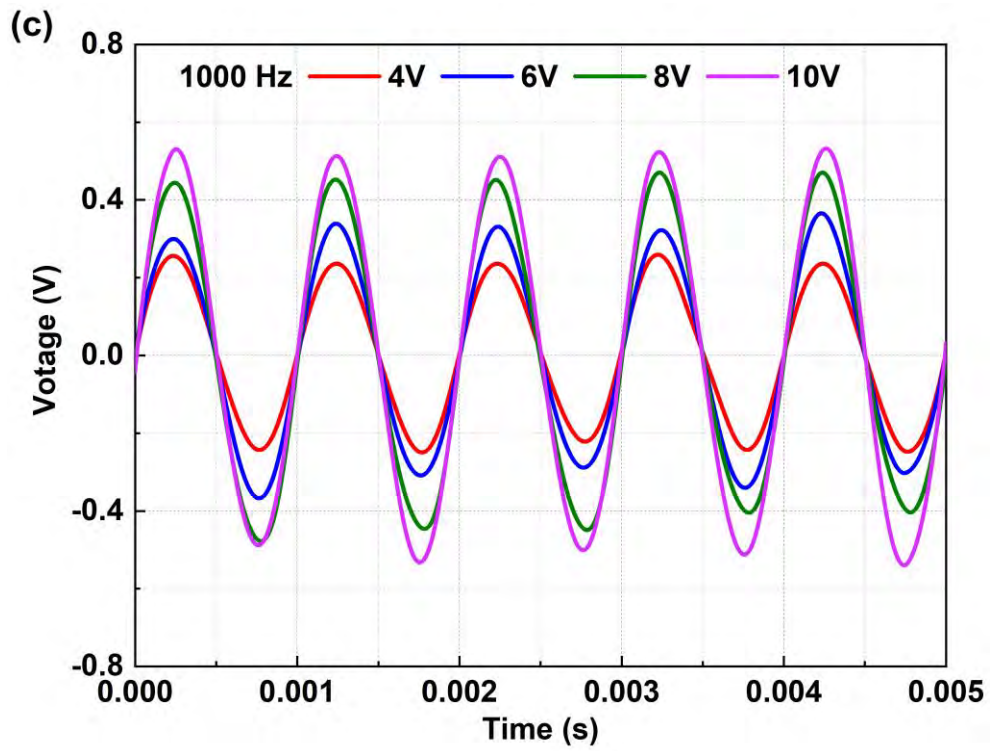
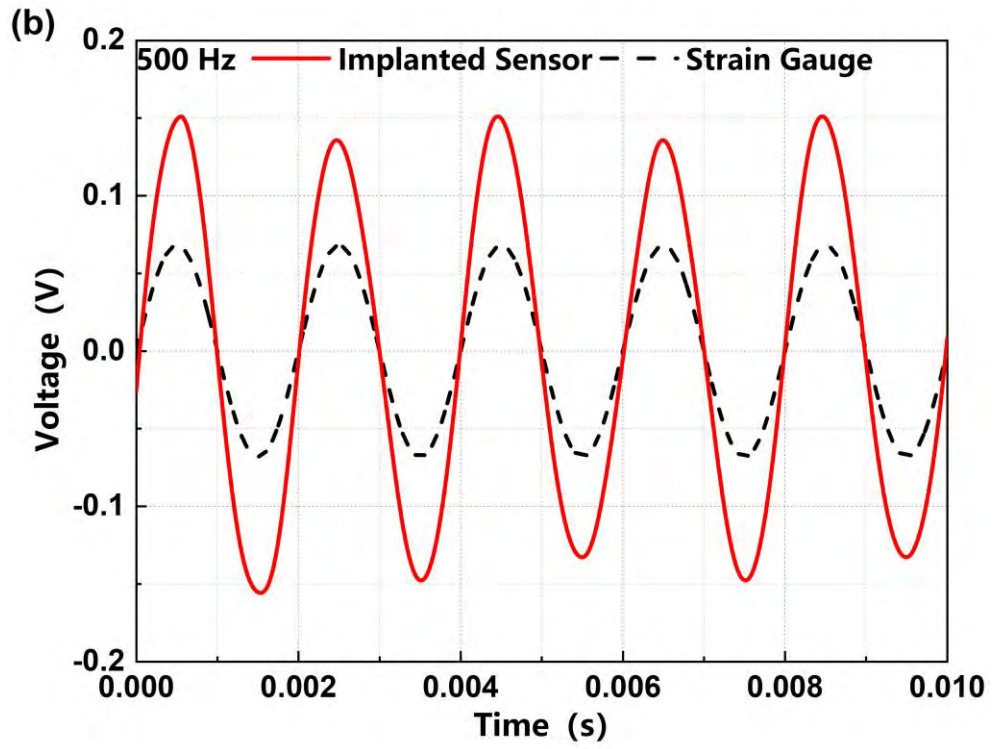


Figure 5.4 *Cont.*

5.2.3 High-frequency Guided Ultrasonic Waves

To interrogate the responsivity and accuracy of the CFRP laminate with implanted sensors to high-frequency GUWs, an ultrasonic measurement system is configured, shown schematically in Figure 5.5. An 8-ply quasi-isotropic CFRP laminate ($500 \times 500 \times 1.15 \text{ mm}^3$) which is implanted with a sensor network consisting of four nanocomposite sensors is prepared. The sensor network is implanted between the 4th and 5th plies, with each sensor being 100 mm from an edge, respectively. A miniaturized lead zirconate titanate (PZT) wafer (PSN-33; $\text{\O} = 12 \text{ mm}$; 1 mm thick) is also embedded between the 4th and 5th plies, alongside of an implanted sensor, which simultaneously perceives GUW signals for comparison. To emit a GUW into the laminate, a PZT wafer (PSN-33; $\text{\O} = 12 \text{ mm}$; 1 mm thick) is surface-mounted at the centre of the laminate. A 5-cycle Hanning-function-modulated sinusoidal toneburst is generated with a waveform generator (configured on a NI[®] PXIe-1071 platform) and applied on the surface-mounted PZT wafer after being amplified to $400 V_{p-p}$ via a linear power amplifier (Ciprian[®] US-TXP-3). The propagated GUW signals are perceived by all implanted sensors and the miniaturized PZT wafer. The nanocomposite sensors are connected to a self-developed signal amplification module consisting of a Wheatstone bridge, amplifiers and filters, and then the converted signals are recorded by an oscilloscope (Agilent[®] DSO9064A).

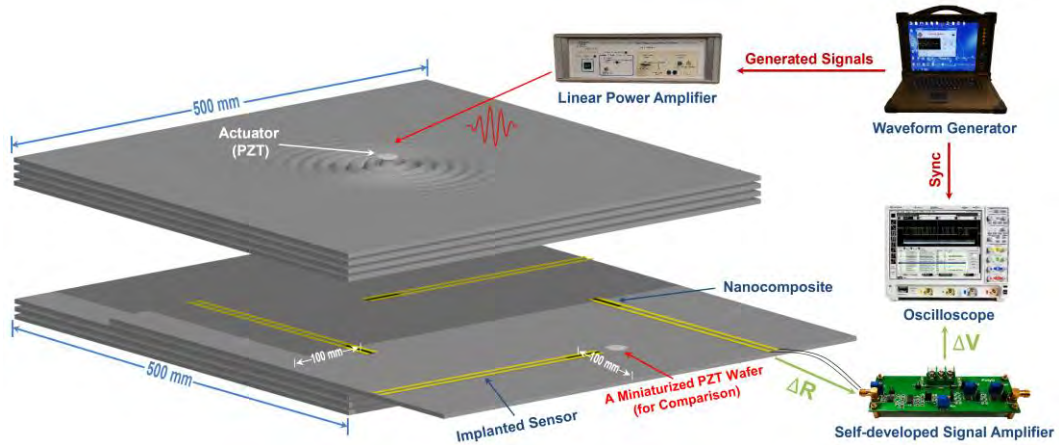


Figure 5.5 Schematic of set-up for acquiring GUV signals propagated in the laminate.

All captured signals are pre-averaged 1024 times to minimize measurement uncertainty and subsequently filtered with a first-order Butterworth filter to mitigate ambient noise. Figure 5.6 compares the signals captured by an implanted nanocomposite sensor that is randomly selected from the sensor network and by the PZT wafer, when a GUV is respectively activated at 200 and 450 kHz, as two examples, to observe good coincidence in the arrival time for all the wave modes, including the zeroth-order symmetric Lamb wave mode (denoted by S_0 in the figure), and the zeroth-order anti-symmetric Lamb wave mode (A_0). The discrepancy in signal magnitude is attributed to the different sensing mechanisms of these two types of sensors: the sensing philosophy of the nanocomposite sensors is based on piezoresistivity (tunnelling effect) as interpreted in Section 4.2, while the PZT wafer measures the change in piezoelectricity. The crosstalk observed in signals at the

excitation moment is generated by the linear power amplifier, which does not interfere with signal processing and interpretation.

Across a broad central frequency regime from 150 to 450 kHz (with a step of 25 kHz), all captured signals are pre-averaged 1024 times to minimize measurement uncertainty, filtered with a first-order Butterworth filter to mitigate ambient noise and consequently processed with a Hilbert transform. The Hilbert transform is an approach to canvass a signal in the time domain in terms of its energy distribution, and the envelope depicts the signal energy migration against time. Upon signal processing, signal spectra are obtained and shown in Figure 5.7, which demonstrate the comparable sensing performance between the implantable nanocomposite piezoresistive sensors and the conventional PZT wafer. Such a sensing capability enables GUV-based structural health monitoring for the host composite structure – a difficult task to be fulfilled using conventional nanocomposite piezoresistive sensors [51, 113, 121].

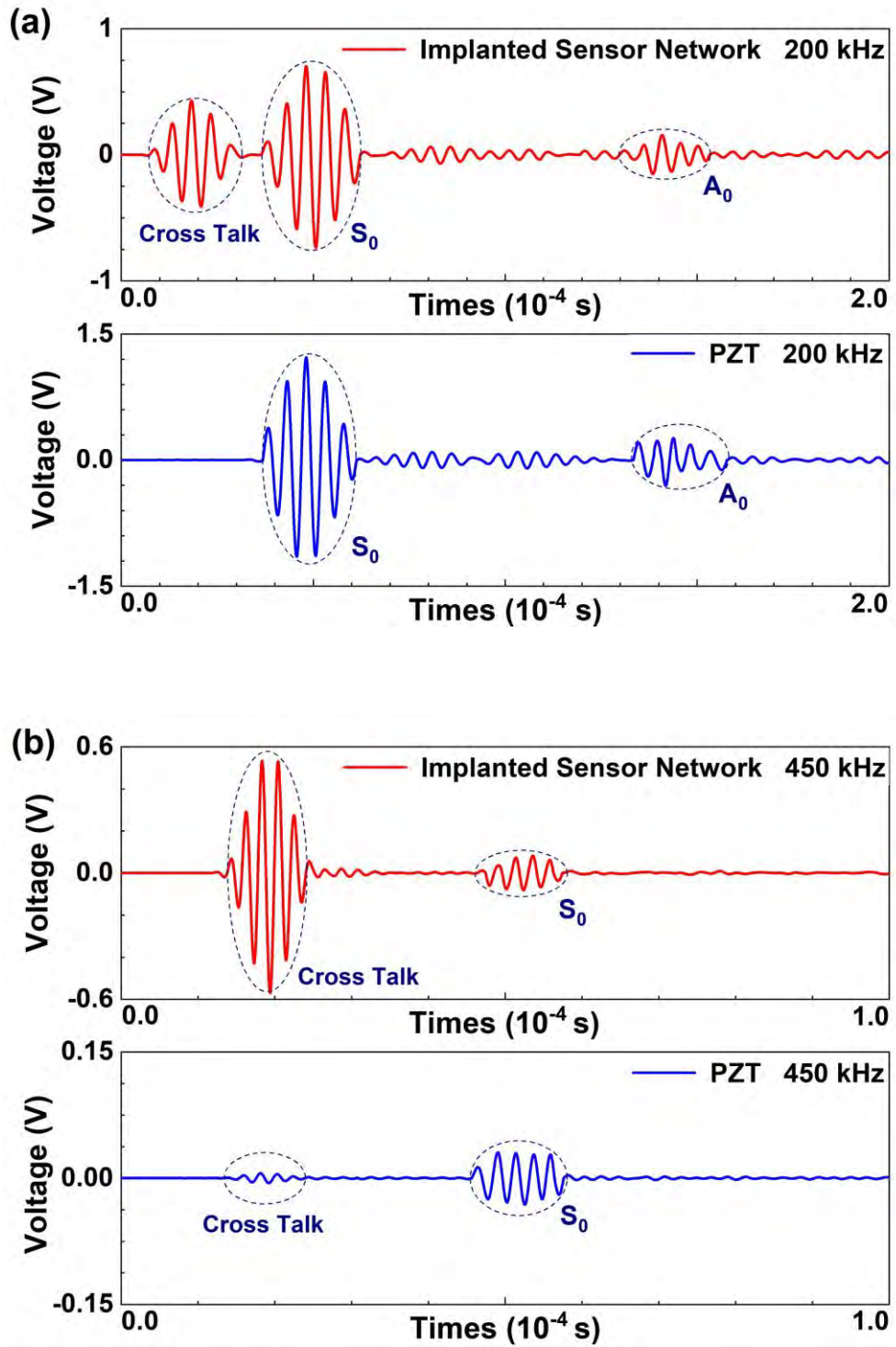


Figure 5.6 Signals captured by a nanocomposite sensor randomly selected from the implanted sensor network and by the PZT wafer, at (a) 200 kHz; and (b) 450 kHz.

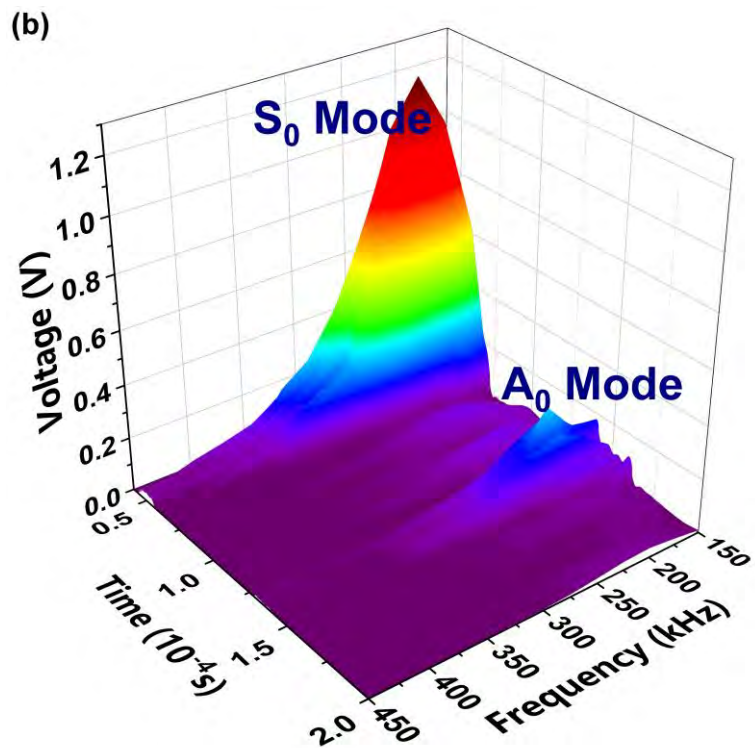
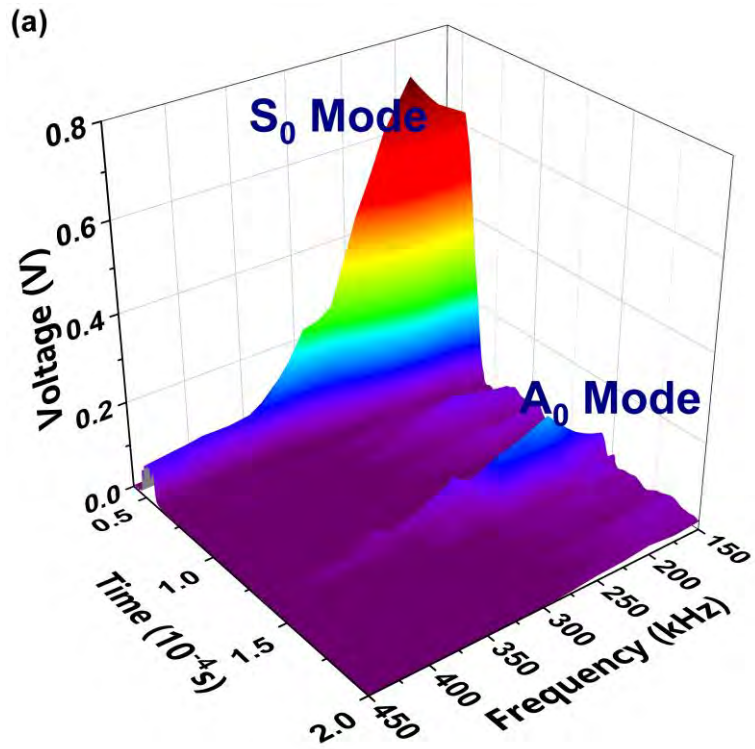


Figure 5.7 Spectra over time-frequency domain up to 450 kHz, perceived by (a) the nanocomposite sensor; and (b) the PZT wafer.

5.3 Possible Influence on Mechanical Properties of Composites

5.3.1 Tensile Properties

Quasi-static tensile test is performed to calibrate tensile properties of the laminates ($250 \times 25 \times 1.15 \text{ mm}^3$) and determine their failure modes, according to ASTM D3039. The two ends of each CFRP laminate are immobilized with an aluminum tab using an adhesive (Scotch-Weld[®] 2216) before tests, to avoid the premature failure near the gripping devices. In each laminate implanted with a sensor, the sensor ($250 \text{ mm} \times 3 \text{ mm} \times 45 \text{ }\mu\text{m}$) is centralized in the laminate and electrified via two CNT-film-made wires (1 mm wide and 10 μm thick each), as schematically illustrated in Figure 5.8. The sensor is positioned between the 4th and 5th plies of each laminate. All laminates are pulled apart on a universal testing system (INSTRON[®] 5982) with a crosshead speed of 2 mm/min until fracture, while the strain is simultaneously recorded by the AVE, Figure 5.9.

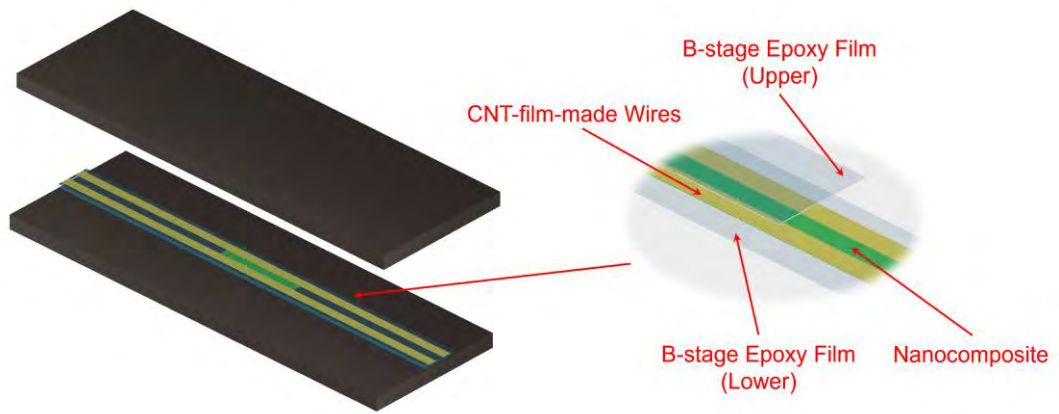


Figure 5.8 Schematic of a CFRP laminate implanted with a nanocomposite sensor (with two CNT-film-made wires) for tensile test.



Figure 5.9 The universal testing platform used in the tensile test.

Figure 5.10 displays the tensile test results of laminates with or without implanted sensors. In Figure 5.10(a), the obtained stress-strain curves argue that the sensor implantation does not incur observable degradation in elastic attributes of CFRP laminates, before reaching their ultimate tensile strength (UTS). Figure 5.10(b) compares the averaged UTS and Young's modulus of all laminates with or without sensor implantation, confirming no significant change in between. Only slight reductions of 2.65% and 1.85% in strength and stiffness, respectively, are observed, attributable to sensor intrusion. In addition, the neglectable degree of standard deviation in results proves good consistency in sample manufacturing.

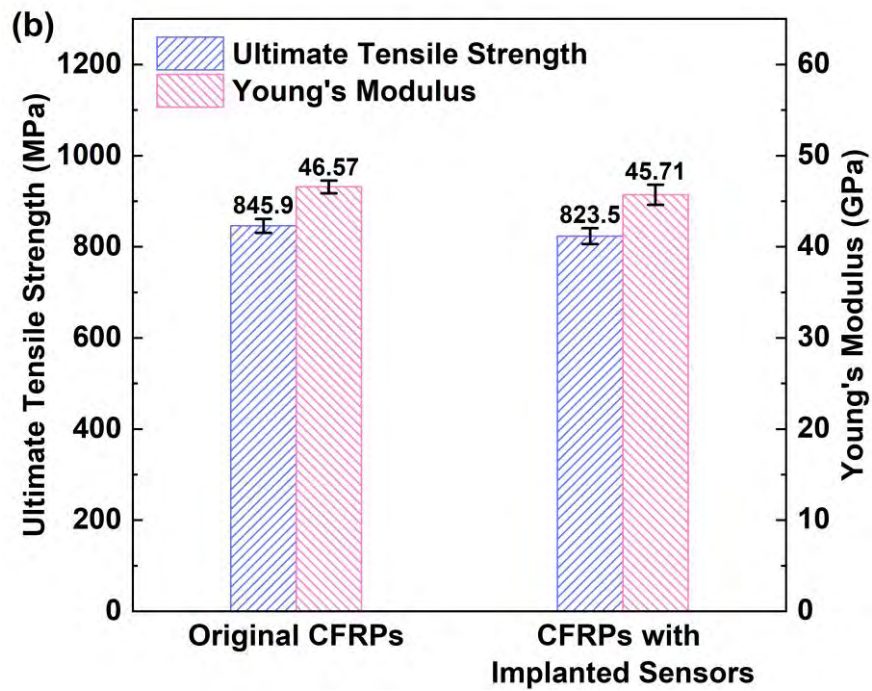
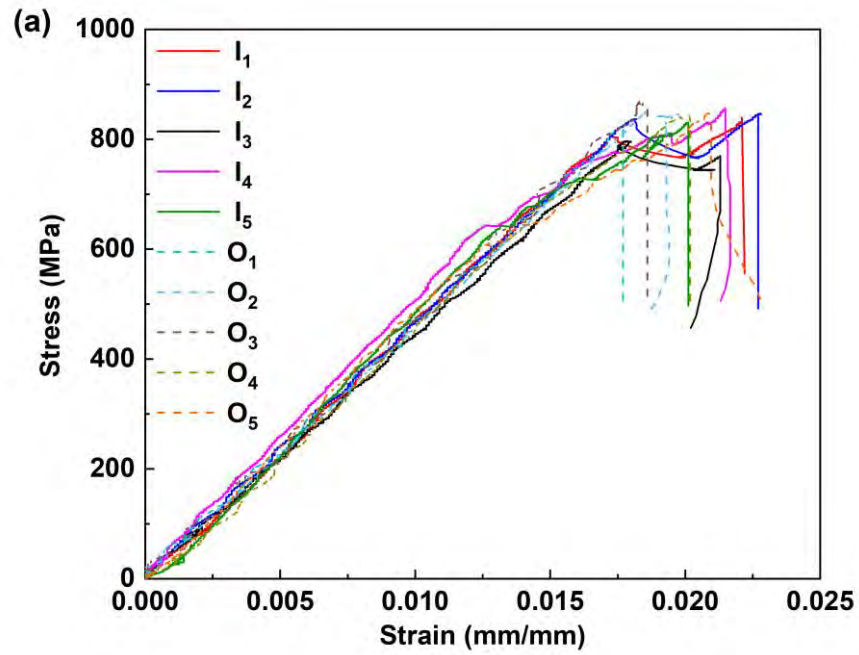


Figure 5.10 Results of tensile test: (a) stress-strain curves of CFRPs with or without implanted sensors (I_1 - I_5 : with implanted sensors; O_1 - O_5 : without any implanted sensor); and (b) averaged UTS and Young's modulus of laminates with or without sensor implantation.

The failure types of CFRP laminates with or without implanted sensors are identical, in a mixed mode of ply delamination and fibre breakage, as seen in Figure 5.11. It can be noted in Figures 5.11(a) and (b) that for a laminate with an implanted sensor, the main pathway, along which the delamination initiates and then progresses, is between the 5th (-45°) and 6th (+45°) plies – analogous to that for those counterpart laminates without sensor implantation as observed in Figure 5.11(c). In these figures, the fractured regions manifest the strong bonding between the carbon fibre (CF) prepreg and the implanted sensor, clarifying that the fracture of the laminate is due to the tensile stress, rather than material degradation at the interface between the implanted sensor and the prepreg.

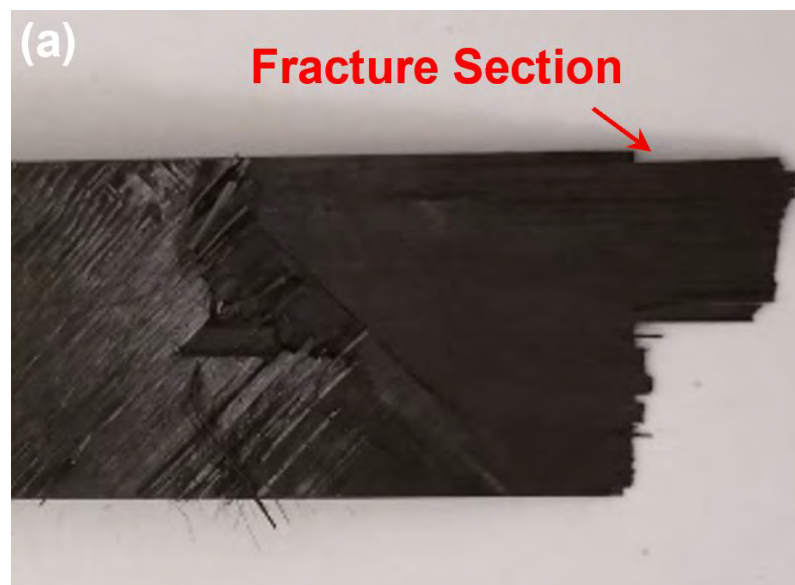


Figure 5.11 (a) A fractured laminate with an implanted sensor; (b) the fracture region in (a); and (c) the fracture region of a counterpart laminate without sensor implantation.

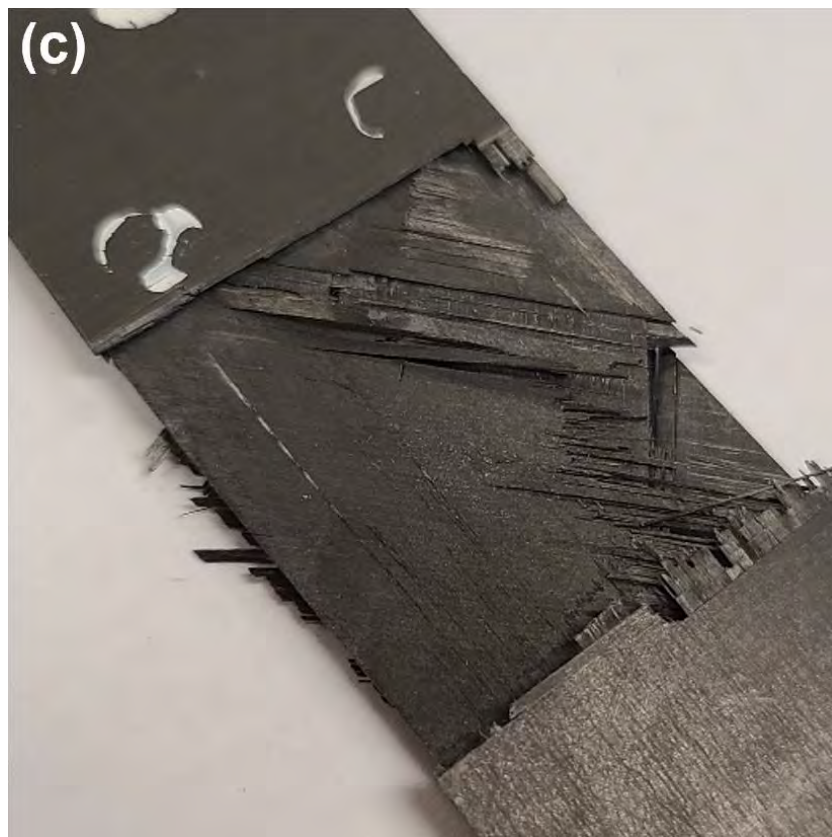
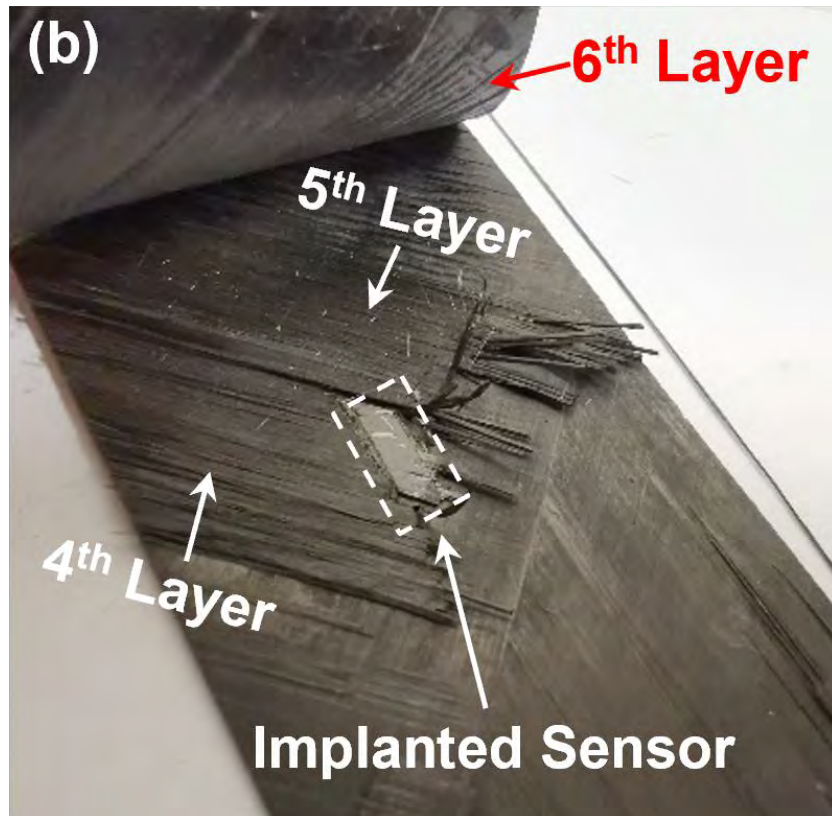


Figure 5.11 *Cont.*

5.3.2 Flexural Properties

Three-point bending test is conducted according to ASTM D790, to comparatively examine the flexural properties of CFRP laminates with or without implanted sensors. Each laminate measures $50.8 \times 12.7 \times 1.15 \text{ mm}^3$, with a support span of 25.4 mm. A sensor ($12.7 \text{ mm} \times 3 \text{ mm} \times 45 \text{ }\mu\text{m}$) with two CNT-film-made wires is implanted at the centre of each laminate between the 1st and 2nd plies, at which the maximum normal stress is expected under bending, in Figure 5.12.

The test is also conducted on the universal test platform (INSTRON[®] 5982) with a crosshead rate of 0.9 mm/min. The maximum normal stress at failure can be determined by Equation 5.1, while the flexural modulus is calculated using Equation 5.2, by measuring the slope in the linear region of the load-deflection curve, as

$$\sigma_f = \frac{3PL_s}{2bd^2}, \quad 5.1$$

$$E_B = \frac{L_s^3 m_s}{4bd^3}, \quad 5.2$$

where σ_f signifies the flexural strength (MPa), P the maximum load (N), L_s the support span (mm), b the width of the laminate (mm), d its depth (mm), E_B the modulus of elasticity in bending (MPa) and m_s the slope of the tangent to the initial straight-line portion of the load-deflection curve.

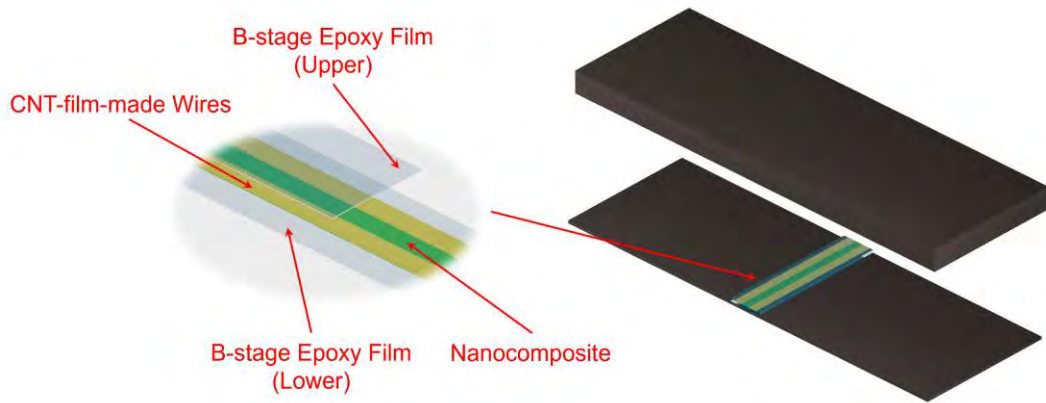


Figure 5.12 Schematic of a CFRP laminate implanted with a nanocomposite sensor (with two CNT-film-made wires) for bending test.

The obtained flexural properties of CFRP laminates with or without implanted sensors are compared in Figure 5.13, to observe the nonintrusive effect of an implanted sensor on the flexural properties of a CFRP laminate. The flexural strength of the laminate with an implanted sensor deviates from 916.6 to 950.9 MPa, while flexural modulus decreases marginally from 61.12 to 59.68 GPa. The slight variations in both flexural strength (+3.74%) and modulus (-2.36%) are attributed to the discrepancy in specimen preparation and tests. Figure 5.14 shows the fractured laminates under the flexural load, indicating that the failure mode is the compression fracture adjacent to the loading nose, irrespective of the implantation of a sensor. The implanted sensor does not initiate a defect, from which the failure develops, outperforming traditional PZT wafers which inevitably reduce the structural integrity to a certain extent [12, 13].

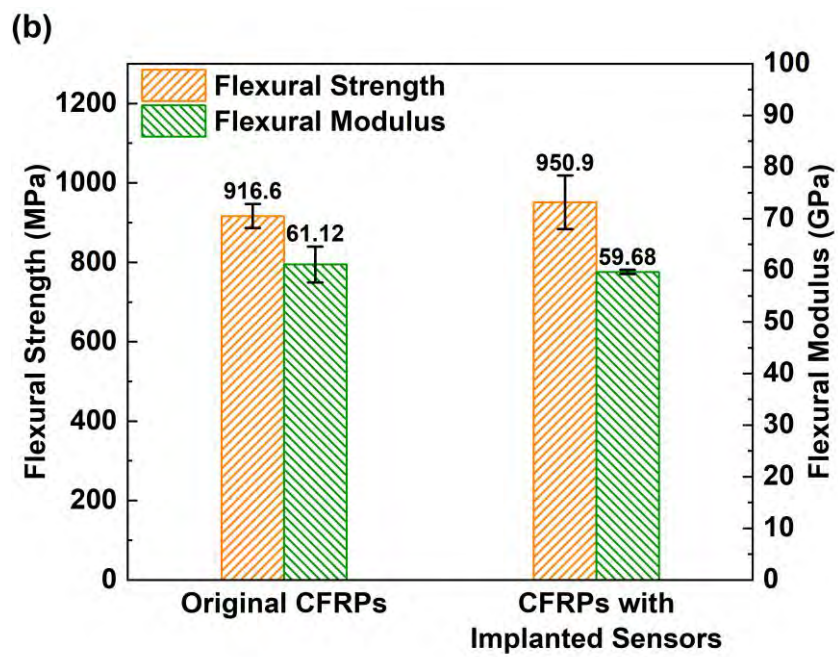
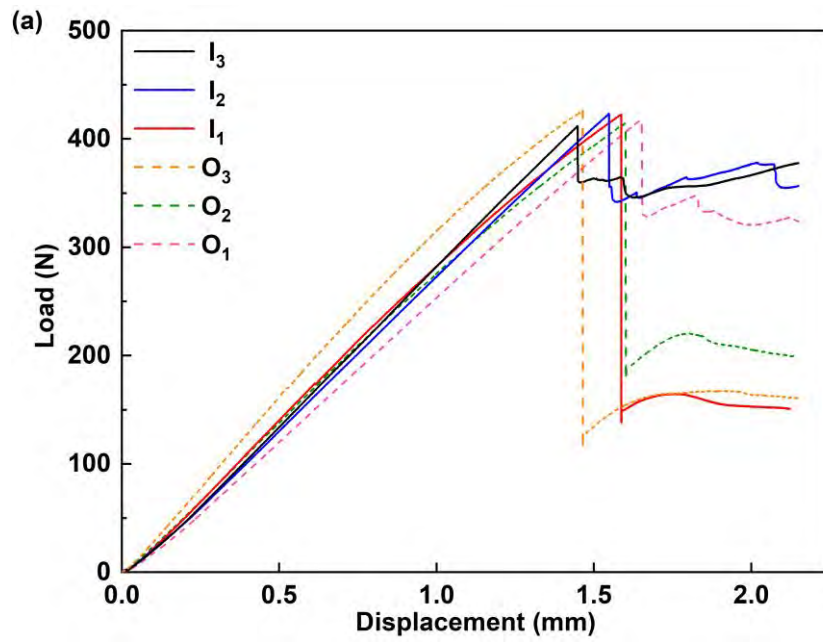


Figure 5.13 (a) Load-displacement curves; and (b) flexural properties of FRPs with and without implanted sensor (O_1 – O_3 : without implanted sensor; I_1 – I_3 : with implanted sensor).

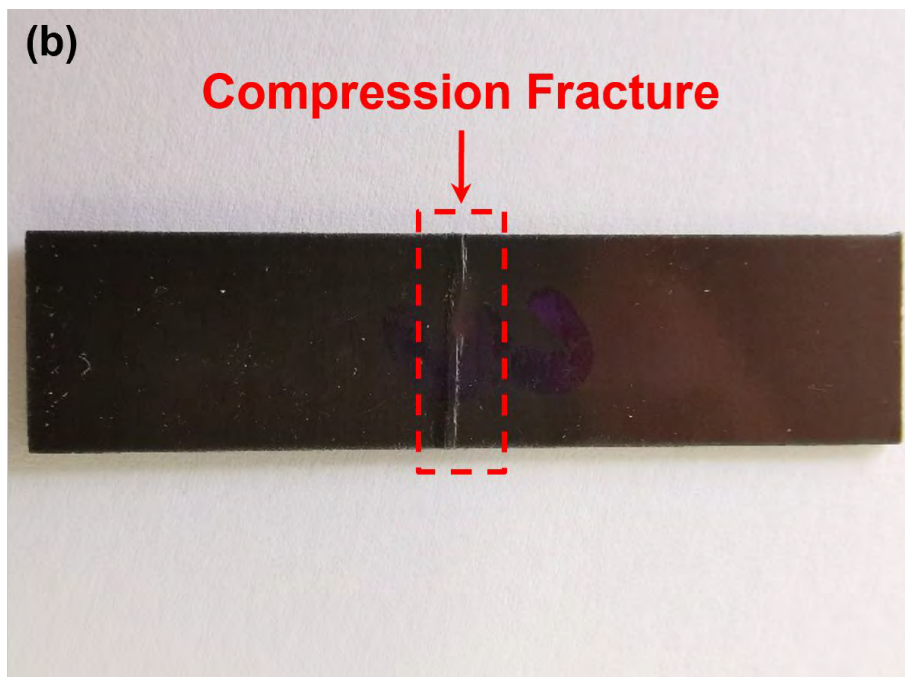
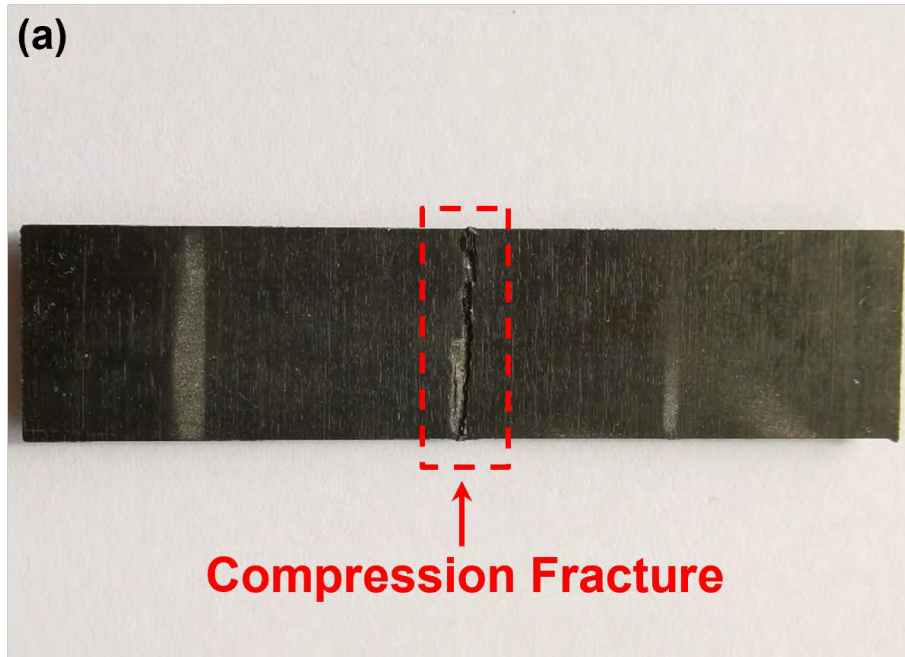


Figure 5.14 Fracture regions of (a) a counterpart laminate without the sensor; and (b) a laminate with an implanted sensor, with the zoomed-in fracture region in (c).

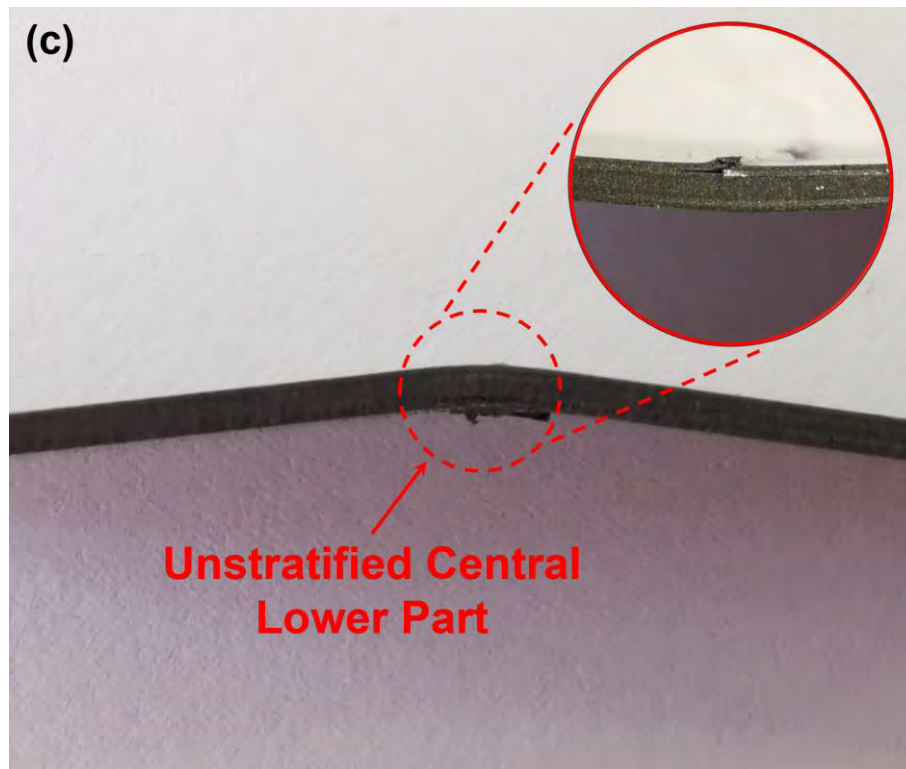


Figure 5.14 *Cont.*

5.4 Summary

After the rigorous fabrication, the sensing performance of CFRPs with implanted nanocomposite sensors is interrogated in a broad frequency regime, ranging from quasi-static tensile loads, through medium-frequency vibrations, to high-frequency ultrasonics. Specifically, the sensors demonstrate high sensitivity towards quasi-static tensile loads, with a high gauge factor of 34.5, much higher than that of a standard strain gauge (generally ~ 2.0). The implantable sensors also perform well in perceiving medium-frequency vibrations and demonstrate their responsivity to dynamic strains up to 450 kHz. The perceived GUV signals are of high accuracy and

fidelity, free of hysteresis and deviation. The acquired sensing performance is significant and promising, demonstrating their potential in both acousto-based passive or GUV-based active structural integrity monitoring (SIM). On top of that, tensile and flexural attributes of CFRPs with implanted nanocomposite sensors, acquired in tensile and bending tests conducted in accordance with ASTM standards, and detailed analysis on their failure modes demonstrate that the sensors inflict neglectable degradation in mechanical properties of the host composites.

CHAPTER 6

Continuous Monitoring of Composites with Implanted Nanocomposite Sensors: From Cure to In-service

6.1 Introduction

In lieu of conventional lead zirconate titanate (PZT) sensors adopted in acousto-ultrasonics-based monitoring approaches, in this chapter, a new continuous monitoring technique which evaluates the status of host composites, from manufacturing onset through service, is demonstrated using the above developed implantable nanocomposite sensors. Along with differential scanning calorimetry (DSC) and a Sesták–Berggren autocatalytic kinetic model, cure behaviors of fibre-reinforced polymer (FRP) composites in manufacturing are quantitatively estimated, in terms of the matrix polymerization degree that is correlated with variations in propagation attributes of guided ultrasonic waves (GUWs) captured by the implanted sensors. Use of the sensors is extended to structural integrity monitoring (SIM) of

FRPs that are in service. Experimental validation demonstrates that a transient impact to composites can be localized and imaged with the implanted sensors.

6.2 Process Monitoring

6.2.1 Cure Kinetics of Matrix

Material properties of FRPs (*e.g.*, stiffness and strength) are associated with the cure degree of matrix in a curing process [122]. On the other hand, propagation attributes of GUWs in FRPs are also dependent on material properties (*e.g.*, density and stiffness) and geometric features of FRPs [42]. Provided that the density and thickness of a FRP remain unchanged in a curing process [14, 30], the matrix cure degree can be correlated with the changes in propagation characteristics of GUWs.

To develop such a correlation, cure behaviors of FRPs are first investigated via DSC and a Sesták–Berggren autocatalytic kinetic model. Without loss of generality, a unidirectional E-glass epoxy prepreg (Guangwei Composites[®] G15000; thickness: 0.15 mm; fibre weight: 150 gsm; resin content: ~40 wt.%) is characterized with a differential scanning calorimeter (METTLER TOLEDO[®] DSC 3) in a nitrogen atmosphere (20 sccm) at the heating rates (β) of 1.0, 1.5, 2.0, 3.0 and 4.5 K/min, respectively, in a temperature range from 298.15 to 523.15 K. Prepreg sample (~2

mg) is sealed in an aluminum DSC pan and placed in the DSC chamber, along with another empty DSC pan that is heated simultaneously for benchmarking.

The DSC curves (*viz.*, heat flow vs. heating temperature) of the prepreg, representing the cure progress of matrix, obtained at representative heating rates, are compared in Figure 6.1, in which an exothermic peak is observed in each curve. As β increases, the exothermic peak shifts to a higher temperature range with a higher magnitude of exotherm, which is attributable to a higher increase rate of the temperature.

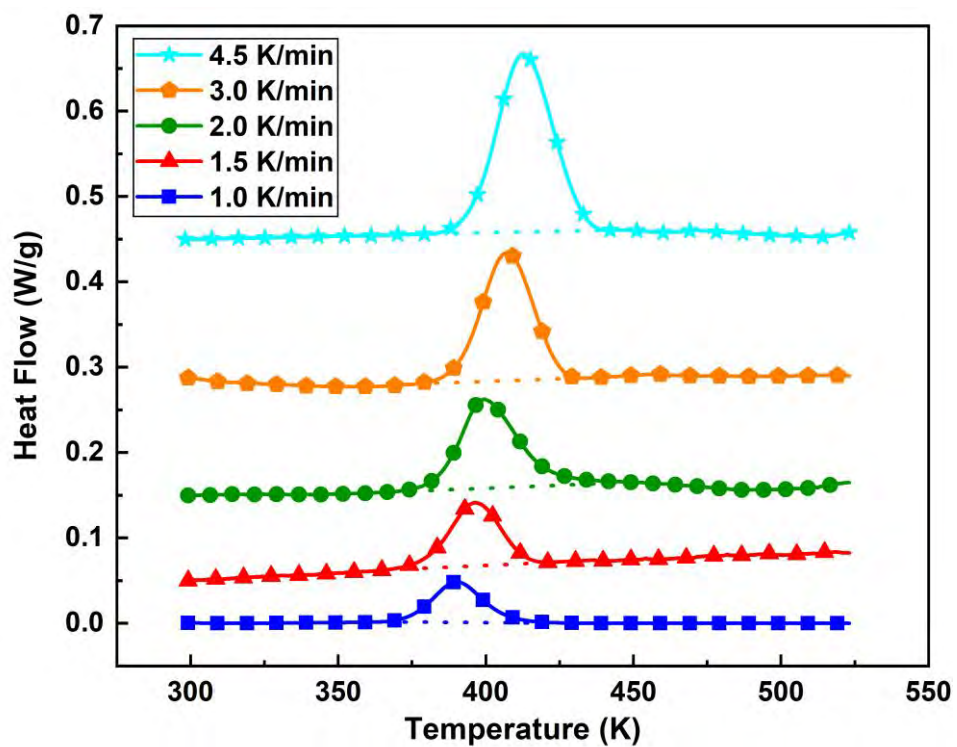


Figure 6.1 DSC curves of the prepreg at the heating rates of 1.0, 1.5, 2.0, 3.0 and 4.5 K/min, respectively.

With results in Figure 6.1, the cure degree, $\alpha(t)$, defined in Equation 4.3, is recalled.

The cure rate, $\frac{d\alpha(t)}{dt}$, can further be ascertained as

$$\frac{d\alpha(t)}{dt} = \frac{1}{H_T} \cdot \frac{dH(t)}{dt}. \quad 6.1$$

On the other hand, $\frac{d\alpha(t)}{dt}$ can also be correlated to the ambient temperature T through curing [31, 32] as

$$\frac{d\alpha(t)}{dt} = k(T) \cdot f(\alpha), \quad 6.2$$

where $k(T)$ denotes a temperature-dependent constant, and $f(\alpha)$ the function representing a kinetic model (to be detailed in the sequent). $k(T)$ can be expressed using an Arrhenius equation [33] as

$$k(T) = A \cdot e^{\frac{-E}{R_g T}}, \quad 6.3$$

where A represents a pre-exponential factor, E the apparent activation energy, and R_g the universal gas constant ($8.314 \text{ J} \cdot \text{mol}^{-1} \cdot \text{K}^{-1}$). Substituting Equations 6.3 into 6.2, the cure rate yields

$$\frac{d\alpha(t)}{dt} = A \cdot e^{\frac{-E}{R_g T}} f(\alpha). \quad 6.4$$

With the heating rate β ($\beta = \frac{dT}{dt}$), Equation 6.4 can be re-written as

$$\frac{d\alpha(t)}{dT} = \frac{A}{\beta} \cdot e^{\frac{-E}{R_g T}} f(\alpha). \quad 6.5$$

In the above, $\frac{d\alpha(t)}{dT}$ is referred to as the reaction rate in cure. To estimate E and A , the Kissinger method [33, 34] is recalled. The method assumes that the cure degree of

resin, regardless of β , remains the same when $\frac{d\alpha(t)}{dt}$ reaches its maximum, on which basis one has

$$\ln\left(\frac{\beta}{T_p^2}\right) = \ln\left(\frac{AR_g}{E}\right) - \frac{E}{R_g T_p}, \quad 6.6$$

where T_p is the temperature, at which $\frac{d\alpha(t)}{dt}$ reaches its maximum at a given β . Via plotting $\ln(\beta/T_p^2)$ versus $1/T_p$, calculating the slope of the linear fit and determining the y -intercept, the values of E and $\ln A$ are obtained as 86.26 kJ/mol and 24.87 $\ln(\text{min}^{-1})$, respectively, as shown in Figure 6.2(a).

With known E and $\ln A$, the Sesták–Berggren model [123-125] is applied, in conjunction with the obtained DSC results in Figure 6.1, to ascertain $f(\alpha)$. With the Sesták–Berggren model, $f(\alpha)$ is approximated by

$$f(\alpha) = \alpha(t)^m (1 - \alpha(t))^n, \quad 6.7$$

where m and n are two unknown variables to be determined. Substituting Equations 6.7 into 6.4 and taking the logarithm of the equation, it yields

$$\ln\left(\frac{d\alpha(t)}{dt} e^{\frac{E}{R_g T}}\right) = n \cdot \ln[\alpha(t)^p (1 - \alpha(t))] + \ln A, \quad 6.8$$

where $p = \frac{m}{n}$. On the other hand, introducing $\alpha(t)_M$ which represents the cure degree, at which $\frac{d\alpha(t)}{dt} e^{\frac{E}{R_g T}}$ reaches its maxima at a given β (as indicated in Figure

6.2(b)), p can be calculated via

$$p = \frac{\alpha(t)_M}{1 - \alpha(t)_M}. \quad 6.9$$

In Figure 6.2(b), it can be seen that for all β of investigation, $\alpha(t)_M$ remains a constant of ~ 0.3 , and p is therefore ~ 0.43 . With it, n and m are calculated via Equation 6.8, in Table 6.1. With all parameters in Table 6.1, the correlation between $\frac{d\alpha(t)}{dt}$ and the cure temperature, and the correlation between $\alpha(t)$ and the cure temperature are fitted with the Sesták–Berggren model, shown in Figure 6.3. These two correlations can be extended to calculate the cure rate ($\frac{d\alpha(t)}{dt}$) and the cure degree ($\alpha(t)$) against the cure temperature, at a given heating rate (β).

On the other hand, different cure degrees of matrix modulate propagation characteristics of GUWs in FRPs distinctly. Facilitated by the correlations in Figure 6.3, $\alpha(t)$ can thus be linked to the group velocity (C_g) of GUWs, by taking into account different heating rates (β). With measured C_g , the cure degree can be evaluated (in Section 6.2.2).

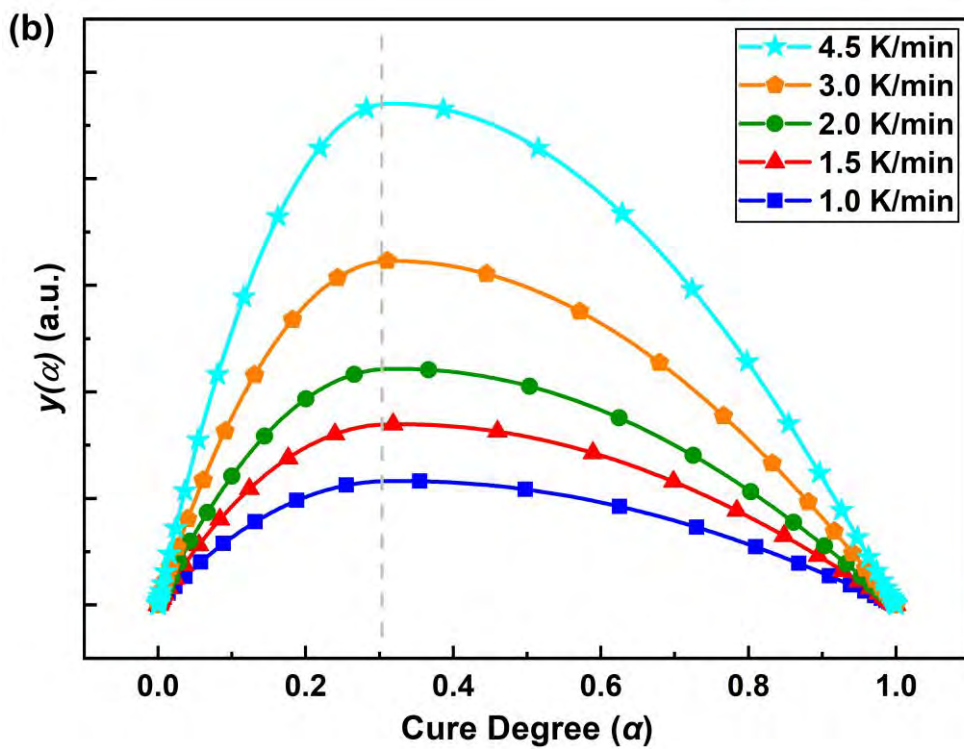
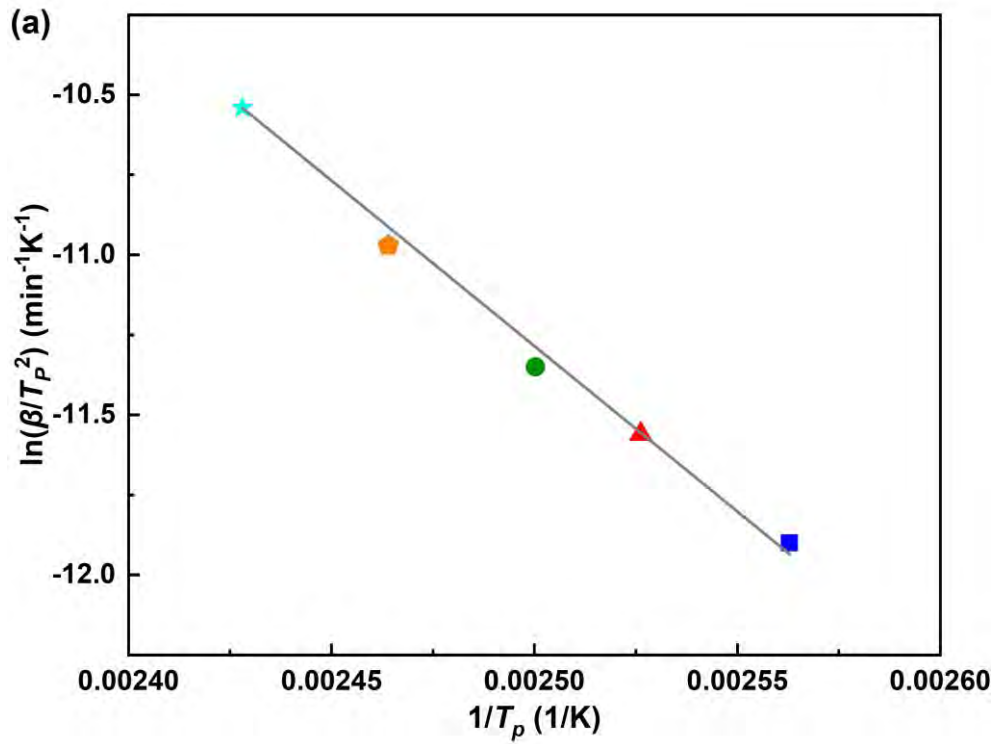


Figure 6.2 (a) Kissinger plot for determining E and $\ln A$; and (b) plot of

$$y(\alpha) = \frac{d\alpha(t)}{dt} e^{\frac{E}{RT}} \text{ versus cure degree } (\alpha(t)) \text{ at different } \beta.$$

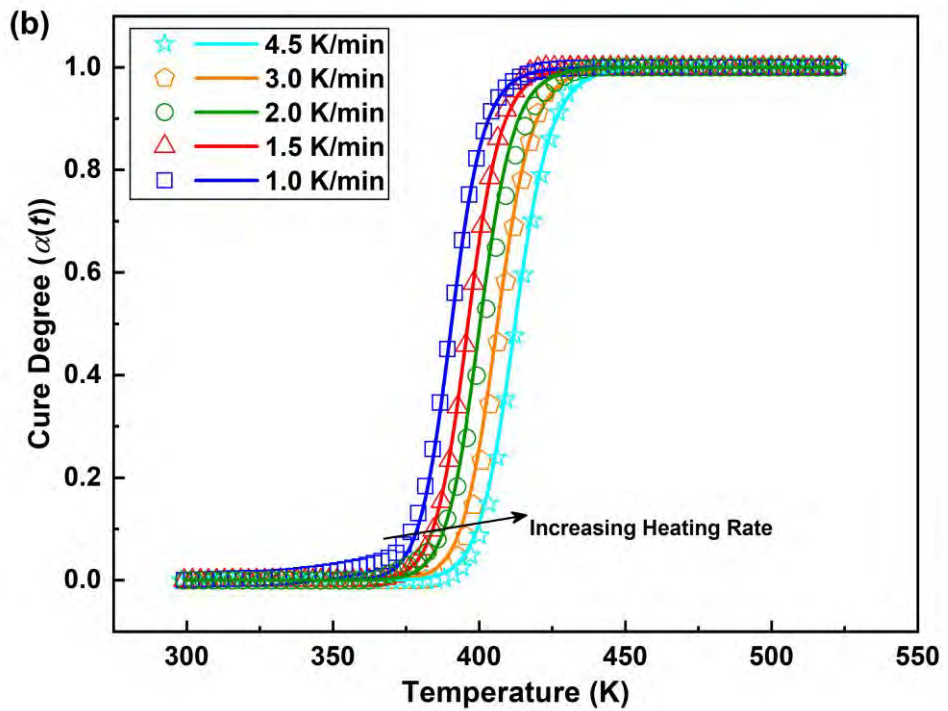
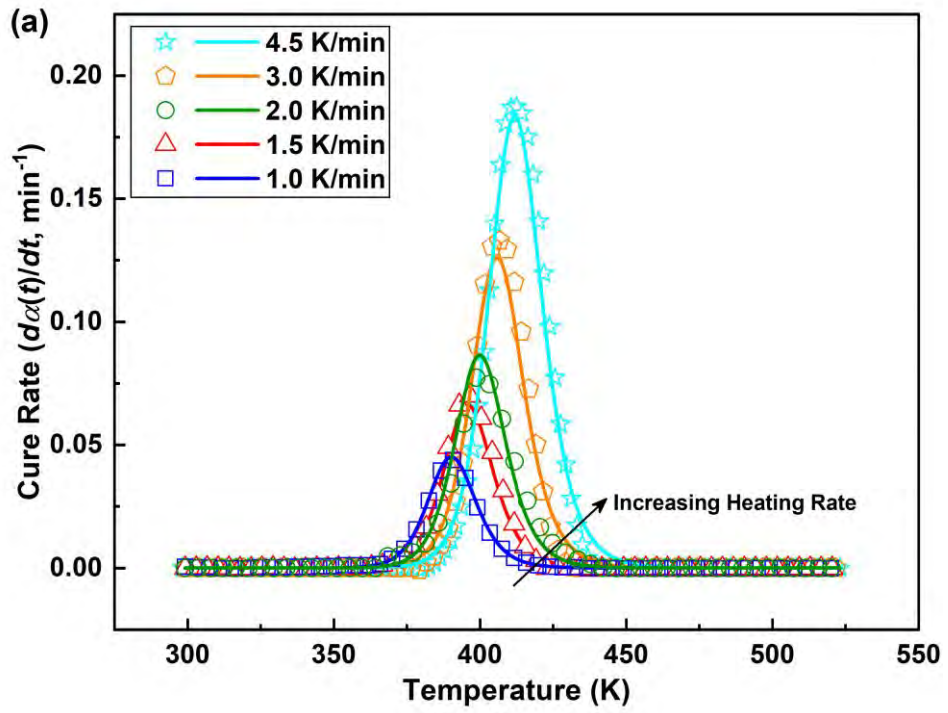


Figure 6.3 (a) Cure rate ($\frac{d\alpha(t)}{dt}$) versus cure temperature; and (b) cure degree ($\alpha(t)$)

versus cure temperature at different β (solid line: Sesták–Berggren model-predicted results; symbol: experimental results).

Table 6.1 Determined parameters in Sesták–Berggren autocatalytic kinetic model.

E [kJ/mol]	$\ln A$ [ln(min ⁻¹)]	m	n
86.26	24.87	0.60	1.43

6.2.2 Guided Ultrasonic Wave-based Cure Monitoring

With the Sesták–Berggren model, the matrix cure degree ($\alpha(t)$) is correlated with the group velocity (C_g) of GUWs perceived by the implanted sensors, to monitor cure progress of FRPs in a real-time and *in situ* manner.

Methodology

Eight plies of unidirectional E-glass epoxy prepregs are stacked to produce an 8-layer quasi-isotropic $[0^\circ/90^\circ/45^\circ/-45^\circ]_s$ FRP laminate ($500 \times 500 \times 1.15$ mm³). A group of eight nanocomposite sensors is implanted between the 4th and 5th prepregs, to configure a sparse sensor network via CNT-film-made wires. The sensor network is instrumented with a self-developed signal generation and acquisition system, as illustrated schematically in Figure 6.4 and described in Section 5.2.3. Two ETFE peel films (AIRTECH[®] WL5200B), 15 μ m thick each, are placed atop and beneath the stacked prepregs. The stacked prepregs that are sandwiched by the peel films are placed on an aluminum tooling plate covered with a layer of thick breather. A miniaturized PZT wafer (PSN-33; \varnothing : 12 mm; 1 mm thick) is surface-placed at the

centre of the upper peel film for GUW generation, which is 150 mm from each of the eight nanocomposite sensors. Under the vacuum pressure of -25 inHg, a good acoustic coupling is achieved between the PZT wafer and prepregs, warranting efficient generation and transmission of GUWs. After adding another thick breather layer on the upper peel film, the prepregs undergo a standard vacuuming process. Upon vacuuming, prepregs are heated from 298.15 to 458.15 K until the laminate is fully cured.

A 5-cycle Hanning-function-modulated sinusoidal toneburst is generated at a frequency of 175 kHz every ten microseconds, using a waveform generator on NI[®] PXIe-1071 platform. The generated signal is applied on the PZT wafer, after it is amplified to 400 V_{p-p} via a linear power amplifier (Ciprian[®] US-TXP-3). Propagation of the generated GUWs in prepregs during the cure progress is perceived with the implanted sensors and recorded with an oscilloscope (Agilent[®] DSO9064A), as shown in Figure 6.4.

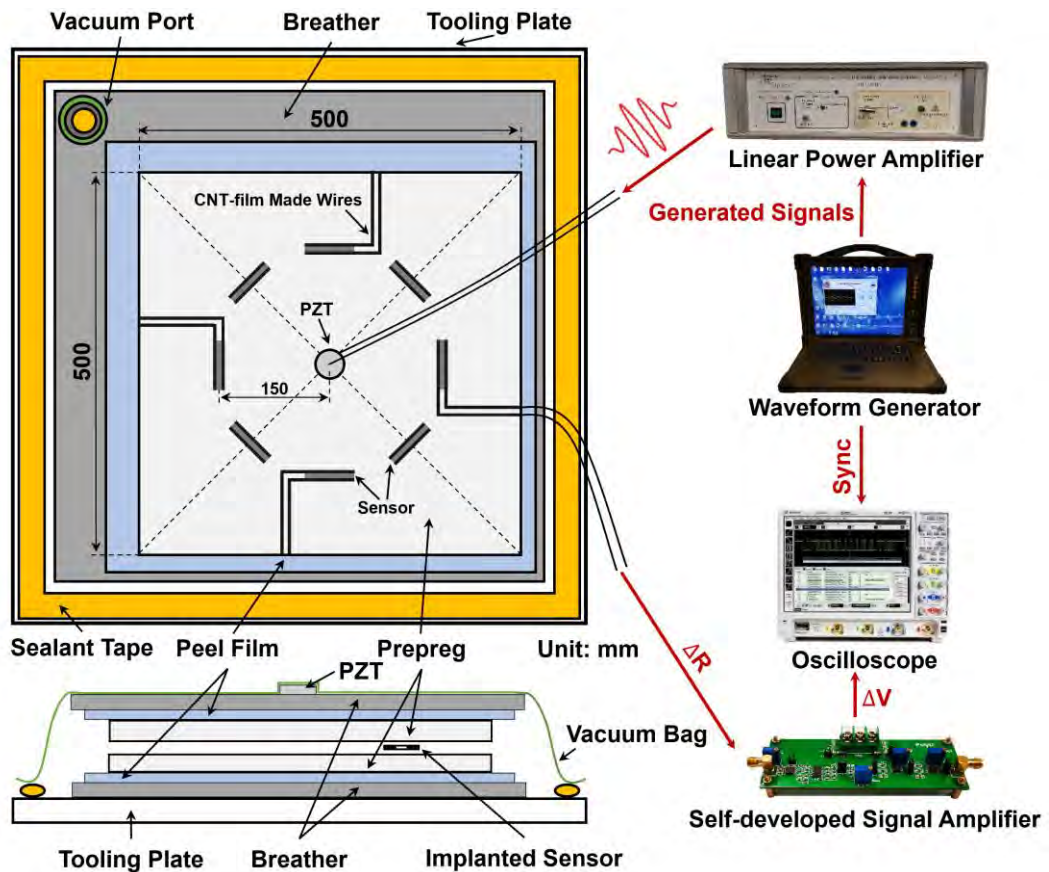


Figure 6.4 Experimental set-up for GUV-based cure monitoring.

Results

All GUV signals recorded as cure progresses are applied with a first-order Butterworth filter to mitigate ambient noise and measurement uncertainties. Figure 6.5 shows representative GUV signals captured by an implanted sensor, along with the energy envelopes of signals obtained via Hilbert transform, at different temperatures with the heating rate of 1.5 K/min. It can be seen in Figure 6.5 that both the group velocity of GUVs and signal magnitudes change remarkably against temperature through curing.

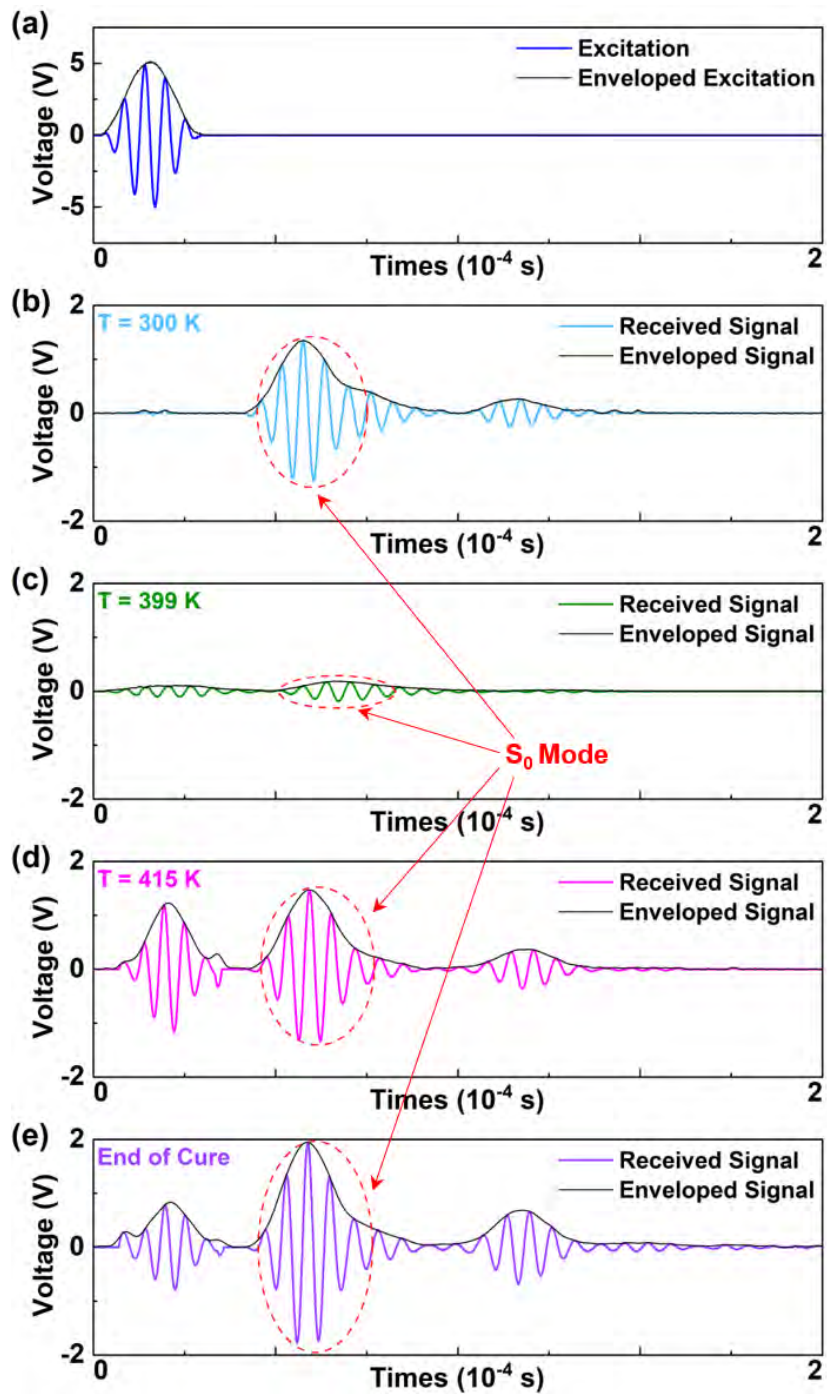


Figure 6.5 Representative G UW signals captured by an implanted sensor, along with wave energy envelopes, at different temperatures with the heating rate of 1.5 K/min.

The group velocity of the zeroth-order symmetric Lamb wave mode is extracted from signals, with which the cure progress of matrix is real-time monitored

according to the Sesták–Berggren model. C_g is calculated in virtue of the time at which the signal energy envelope reaches its peak, as

$$C_g = \frac{L}{t_s - t_e}, \quad 6.10$$

where L (150 mm) is the distance between the PZT wafer and a nanocomposite sensor. t_e and t_s signify the moments, at which the energy envelope reaches its peak, respectively for the excitation signal and for the sensor-received signal.

A batch of the above-detailed 8-layer prepregs, each with the implanted nanocomposite sensor network and a surface-placed PZT wafer, are prepared. As representative results, the progressive alteration in C_g of the S_0 wave mode, measured at two different heating rates, namely 1.0 and 1.5 K/min, are displayed in Figure 6.6. The S_0 wave mode is measurable at the beginning of cure. As observed, C_g of the S_0 wave mode decreases, as the cure temperature elevates, until wave signals can no longer be identified due to the fact that the matrix becomes an attenuative, viscous liquid; as cure continues, the S_0 wave mode is measurable again from ~ 393 K for the heating rate of 1.0 K/min and from ~ 399 K for 1.5 K/min, at which the corresponding cure degrees are 0.620 (for 1.0 K/min) and 0.625 (for 1.5 K/min), as predicted by the Sesták–Berggren model. These results are consistent with the cure degree at the gel point of the matrix (~ 0.6) as provided by the manufacturer. As depicted in Figure 6.6, after the gel point of matrix, the C_g of GUWs increases rapidly, as a result of a higher crosslinking density of the resin. The increase rate of

C_g decreases after the matrix begins its vitrification and subsequently remains slight change which indicates the completion of cure.

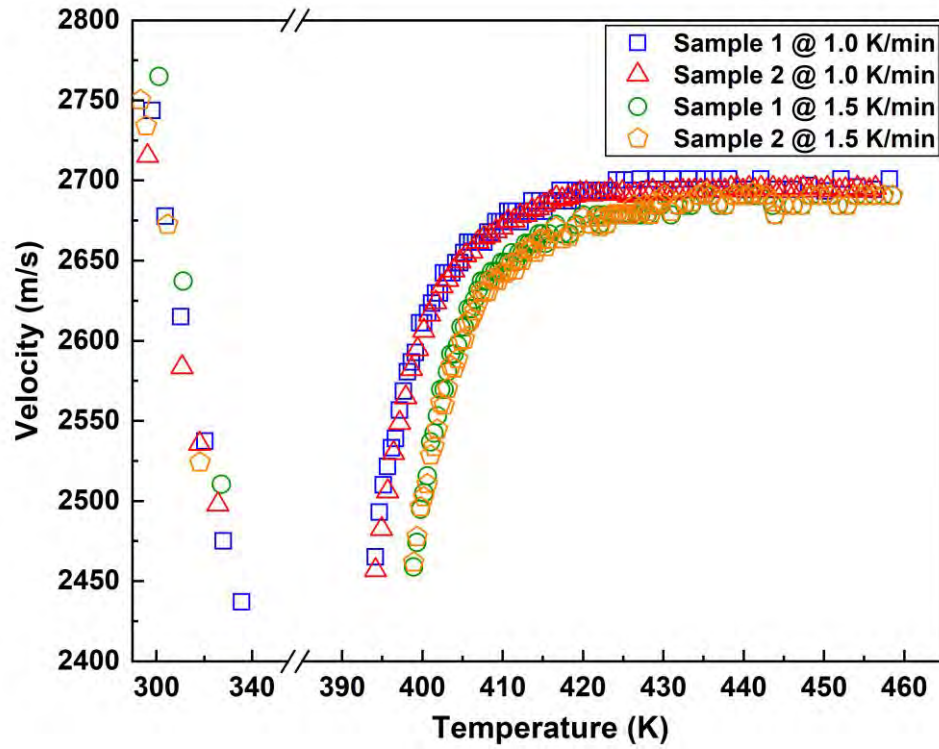


Figure 6.6 Group velocity of S_0 wave mode at different cure temperatures, corresponding to different cure degrees.

The alteration in C_g of the S_0 wave mode is quantitatively associated with the change in the stiffness of the matrix which reflects the cure degree, as shown in Figure 6.7. In Figure 6.7(a), good consistence among all experimentally measured C_g is noted when the cure degree of matrix is at the same degree, irrespective of different heating rates. With Figure 6.7(a), the correlation between the cure degree of matrix and C_g of the S_0 wave mode is fitted as

$$C_g = 1035 \int_{0.625}^{\alpha} \alpha^{0.39} (1-\alpha)^{0.26} d\alpha + 2460, \quad 6.11$$

as shown in Figure 6.7(b). With such a correlation, cure information of composites after the gel point of matrix can be monitored in a real-time manner with the pre-implanted nanocomposite sensors, to quantify the cure degree of matrix and indicate the completion of resin cure.

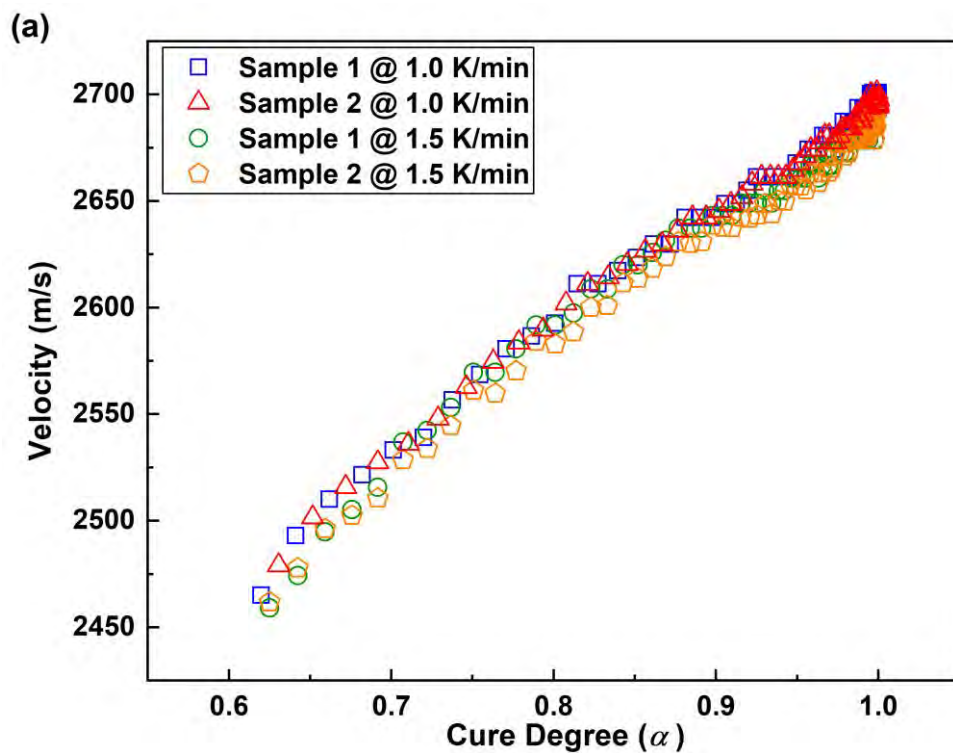


Figure 6.7 (a) Measured C_g of GUWs *versus* cure degree of matrix; and (b)

Equation 6.11-predicted correlation between cure degree of matrix and C_g of S_0 wave mode, compared with experimental results.

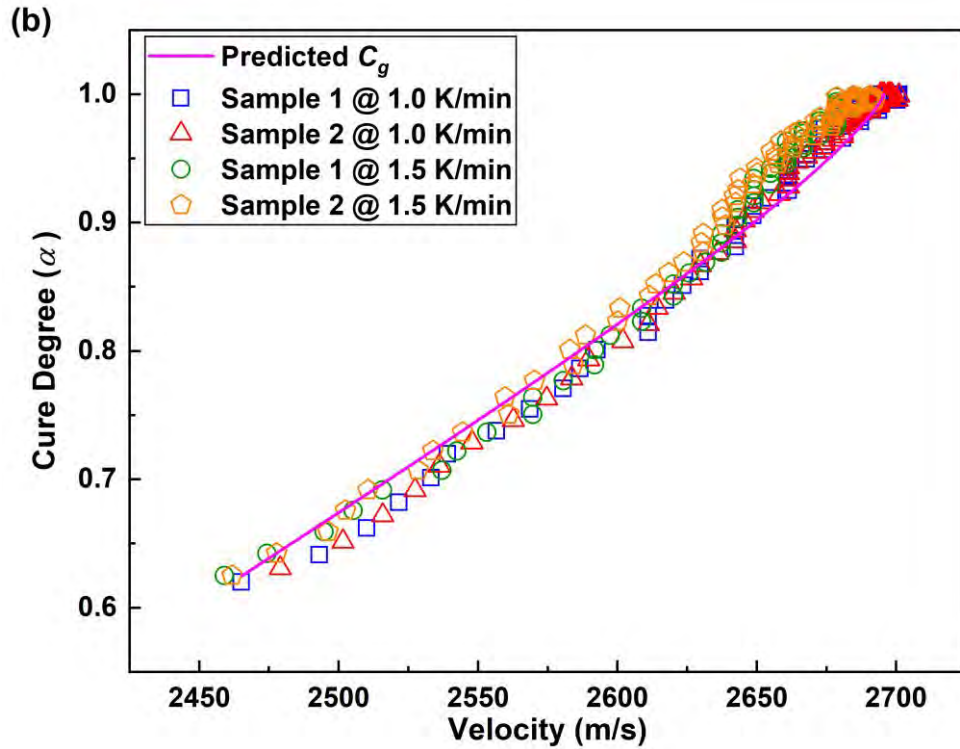


Figure 6.7 Cont.

Cure Anomaly Detection

With the Sesták–Berggren model and acquired relationship between the group velocity of GUWs and cure degree of matrix in Equation 6.11, the cure progress of another two sets of 8-layer prepregs with implanted sensors is monitored at the heating rate of 2.0 K/min. To introduce a mock-up anomaly in a curing process, a heating tape (measuring $15 \times 3 \text{ cm}^2$) is adhered at the back surface of the tooling plate for one of the two sets. The tape is located along the GUW propagation path that is linked by the PZT wafer and nanocomposite sensor I, indicated in Figure 6.8.

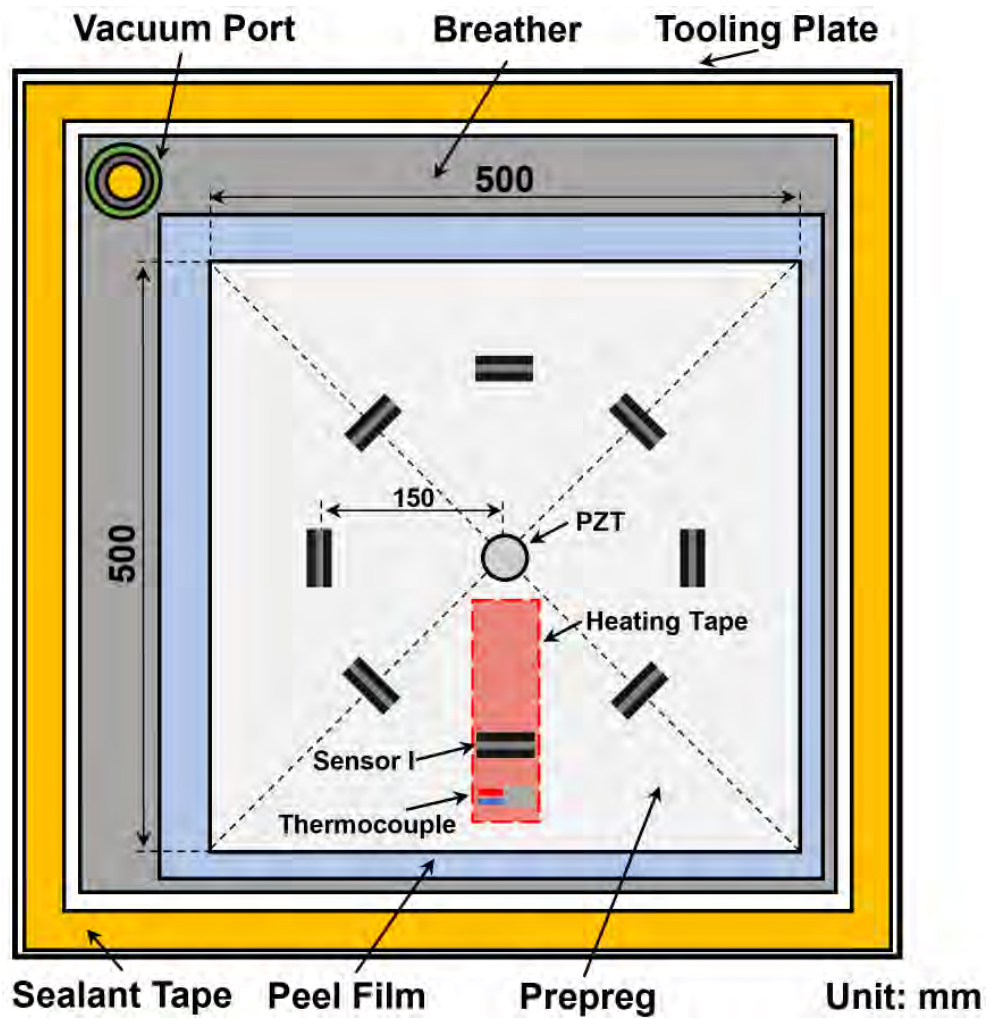


Figure 6.8 Schematic of the prepress cured with a heating anomaly.

As shown in Figure 6.9(a), the experimentally measured C_g from the normal heating area is consistent with the predicted C_g which is obtained via the combination of the Sesták–Berggren model in Section 6.2.1 and acquired relationship between the group velocity of GUWs and cure degree of matrix via Equation 6.11.

On the other hand, the heating tape quickly elevates the temperature of the matrix in its vicinity at a higher heating rate, as measured by a thermocouple collocated

alongside the tape to real-time record the temperature change in such an abnormal heating area, Figure 6.9(b). As this abnormal area is heated to and maintained at a higher temperature more quickly, compared with the normal area, the matrix at this abnormal area reaches its gel point (at which time GUWs can be measured again in a curing process) and finishes the cure progress (at which time the group velocity of GUWs reaches and maintains at its plateau) earlier, in Figure 6.9(b), implying the cure anomaly.

In brief, FRPs with the developed implantable sensors can achieve following functions and thus serve as a reference to calibrate the cure progress and guarantee the quality of FRPs of similar kind:

- 1) the ability to perceive GUWs at the uncured phase offers the opportunity to infer the lay-up to scrap a defected part such as expired shelf life of matrix before the start of an expensive and energy-consuming cure cycle;
- 2) the capability to determine the cure degree after the gel point of matrix is essential to assist in maintaining the quality of thus-fabricated composites, as the heating anomaly would result in different cure degrees of matrix, which may bring inconsistent residual strain and thus cause warping of finished composites;
- 3) the capacity to indicate the completion of cure allows the tailored cure schedule to suit the resin age and chemical integrity. A reduction in cure schedule and energy cost may be achieved using cure monitoring.

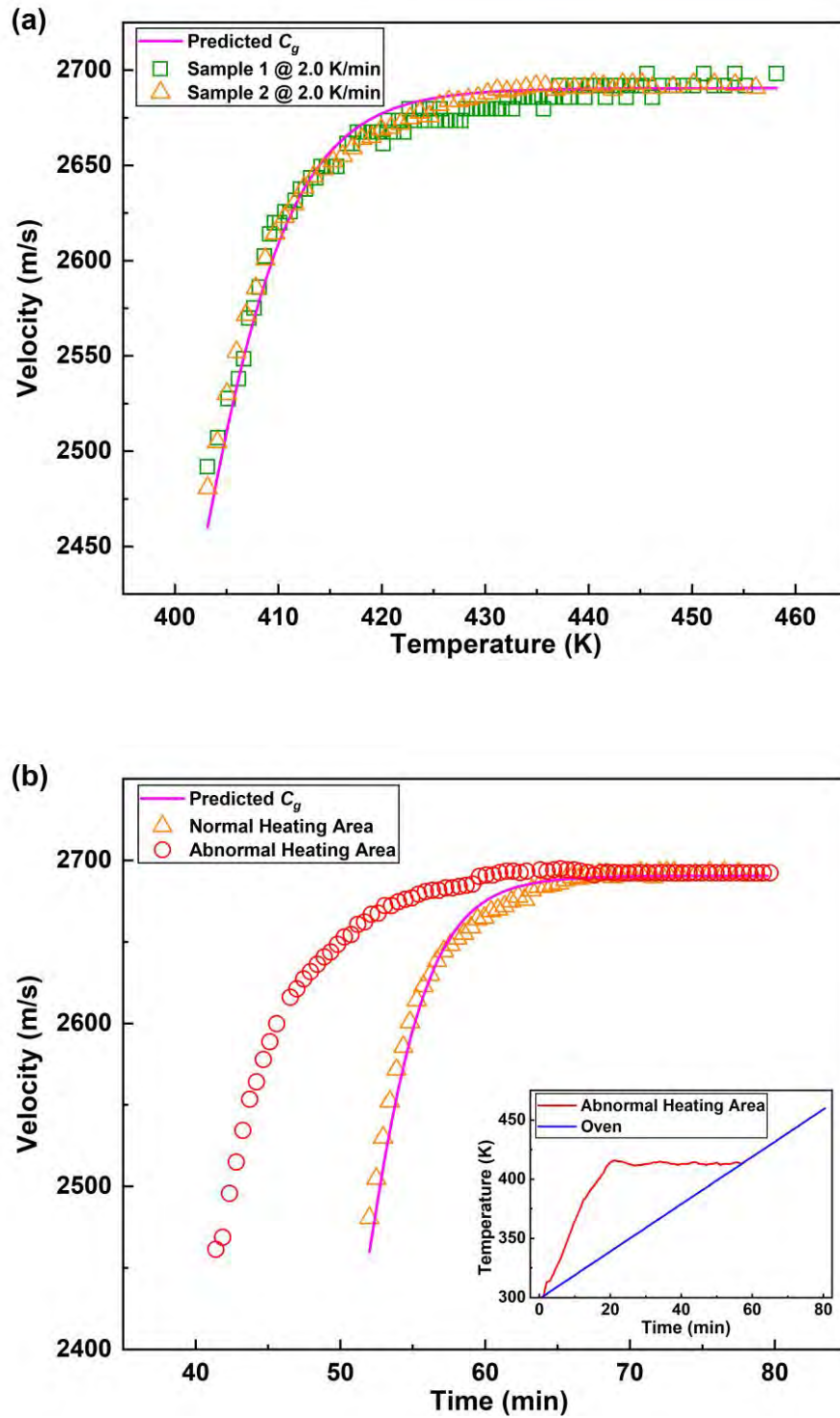


Figure 6.9 (a) Group velocity of S_0 wave mode after the gel point of matrix (at the heating rate of 2 K/min); and (b) comparison of C_g measured in normal and abnormal cure areas (solid line: Sesták–Berggren model and Equation 6.11-predicted results; symbol: experimental results).

6.3 In-service Impact Localization

Subsequent to the above cure progress monitoring, the structural integrity of the same FRP laminate in service is further evaluated, using the same implanted nanocomposite sensor network, to locate a transient impact invasion. The eight nanocomposite sensors in the network are denoted with $S_i (i = 1, 2, \dots, 8)$, enclosing a circular inspection area with a radius of 150 mm, Figure 6.10. As a proof-of-concept validation, a steel ball (\varnothing : 8 mm; weight: 10 g) impinges on the laminate from a height of 250 mm ($\sim 25 \times 10^{-3}$ J impact energy) in a drop-weight impact test and the impact triggers acoustic emission (AE) signals that are captured by the sensors and recorded with the measurement system. Raw signals are applied with a first-order Butterworth low-pass filter with a cut-off frequency of 10 kHz, to suppress measurement noise.

A delay-and-sum triangulation algorithm [126] is recalled to image the impact spot. In the algorithm, the moment t_i , at which the first-arrival wave component is captured with the i^{th} sensor located at (x_i, y_i) , is defined as

$$t_i = t_0 + \Delta t_i, \quad 6.12$$

where t_0 denotes the moment at which the steel ball impinges on the laminate and Δt_i the time for the first-arrival wave component in the AE signal to travel from the

impact spot to S_i . With another sensor S_j at (x_j, y_j) , the difference (*i.e.*, $\Delta t_{ij}(x, y)$) in the arrival time of AE signals captured by S_i and S_j reads

$$\Delta t_{ij}(x, y) = t_i - t_j = (t_0 + \Delta t_i) - (t_0 + \Delta t_j) = \frac{\sqrt{(x-x_i)^2 + (y-y_i)^2} - \sqrt{(x-x_j)^2 + (y-y_j)^2}}{v_{plate}}, \quad 6.13$$

$$(i = 1, 2, \dots, 8)$$

where variables are distinguished by subscripts i and j for two individual sensors, v_{plate} the velocity of the first-arrival wave component and (x, y) the impact spot location. A two-dimensional grey-scale image is obtained using the delay-and-sum triangulation algorithm, in which each pixel value ($\xi_{ij}(x, y)$) is defined as

$$\xi_{ij}(x, y) = \max(E_i + E_j(\Delta t_{ij}(x, y))), \quad 6.14$$

where E is the energy packet of the first-arrival wave component extracted from AE signals. The max operator in the equation defines the maximal of the summation of two signals received by S_i and S_j , which is associated with the probability of impact spot – that is the perception as to the impact spot from the perspective of the sensor pair of S_i and S_j . Aggregating images constructed by all sensor pairs rendered by the sensor network, a superimposed image is made, in which those pixels with greater values have a higher degree of probability of impact spot, and *vice versa*. Figures 6.10(a) and (b) show the raw and filtered signals captured by S_3 and S_5 , as an example; Figure 6.10(c) highlights the identified impact location using the above delay-and-sum algorithm, in which the colour gradient calibrates the probability of

the occurrence of an impact. A high degree of coincidence between the identified impact spot and reality is observed.

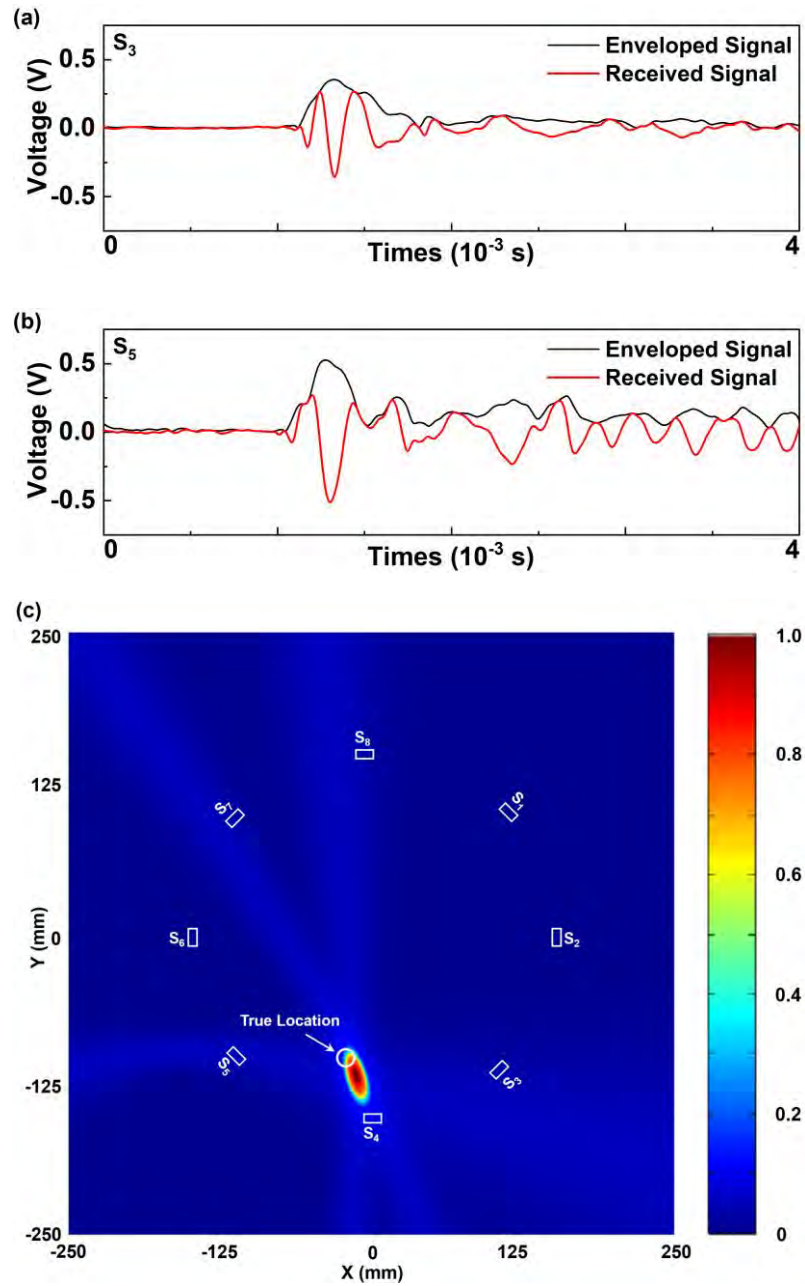


Figure 6.10 (a, b) Representative raw and processed AE signals acquired with S₃ and S₅; and (c) comparison between the real impact spot and the identified spot.

6.4 Summary

This chapter demonstrates a new approach for *in situ*, online monitoring of FRPs using a single type of permanently implanted sensor with neglectable intrusion to the composites, from cure monitoring to in-service impact localization. Being capable of perceiving dynamic strains in a broad frequency range from quasi-static loads to GUWs up to half a megahertz, the sensors endow the composites with a capacity to self-monitor the matrix cure progress and detect the cure anomaly, if any, via interpreting subtle changes in propagation characteristics of sensor-captured GUW signals. The use of the same type of sensor can also be extended to structural integrity evaluation of FRPs when the composites are in service, as proven by the experimental validation.

CHAPTER 7

Conclusions and Recommendations for Future Work

7.1 Conclusions

Fibre-reinforced polymer (FRP) composites are now being widely used to function as load-bearing structural components in land, water, air and space vehicles, owing to their superior mechanical properties. Yet the quality of composites is associated with their manufacturing process and the occurrence of damage, whatever modality it takes, can remarkably jeopardise the durability and reliability of composite structures. Thanks to the presence of guided ultrasonic wave (GUW)-based monitoring, the material integrity can be accurately monitored in an *in situ* and on-line manner, from manufacturing onset through service, to the end of life. A great number of studies have been reported to improve the efficiency and accuracy of GUW-based cure monitoring (CM) or structural health monitoring (SHM) approaches in past decades. For all GUW-based monitoring approaches, sensors or elaborately designed sensor networks, are the most fundamental and important

elements in a monitoring system for the acquisition of signals. Nonetheless, efforts placed on developing GUV-responsive nanocomposite sensors, which can be integrated into composite structures, are fairly limited, though the fact that the most popular ultrasonic sensors (*e.g.*, lead zirconate titanate (PZT) wafers) may intrude the host structures when embedded. Meanwhile, the PZT wafers, along with sensor-associated electrodes and circuits, introduce massive weight penalty to the original composites. Hence, it is essential to develop ultrasonic-sensitive sensors, which can be integrated into composite structures, while not at the cost of mechanical attributes of the original structures.

The recent prosperity in nanotechnology has ushered in a new avenue for the development of functional FRPs, in virtue of fascinating mechanical and electrical properties of nanocomposites. A great many functional composites have already been endowed with functionalities such as sensing, self-healing, energy storage and electromagnetic interference shielding, just to name a few.

Inspired by those achievements, a new genre of sensing fabrics, which can be employed to implement both electrical resistance (ER)-based and acousto-ultrasonics-based monitoring of glass fibre-reinforced polymer (GFRP) composites, is initially, rigorously prepared in this study. Outperforming conventional nanocomposite sensors, which are restricted to the ER measurement-based

monitoring approaches, such sensing fabrics can be extendedly introduced to implement acousto-ultrasonics-based monitoring, relying on the quantum tunnelling effect.

In a frequency regime up to 375 kHz, the carbon nanotube (CNT)-grafted sensing fabrics exhibit high sensitivity towards GUWs, by right of the tailored appropriate mass fraction of grafted CNTs. The low CNT grafting temperature at 500 °C guarantees the slight variation in the tensile strength of fibres as proven by single fibre tensile test (ASTM C1557) and fibre-reinforced polymer matrix composite tensile test (ASTM D3039), while not scrutinizing the graphitization degree of synthesized CNTs (with I_d/I_g ratios <0.89). Such CNT-grafted sensing fabrics can perform ER-based continuous monitoring: to distinguish three key stages of epoxy resin in a cure and precisely sense loads applied to in-service composite structures, with a gauge factor of 30.2.

An implantable, compatible and networkable nanocomposite sensor, formulated with graphene nanoplatelets (GNPs) and polyvinylpyrrolidone (PVP), is further developed to enable sensor networks to be integrated into carbon fibre-reinforced polymer (CFRP) composites. With the acquired percolation threshold of GNPs, the sensors precisely and faithfully respond to disturbances induced by quasi-static loads (with a high gauge factor of 34.5) and structural vibrations. After that, the performance of

such sensors in perceiving GUWs is also validated up to frequency of 450 kHz, in virtue of the quantum tunneling effect.

Employing partially precured ($\alpha = 0.4$) B-stage epoxy as dielectric membranes and highly conductive CNT-film-made wires as circuits, the sensors demonstrate high compatibility and nonintrusive attributes to the host composites, as proven by the microscopic morphological characterization of composites with implanted sensors. What is more, the mechanical property investigation also reveals that the tensile and bending strengths of composites only changed slightly, by 2.65% and 3.74% respectively, due to the implantation of sensors.

With their fascinating traits such as compatible and extra-lightweight, thus-produced sensors impose neglectable intrusion, weight and volume penalties to the host structures, yet are capable of extracting rich information of monitored composites, provided they are densely deployed and instrumented. Such a superiority makes the implantable sensors outperform conventional ultrasonic sensors (*e.g.*, PZT wafers and polyvinylidene fluoride (PVDF) film sensors), which in general are sparsely configured to meet a compromise between cost and efficiency. With appropriate communication and networking, the sensors holistically capture the information of the monitored structures, to satisfy acousto-ultrasonics-based monitoring of engineering assets. Two proof-of-concept paradigms are performed to verify the

monitoring capabilities of the implantable sensors at both manufacturing and application phases of the composites. The sensors successfully trace the cure progress and detect the cure anomaly of epoxy resin through evaluating fluctuations of captured G UW signals. Furthermore, the sensors show a talent in in-service SHM, to pinpoint and assess the location and severity of an impingement.

In summary, the nanocomposite sensors, which are specially developed for G UW-based monitoring schemes in this study, feature merits listed below, to meet the requirements and objectives originally proposed:

- 1) **broadband responsive frequency regime:** these genres of sensors possess the ability to respond to strains induced by quasi-static tensile loads (gauge factors larger than 30), medium-frequency structural vibrations and high-frequency G UWs up to circa half a megahertz.
- 2) **neglectable intrusion to host composite structures:** the mechanical tests carried out have proven the noninvasive attributes of the developed sensors, either the CNT-grafted sensing fabrics or the implantable nanocomposite sensors, when they are integrated into FRPs; on top of that, the developed communication systems, which are made of highly conductive CNT-film-made wires and abandon electrodes, break up an innovative path for the instrumentation of integrated sensing systems;

- 3) **robust cure monitoring and in-service integrity monitoring capabilities:** the sensors developed possess either ER-based or GUV-based monitoring abilities, from manufacturing through service, to trace resin cure behaviors in preparation and then monitor health states of thus-finished composite structures.

7.2 Recommendations for Future Work

Though the developed nanocomposite sensors feature a great many proven merits, several issues are still waiting to be solved, to enable the sensors to be further applied in practical applications. Improving the sensing performance of the integratable nanocomposite sensors is among those impending initiatives, which can be achieved via further optimizing the nanostructure of nanocomposites. Second, the mechanical performance of the integrated composites under dynamic or cyclic loading scenarios needs to be fully validated. There is another important issue which should not be neglected, that is, the fabrication of epoxy membranes and the alignment of CNT-film-made wires are still of manual manipulation, which may be inefficient and introduce the performance discrepancy among individual sensors. Some hypothetical solutions to optimize the integrated sensing system are proposed as follows:

- 1) the agglomeration of nanoparticles can be solved via various approaches embracing the ultrasonication-assisted dispersion, mechanical stirring, calendaring, chemical grafting, *etc.* Specifically, with grafted functional groups,

graphene and its derivatives can be dispersed in polymers more evenly, thanks to the formation of hydrogen bondings and coordination bonds;

- 2) to further explore the impact of integrated sensor networks on the structural integrity of composites under dynamic loadings, tension-tension fatigue test can be implemented to evaluate residual properties of composites with or without integrated sensors, to examine the durability and survivability of both sensors and host structures;
- 3) a totally additive manufacturing (AM) driven approach will be applied to functionalize CFRPs with the capacity of *in situ*, real-time GUV-based integrity monitoring. A nanocomposite-based, implantable sensing network layer, replacing the above developed implantable sensors and fabricated in virtue of a new concept of totally additive manufacturing (all components of the sensing layer will be uninterruptedly made using AM in one go), will be developed to abandon conventional sensor embedding or mounting, diminish sensor intrusion and minimize mechanical degradation of composites. Design of the sensing network layer will first be done in SolidWorks[®] and printing traces will be simulated using Toolpath Generation Software (Mastercam[®]). The aerosol jet printing (AJP) facility, schematically shown in Figure 7.1(a), features multiple and interchangeable atomization cassettes and deposition heads, making it possible to continuously and uninterruptedly print different components of the entire sensing network layer (including sensing units, dielectric membranes,

electrodes and wires) without the need to pause printing for the replacement of heads and materials. The detailed fabrication process includes following four key steps in sequence: first, an ultrathin epoxy membrane will be printed using AJP, to prevent sensors and circuits from short-circuit by carbon fibers. In AJP, the viscosity, morphology and thickness of the membranes are controllable, whereby to minimize the possible intrusion of the implanted layer to CFRPs as AJP facility allows the width of the printed trace to vary from 10 microns to millimeters and the thickness from 100 nm to microns. The GNPs/PVP nanocomposite ink will be continually printed on the above AJP-fabricated lower membrane, at the positions in accordance with a desired sensing network pattern. An exemplary pattern of the sensing network is shown in Figure 7.2. Key parameters, such as the flow rate of the carrier gas (for transporting the aerosol mist to the head), the flow rate of the sheath gas (for collimating the aerosol into a narrow beam) and the speed of the stage (for transporting the substrate beneath the beam), will be investigated carefully and optimized, so as to boost the sensitivity of the printed sensing units to high-frequency GUWs. After that, the highly conductive CNT-films will first be tailored into thin wires with the width of 1 ± 0.1 mm and thickness of 10 ± 5 microns. A fused deposition modeling (FDM) nozzle will be customized to precisely indent above prepared continuous CNT-film wires, in Figure 7.1(b), with a high spatial resolution (down to <1 micron). In this process, the polymer matrix and CNT-film will be

infused in a guide pipe. A booster pump will increase the inner pressure of the guide pipe to extrude the CNT-film (which is impregnated with polymer matrix in the guide pipe). Atop each sensing unit, silver epoxy adhesive with the viscosity of 100-200 cP (Resin Design[®] ACURA E8074) will be deposited on CNT-film wire ends, to function as electrodes for each sensing unit, which guarantee good adhesion between sensing units and wires, and also a low contact resistance. Individual sensing unit will be electrified and networked by the CNT-film wires, to form a dense sensing network layer. Another layer of polymer matrix (the upper membrane), identical to the above lower epoxy membrane, will be printed directly atop the sensing network layer. After sufficient curing, the sensing network layer, sealed by the upper and lower membranes, can be implanted into CFRP panels during lay-up, as an additional ply to be inserted between prepreg plies, as shown in Figure 7.3.

Furthermore, more practical validations related to active GUV-based monitoring in conjunction with developed integratable nanocomposite sensors should be carried out in the future, to detect buried defects such as delamination, fibre breakage, matrix ageing and impact-induced damage.

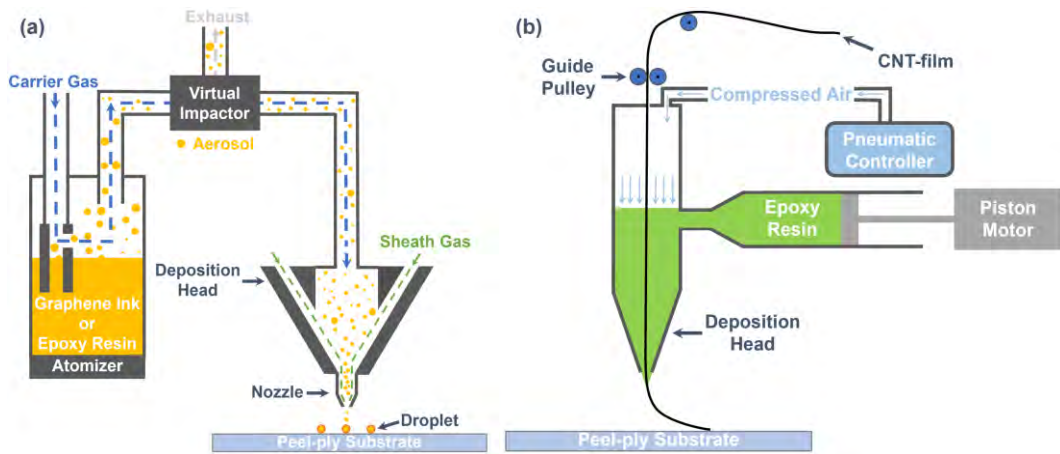


Figure 7.1 AM-driven approaches for fabricating (a) sensing units via AJP; and (b) wires/circuits via FDM.

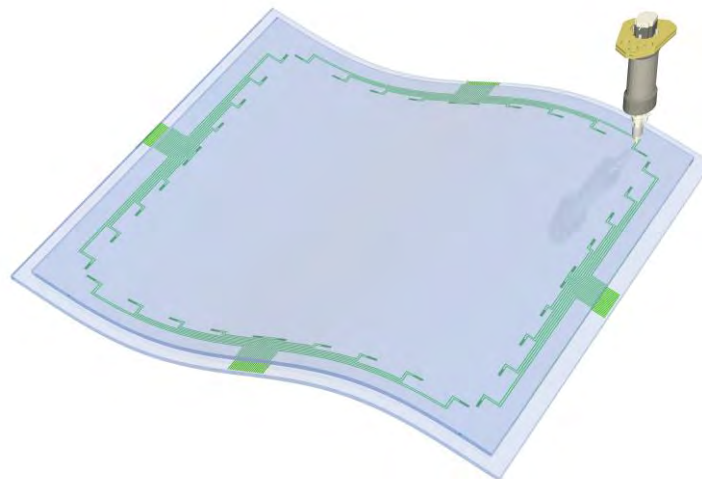


Figure 7.2 Schematic of an AM-driven integratable sensing network layer.

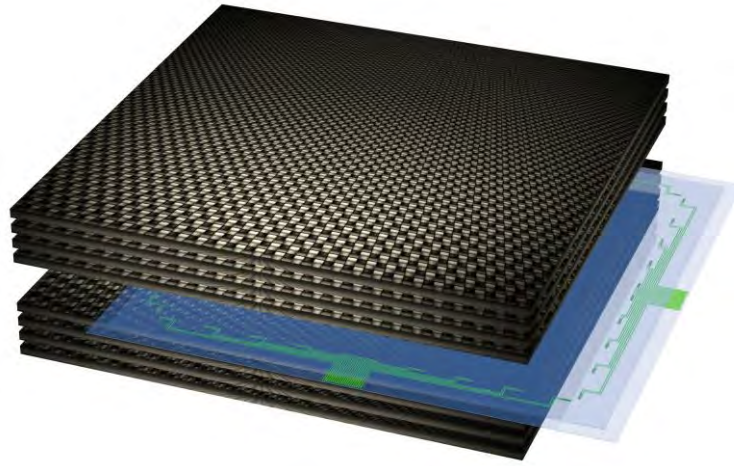


Figure 7.3 Implantation of the sensing network layer in CFRPs.

Bibliography

- [1] J. Karger-Kocsis, H. Mahmood, A. Pegoretti, All-carbon multi-scale and hierarchical fibers and related structural composites: A review, *Composites Science and Technology* 186 (2020) 107932.
- [2] S. Lu, D. Chen, X. Wang, J. Shao, K. Ma, L. Zhang, S. Araby, Q. Meng, Real-time cure behaviour monitoring of polymer composites using a highly flexible and sensitive CNT buckypaper sensor, *Composites Science and Technology* 152 (2017) 181-189.
- [3] Y. Xiao, W. Qiao, H. Fukuda, H. Hatta, The effect of embedded devices on structural integrity of composite laminates, *Composite Structures* 153 (2016) 21-29.
- [4] J.P. Lynch, A. Partridge, K.H. Law, T.W. Kenny, A.S. Kiremidjian, E. Carryer, Design of piezoresistive MEMS-based accelerometer for integration with wireless sensing unit for structural monitoring, *Journal of Aerospace Engineering* 16(3) (2003) 108-114.
- [5] M.B. Rao, M. Bhat, C. Murthy, K.V. Madhav, S. Asokan, Structural health monitoring (SHM) using strain gauges, PVDF film and fiber bragg grating (FBG) sensors: A comparative study, *Proc. National Seminar on Non-Destructive Evaluation*, Citeseer, 2006, pp. 7-9.
- [6] G.C. Kahandawa, J. Epaarachchi, H. Wang, K. Lau, Use of FBG sensors for SHM in aerospace structures, *Photonic Sensors* 2(3) (2012) 203-214.
- [7] V.K. Varadan, *Wireless microsensors for health monitoring of aircraft structures, MEMS Components and Applications for Industry, Automobiles, Aerospace, and Communication II*, International Society for Optics and Photonics, 2003, pp. 175-188.
- [8] K.-C. Chuang, C.-C. Ma, C.-K. Chang, Determination of dynamic history of impact loadings using polyvinylidene fluoride (PVDF) films, *Experimental*

Mechanics 54(3) (2014) 483-488.

[9] H. Alnuaimi, U. Amjad, P. Russo, V. Lopresto, T. Kundu, Monitoring damage in composite plates from crack initiation to macro-crack propagation combining linear and nonlinear ultrasonic techniques, *Structural Health Monitoring* 20(1) (2021) 139-150.

[10] H. Mei, M.F. Haider, R. James, V. Giurgiutiu, Pure S0 and SH0 detections of various damage types in aerospace composites, *Composites Part B: Engineering* 189 (2020) 107906.

[11] M. Lin, F.-K. Chang, The manufacture of composite structures with a built-in network of piezoceramics, *Composites Science and Technology* 62(7-8) (2002) 919-939.

[12] C. Andreades, P. Mahmoodi, F. Ciampa, Characterisation of smart CFRP composites with embedded PZT transducers for nonlinear ultrasonic applications, *Composite Structures* 206 (2018) 456-466.

[13] H.P. Konka, M. Wahab, K. Lian, The effects of embedded piezoelectric fiber composite sensors on the structural integrity of glass-fiber–epoxy composite laminate, *Smart Materials and Structures* 21(1) (2011) 015016.

[14] S. Nag-Chowdhury, H. Bellegou, I. Pillin, M. Castro, P. Longrais, J. Feller, Non-intrusive health monitoring of infused composites with embedded carbon quantum piezo-resistive sensors, *Composites Science and Technology* 123 (2016) 286-294.

[15] X. Huang, B. Patham, Experimental characterization of a curing thermoset epoxy-anhydride system—Isothermal and nonisothermal cure kinetics, *Journal of Applied Polymer Science* 127(3) (2013) 1959-1966.

[16] G. George, G. Cash, L. Rintoul, Cure monitoring of aerospace epoxy resins and prepregs by Fourier transform infrared emission spectroscopy, *Polymer International* 41(2) (1996) 169-182.

[17] W. Stark, Investigation of the curing behaviour of carbon fibre epoxy prepreg by Dynamic Mechanical Analysis DMA, *Polymer Testing* 32(2) (2013) 231-239.

- [18] H. Stutz, J. Mertes, Torsional braid analysis and gelation in thermoset resins, *Journal of Applied Polymer Science* 38(5) (1989) 781-787.
- [19] M.K. Moghaddam, A. Breede, A. Chaloupka, A. Boedecker, C. Habben, E.-M. Meyer, C. Brauner, W. Lang, Design, fabrication and embedding of microscale interdigital sensors for real-time cure monitoring during composite manufacturing, *Sensors and Actuators A: Physical* 243 (2016) 123-133.
- [20] R. Harrold, Z. Sanjana, Acoustic waveguide monitoring of the cure and structural integrity of composite materials, *Polymer Engineering & Science* 26(5) (1986) 367-372.
- [21] D.M. Sánchez, M. Gresil, C. Soutis, Distributed internal strain measurement during composite manufacturing using optical fibre sensors, *Composites Science and Technology* 120 (2015) 49-57.
- [22] K. Mizukami, S. Yoshimoto, K. Ogi, In-process acquisition of cure-dependent viscoelastic properties of carbon fiber reinforced composites using micromechanics-based guided wave analysis, *Polymer Testing* 65 (2018) 459-467.
- [23] K. Mizukami, T. Ikeda, K. Ogi, Measurement of velocity and attenuation of ultrasonic guided wave for real-time estimation of cure-dependent anisotropic viscoelastic properties of carbon fiber-reinforced plastics, *Ultrasonics* 99 (2019) 105952.
- [24] G. Fernando, B. Degamber, Process monitoring of fibre reinforced composites using optical fibre sensors, *International Materials Reviews* 51(2) (2006) 65-106.
- [25] V. Dewynter-Marty, P. Ferdinand, E. Bocherens, R. Carbone, H. Beranger, S. Bourasseau, M. Dupont, D. Balageas, Embedded fiber Bragg grating sensors for industrial composite cure monitoring, *Journal of Intelligent Material Systems and Structures* 9(10) (1998) 785-787.
- [26] V. Antonucci, M. Giordano, A. Cusano, J. Nasser, L. Nicolais, Real time monitoring of cure and gelification of a thermoset matrix, *Composites Science and Technology* 66(16) (2006) 3273-3280.

- [27] L. Sorrentino, C. Bellini, D. Capriglione, L. Ferrigno, Local monitoring of polymerization trend by an interdigital dielectric sensor, *The International Journal of Advanced Manufacturing Technology* 79(5) (2015) 1007-1016.
- [28] A. Maffezzoli, E. Quarta, V. Luprano, G. Montagna, L. Nicolais, Cure monitoring of epoxy matrices for composites by ultrasonic wave propagation, *Journal of Applied Polymer Science* 73(10) (1999) 1969-1977.
- [29] X. Qing, X. Liu, J. Zhu, Y. Wang, In-situ monitoring of liquid composite molding process using piezoelectric sensor network, *Structural Health Monitoring* (2020) 1475921720958082.
- [30] J.S. Chilles, A.F. Koutsomitopoulou, A.J. Croxford, I.P. Bond, Monitoring cure and detecting damage in composites with inductively coupled embedded sensors, *Composites Science and Technology* 134 (2016) 81-88.
- [31] X. Liu, Y. Li, J. Zhu, Y. Wang, X. Qing, Monitoring of resin flow front and degree of cure in vacuum-assisted resin infusion process using multifunctional piezoelectric sensor network, *Polymer Composites* 42(1) (2021) 113-125.
- [32] M. Ibrahim, Nondestructive evaluation of thick-section composites and sandwich structures: A review, *Composites Part A: Applied Science and Manufacturing* 64 (2014) 36-48.
- [33] Z. Su, L. Ye, X. Bu, A damage identification technique for CF/EP composite laminates using distributed piezoelectric transducers, *Composite Structures* 57(1-4) (2002) 465-471.
- [34] Z. Su, L. Ye, Lamb wave-based quantitative identification of delamination in CF/EP composite structures using artificial neural algorithm, *Composite Structures* 66(1-4) (2004) 627-637.
- [35] Z. Su, X. Wang, Z. Chen, L. Ye, D. Wang, A built-in active sensor network for health monitoring of composite structures, *Smart Materials and Structures* 15(6) (2006) 1939.
- [36] M. Lin, F.-K. Chang, Composite structures with built-in diagnostics, *Materials*

Today 2(2) (1999) 18-22.

[37] M. Lin, X. Qing, A. Kumar, S.J. Beard, Smart layer and smart suitcase for structural health monitoring applications, Smart structures and materials 2001: industrial and commercial applications of smart structures technologies, International Society for Optics and Photonics, 2001, pp. 98-106.

[38] C.S. Wang, J. Park, F.-K. Chang, Impact damage identification of composite structures with built-in piezoelectric sensor/actuator networks, Stanford Univ CA Dept of Aeronautics and Astronautics, 1999.

[39] X.P. Qing, S.J. Beard, A. Kumar, H.-L. Chan, R. Ikegami, Advances in the development of built-in diagnostic system for filament wound composite structures, Composites Science and Technology 66(11-12) (2006) 1694-1702.

[40] P. Schubel, R. Crossley, E. Boateng, J. Hutchinson, Review of structural health and cure monitoring techniques for large wind turbine blades, Renewable Energy 51 (2013) 113-123.

[41] A. McIlhagger, D. Brown, B. Hill, The development of a dielectric system for the on-line cure monitoring of the resin transfer moulding process, Composites Part A: Applied Science and Manufacturing 31(12) (2000) 1373-1381.

[42] Z. Su, L. Ye, Y. Lu, Guided Lamb waves for identification of damage in composite structures: A review, Journal of Sound and Vibration 295(3-5) (2006) 753-780.

[43] Z.Q. Su, L. Cheng, X.M. Wang, L. Yu, Diagnostic imaging for structural damage, Advanced Materials Research, Trans Tech Publ, 2008, pp. 1157-1160.

[44] J. Achenbach, Wave propagation in elastic solids, Elsevier 2012.

[45] J.L. Rose, Ultrasonic guided waves in solid media, Cambridge University Press 2014.

[46] W. Ostachowicz, P. Kudela, P. Malinowski, T. Wandowski, Damage localisation in plate-like structures based on PZT sensors, Mechanical Systems and Signal Processing 23(6) (2009) 1805-1829.

- [47] C. Wang, L. Rose, Wave reflection and transmission in beams containing delamination and inhomogeneity, *Journal of Sound and Vibration* 264(4) (2003) 851-872.
- [48] B. Ren, C.J. Lissenden, Ultrasonic guided wave inspection of adhesive bonds between composite laminates, *International Journal of Adhesion and Adhesives* 45 (2013) 59-68.
- [49] Z. Zhang, M. Liu, Z. Su, Y. Xiao, Quantitative evaluation of residual torque of a loose bolt based on wave energy dissipation and vibro-acoustic modulation: A comparative study, *Journal of Sound and Vibration* 383 (2016) 156-170.
- [50] J.E. Michaels, T.E. Michaels, Guided wave signal processing and image fusion for in situ damage localization in plates, *Wave Motion* 44(6) (2007) 482-492.
- [51] Y. Li, K. Wang, Q. Wang, J. Yang, P. Zhou, Y. Su, S. Guo, Z. Su, Acousto-ultrasonics-based health monitoring for nano-engineered composites using a dispersive graphene-networked sensing system, *Structural Health Monitoring* 20(1) (2021) 240-254.
- [52] P. Zhou, W. Cao, Y. Liao, K. Wang, X. Yang, J. Yang, Y. Su, L. Xu, L.-m. Zhou, Z. Zhang, Temperature effect on all-inkjet-printed nanocomposite piezoresistive sensors for ultrasonics-based health monitoring, *Composites Science and Technology* 197 (2020) 108273.
- [53] D.N. Alleyne, P. Cawley, The interaction of Lamb waves with defects, *IEEE Transactions on Ultrasonics, Ferroelectrics, and Frequency Control* 39(3) (1992) 381-397.
- [54] Y. Li, Graphene nanoparticle-functionalized polymer composites for self-sensing ultrasonic waves: an initiative towards" sensor-free" structural health monitoring, (2019).
- [55] X. Liu, J. Li, J. Zhu, Y. Wang, X. Qing, Cure monitoring and damage identification of CFRP using embedded piezoelectric sensors network, *Ultrasonics* 115 (2021) 106470.

- [56] P.-C. Ma, N.A. Siddiqui, G. Marom, J.-K. Kim, Dispersion and functionalization of carbon nanotubes for polymer-based nanocomposites: A review, *Composites Part A: Applied Science and Manufacturing* 41(10) (2010) 1345-1367.
- [57] D. Bethune, C.H. Kiang, M. De Vries, G. Gorman, R. Savoy, J. Vazquez, R. Beyers, Cobalt-catalysed growth of carbon nanotubes with single-atomic-layer walls, *Nature* 363(6430) (1993) 605-607.
- [58] C. Li, E.T. Thostenson, T.-W. Chou, Sensors and actuators based on carbon nanotubes and their composites: a review, *Composites Science and Technology* 68(6) (2008) 1227-1249.
- [59] D. Qian, a. Wagner, Gregory J, W.K. Liu, M.-F. Yu, R.S. Ruoff, Mechanics of carbon nanotubes, *Applied Mechanics Reviews* 55(6) (2002) 495-533.
- [60] C.E. Baddour, C. Briens, Carbon nanotube synthesis: a review, *International Journal of Chemical Reactor Engineering* 3(1) (2005).
- [61] Y. Li, Y. Liao, Z. Su, Graphene-functionalized polymer composites for self-sensing of ultrasonic waves: An initiative towards “sensor-free” structural health monitoring, *Composites Science and Technology* 168 (2018) 203-213.
- [62] S.R. Shin, Y.-C. Li, H.L. Jang, P. Khoshakhlagh, M. Akbari, A. Nasajpour, Y.S. Zhang, A. Tamayol, A. Khademhosseini, Graphene-based materials for tissue engineering, *Advanced Drug Delivery Reviews* 105 (2016) 255-274.
- [63] A.A. Balandin, S. Ghosh, W. Bao, I. Calizo, D. Teweldebrhan, F. Miao, C.N. Lau, Superior thermal conductivity of single-layer graphene, *Nano Letters* 8(3) (2008) 902-907.
- [64] X. Ji, Y. Xu, W. Zhang, L. Cui, J. Liu, Review of functionalization, structure and properties of graphene/polymer composite fibers, *Composites Part A: Applied Science and Manufacturing* 87 (2016) 29-45.
- [65] L. Zhang, F. Zhang, X. Yang, G. Long, Y. Wu, T. Zhang, K. Leng, Y. Huang, Y. Ma, A. Yu, Porous 3D graphene-based bulk materials with exceptional high surface area and excellent conductivity for supercapacitors, *Scientific Reports* 3(1) (2013) 1-

9.

[66] E. Kan, Z. Li, J. Yang, Graphene nanoribbons: geometric, electronic, and magnetic properties, ISBN 2011.

[67] Y. Li, Z. Feng, L. Huang, K. Essa, E. Bilotti, H. Zhang, T. Peijs, L. Hao, Additive manufacturing high performance graphene-based composites: A review, Composites Part A: Applied Science and Manufacturing 124 (2019) 105483.

[68] A. Hernández-Pérez, F. Avilés, A. May-Pat, A. Valadez-González, P. Herrera-Franco, P. Bartolo-Pérez, Effective properties of multiwalled carbon nanotube/epoxy composites using two different tubes, Composites Science and Technology 68(6) (2008) 1422-1431.

[69] W. Bauhofer, J.Z. Kovacs, A review and analysis of electrical percolation in carbon nanotube polymer composites, Composites Science and Technology 69(10) (2009) 1486-1498.

[70] E.T. Thostenson, T.W. Chou, Carbon nanotube networks: sensing of distributed strain and damage for life prediction and self healing, Advanced Materials 18(21) (2006) 2837-2841.

[71] L. Böger, M.H. Wichmann, L.O. Meyer, K. Schulte, Load and health monitoring in glass fibre reinforced composites with an electrically conductive nanocomposite epoxy matrix, Composites Science and Technology 68(7-8) (2008) 1886-1894.

[72] W. Li, A. Dichiara, J. Bai, Carbon nanotube-graphene nanoplatelet hybrids as high-performance multifunctional reinforcements in epoxy composites, Composites Science and Technology 74 (2013) 221-227.

[73] B. Yang, F.-Z. Xuan, Z. Wang, L. Chen, H. Lei, W. Liang, Y. Xiang, K. Yang, Multi-functional interface sensor with targeted IFSS enhancing, interface monitoring and self-healing of GF/EVA thermoplastic composites, Composites Science and Technology 167 (2018) 86-95.

[74] B. Yang, F.-Z. Xuan, H. Lei, Z. Wang, Y. Xiang, K. Yang, X. Tang, W. Liang, Simultaneously enhancing the IFSS and monitoring the interfacial stress state of

GF/epoxy composites via building in the MWCNT interface sensor, *Composites Part A: Applied Science and Manufacturing* 112 (2018) 161-167.

[75] S. Luo, G. Wang, Y. Wang, Y. Xu, Y. Luo, Carbon nanomaterials enabled fiber sensors: A structure-oriented strategy for highly sensitive and versatile in situ monitoring of composite curing process, *Composites Part B: Engineering* 166 (2019) 645-652.

[76] H. Dai, E.T. Thostenson, Scalable and multifunctional carbon nanotube-based textile as distributed sensors for flow and cure monitoring, *Carbon* 164 (2020) 28-41.

[77] R. Sager, P. Klein, D. Lagoudas, Q. Zhang, J. Liu, L. Dai, J. Baur, Effect of carbon nanotubes on the interfacial shear strength of T650 carbon fiber in an epoxy matrix, *Composites Science and Technology* 69(7-8) (2009) 898-904.

[78] H. Zhang, Y. Liu, M. Kuwata, E. Bilotti, T. Peijs, Improved fracture toughness and integrated damage sensing capability by spray coated CNTs on carbon fibre prepreg, *Composites Part A: Applied Science and Manufacturing* 70 (2015) 102-110.

[79] J. Rodríguez-González, C. Rubio-González, J. Ku-Herrera, Influence of seawater ageing on the mechanical and damage self-sensing capability of glass fiber-MWCNT/epoxy laminates subjected to flexural loading by means of the electrical resistance approach, *Smart Materials and Structures* 27(12) (2018) 125002.

[80] K. Almuhammadi, M. Alfano, Y. Yang, G. Lubineau, Analysis of interlaminar fracture toughness and damage mechanisms in composite laminates reinforced with sprayed multi-walled carbon nanotubes, *Materials & Design* 53 (2014) 921-927.

[81] J. Rodríguez-González, C. Rubio-Gonzalez, Mixed-mode I/II interlaminar fracture toughness of carbon fiber/epoxy composites with the addition of multiwalled carbon nanotubes by spraying technique, *Journal of Composite Materials* 52(22) (2018) 3045-3052.

[82] S. Luo, T. Liu, Graphite nanoplatelet enabled embeddable fiber sensor for in situ curing monitoring and structural health monitoring of polymeric composites, *ACS Applied Materials & Interfaces* 6(12) (2014) 9314-9320.

- [83] S. Luo, W. Obitayo, T. Liu, SWCNT-thin-film-enabled fiber sensors for lifelong structural health monitoring of polymeric composites-From manufacturing to utilization to failure, *Carbon* 76 (2014) 321-329.
- [84] M. Al-Bahrani, Z.J. Gombos, A. Cree, Investigation of the constancy of the MWCNTs on the fibres surface for manufactured self-sensing composites, *Composites Part B: Engineering* 173 (2019) 106998.
- [85] D.H. Sung, S.M. Doshi, C. Murray, A.N. Rider, E.T. Thostenson, Electrophoretic deposition: Novel in situ film growth mechanism of carbon nanocomposite films within non-conductive fabrics for multi-scale hybrid composites, *Composites Science and Technology* 200 (2020) 108415.
- [86] J. Zhang, R. Zhuang, J. Liu, E. Mäder, G. Heinrich, S. Gao, Functional interphases with multi-walled carbon nanotubes in glass fibre/epoxy composites, *Carbon* 48(8) (2010) 2273-2281.
- [87] M. Atiq Ur Rehman, Q. Chen, A. Braem, M.S. Shaffer, A.R. Boccaccini, Electrophoretic deposition of carbon nanotubes: recent progress and remaining challenges, *International Materials Reviews* (2020) 1-30.
- [88] C. Wang, J. Li, S. Sun, X. Li, F. Zhao, B. Jiang, Y. Huang, Electrophoretic deposition of graphene oxide on continuous carbon fibers for reinforcement of both tensile and interfacial strength, *Composites Science and Technology* 135 (2016) 46-53.
- [89] M. Park, J.H. Park, B. Yang, J. Cho, S.Y. Kim, I. Jung, Enhanced interfacial, electrical, and flexural properties of polyphenylene sulfide composites filled with carbon fibers modified by electrophoretic surface deposition of multi-walled carbon nanotubes, *Composites Part A: Applied Science and Manufacturing* 109 (2018) 124-130.
- [90] Y.J. Kwon, Y. Kim, H. Jeon, S. Cho, W. Lee, J.U. Lee, Graphene/carbon nanotube hybrid as a multi-functional interfacial reinforcement for carbon fiber-reinforced composites, *Composites Part B: Engineering* 122 (2017) 23-30.

- [91] M. Kumar, Y. Ando, Chemical vapor deposition of carbon nanotubes: a review on growth mechanism and mass production, *Journal of Nanoscience and Nanotechnology* 10(6) (2010) 3739-3758.
- [92] Y. Zhang, L. Zhang, C. Zhou, Review of chemical vapor deposition of graphene and related applications, *Accounts of Chemical Research* 46(10) (2013) 2329-2339.
- [93] Z. Yao, C. Wang, R. Lu, S. Su, J. Qin, Y. Wang, Z. Ma, H. Wei, Q. Wang, Fracture investigation of functionalized carbon nanotubes-grown carbon fiber fabrics/epoxy composites, *Composites Science and Technology* 195 (2020) 108161.
- [94] Z. Sha, Z. Han, S. Wu, F. Zhang, M.S. Islam, S.A. Brown, C.-H. Wang, Low-temperature plasma assisted growth of vertical graphene for enhancing carbon fibre/epoxy interfacial strength, *Composites Science and Technology* 184 (2019) 107867.
- [95] T.R. Pozegic, I. Hamerton, J.V. Anguita, W. Tang, P. Balocchi, P. Jenkins, S.R.P. Silva, Low temperature growth of carbon nanotubes on carbon fibre to create a highly networked fuzzy fibre reinforced composite with superior electrical conductivity, *Carbon* 74 (2014) 319-328.
- [96] J. Sebastian, N. Schehl, M. Bouchard, M. Boehle, L. Li, A. Lagounov, K. Lafdi, Health monitoring of structural composites with embedded carbon nanotube coated glass fiber sensors, *Carbon* 66 (2014) 191-200.
- [97] D. He, B. Fan, H. Zhao, X. Lu, M. Yang, Y. Liu, J. Bai, Design of electrically conductive structural composites by modulating aligned CVD-grown carbon nanotube length on glass fibers, *ACS Applied Materials & Interfaces* 9(3) (2017) 2948-2958.
- [98] H. De Luca, D. Anthony, E. Greenhalgh, A. Bismarck, M. Shaffer, Piezoresistive structural composites reinforced by carbon nanotube-grafted quartz fibres, *Composites Science and Technology* 198 (2020) 108275.
- [99] S. Lu, C. Zhao, L. Zhang, D. Chen, D. Chen, X. Wang, K. Ma, Real time monitoring of the curing degree and the manufacturing process of fiber reinforced

composites with a carbon nanotube buckypaper sensor, *RSC Advances* 8(39) (2018) 22078-22085.

[100] K. Aly, A. Li, P.D. Bradford, In-situ monitoring of woven glass fiber reinforced composites under flexural loading through embedded aligned carbon nanotube sheets, *Journal of Composite Materials* 52(20) (2018) 2777-2788.

[101] Y. Ou, C. González, J.J. Vilatela, Interlaminar toughening in structural carbon fiber/epoxy composites interleaved with carbon nanotube veils, *Composites Part A: Applied Science and Manufacturing* 124 (2019) 105477.

[102] S.R. White, N.R. Sottos, P.H. Geubelle, J.S. Moore, M.R. Kessler, S. Sriram, E.N. Brown, S. Viswanathan, Autonomic healing of polymer composites, *Nature* 409(6822) (2001) 794-797.

[103] M. Kessler, S. White, Self-activated healing of delamination damage in woven composites, *Composites Part A: Applied Science and Manufacturing* 32(5) (2001) 683-699.

[104] N. Kwok, H.T. Hahn, Resistance heating for self-healing composites, *Journal of Composite Materials* 41(13) (2007) 1635-1654.

[105] Y. Heo, H.A. Sodano, Thermally responsive self-healing composites with continuous carbon fiber reinforcement, *Composites Science and Technology* 118 (2015) 244-250.

[106] Y. Yu, B. Zhang, M. Feng, G. Qi, F. Tian, Q. Feng, J. Yang, S. Wang, Multifunctional structural lithium ion batteries based on carbon fiber reinforced plastic composites, *Composites Science and Technology* 147 (2017) 62-70.

[107] X. Luo, D. Chung, Carbon-fiber/polymer-matrix composites as capacitors, *Composites Science and Technology* 61(6) (2001) 885-888.

[108] P. Ladpli, R. Nardari, F. Kopsaftopoulos, F.-K. Chang, Multifunctional energy storage composite structures with embedded lithium-ion batteries, *Journal of Power Sources* 414 (2019) 517-529.

[109] J.P. Thomas, M.A. Qidwai, The design and application of multifunctional

structure-battery materials systems, *JOM* 57(3) (2005) 18.

[110] J.F. Snyder, R.H. Carter, E.D. Wetzel, Electrochemical and mechanical behavior in mechanically robust solid polymer electrolytes for use in multifunctional structural batteries, *Chemistry of Materials* 19(15) (2007) 3793-3801.

[111] E.S. Greenhalgh, J. Ankersen, L.E. Asp, A. Bismarck, Q. Fontana, M. Houille, G. Kalinka, A. Kucernak, M. Mistry, S. Nguyen, Mechanical, electrical and microstructural characterisation of multifunctional structural power composites, *Journal of Composite Materials* 49(15) (2015) 1823-1834.

[112] D. Chung, A review of multifunctional polymer-matrix structural composites, *Composites Part B: Engineering* 160 (2019) 644-660.

[113] P. Zhou, Y. Liao, Y. Li, D. Pan, W. Cao, X. Yang, F. Zou, L.-m. Zhou, Z. Zhang, Z. Su, An inkjet-printed, flexible, ultra-broadband nanocomposite film sensor for in-situ acquisition of high-frequency dynamic strains, *Composites Part A: Applied Science and Manufacturing* 125 (2019) 105554.

[114] N. Hu, Y. Karube, C. Yan, Z. Masuda, H. Fukunaga, Tunneling effect in a polymer/carbon nanotube nanocomposite strain sensor, *Acta Materialia* 56(13) (2008) 2929-2936.

[115] J. Dong, J. He, C. Jia, Y. Song, Z. He, H. Wei, T. Zhang, W. Zheng, Z. Jiang, Y. Huang, Growth of carbon black onto continuous carbon fiber to produce composites with improved mechanical and interfacial properties: a step closer to industrial production, *Composites Science and Technology* 173 (2019) 83-89.

[116] J. Dong, C. Jia, M. Wang, X. Fang, H. Wei, H. Xie, T. Zhang, J. He, Z. Jiang, Y. Huang, Improved mechanical properties of carbon fiber-reinforced epoxy composites by growing carbon black on carbon fiber surface, *Composites Science and Technology* 149 (2017) 75-80.

[117] J.G. Simmons, Generalized formula for the electric tunnel effect between similar electrodes separated by a thin insulating film, *Journal of Applied Physics* 34(6) (1963) 1793-1803.

- [118] V.K. Shante, S. Kirkpatrick, An introduction to percolation theory, *Advances in Physics* 20(85) (1971) 325-357.
- [119] Y. Li, J. Yan, L. Qiao, S. Hu, Experimental study on the condensation of ethanol–water mixtures on vertical tube, *Heat and Mass Transfer* 44(5) (2008) 607-616.
- [120] W.I. Lee, A.C. Loos, G.S. Springer, Heat of reaction, degree of cure, and viscosity of Hercules 3501-6 resin, *Journal of Composite Materials* 16(6) (1982) 510-520.
- [121] Y. Liao, F. Duan, H. Zhang, Y. Lu, Z. Zeng, M. Liu, H. Xu, C. Gao, L.-m. Zhou, H. Jin, Ultrafast response of spray-on nanocomposite piezoresistive sensors to broadband ultrasound, *Carbon* 143 (2019) 743-751.
- [122] N. Ghodhbani, P. Maréchal, H. Duflo, Ultrasound monitoring of the cure kinetics of an epoxy resin: Identification, frequency and temperature dependence, *Polymer Testing* 56 (2016) 156-166.
- [123] M.J. Yoo, S.H. Kim, S.D. Park, W.S. Lee, J.-W. Sun, J.-H. Choi, S. Nahm, Investigation of curing kinetics of various cycloaliphatic epoxy resins using dynamic thermal analysis, *European Polymer Journal* 46(5) (2010) 1158-1162.
- [124] M. Hayaty, M.H. Beheshty, M. Esfandeh, Cure kinetics of a glass/epoxy prepreg by dynamic differential scanning calorimetry, *Journal of Applied Polymer Science* 120(1) (2011) 62-69.
- [125] J. Šesták, G. Berggren, Study of the kinetics of the mechanism of solid-state reactions at increasing temperatures, *Thermochimica Acta* 3(1) (1971) 1-12.
- [126] M. Liu, Z. Zeng, H. Xu, Y. Liao, L. Zhou, Z. Zhang, Z. Su, Applications of a nanocomposite-inspired in-situ broadband ultrasonic sensor to acousto-ultrasonics-based passive and active structural health monitoring, *Ultrasonics* 78 (2017) 166-174.